Synthesis, Passivation and Charging of Silicon Nanocrystals

Thesis by

Elizabeth A. Boer

In Partial Fulfillment of the Requirements

for the Degree of

Doctor of Philosophy

California Institute of Technology

Pasadena, California

2001

(Submitted January 26, 2001)

Acknowledgements

I have a confession to make: one of the first things I often read if I pick up a thesis is the acknowledgements. Why so? you may ask. While the main text gives you the scientific story, it is in the acknowledgements that you get the smallest glimpse of the sweat, tears, late nights, early mornings, and things that break, as well as those precious moments when something works, the first experiment is done, the connection is made, and the results are finally understood.

But enough romanticism, I have some serious thanking to do. I was in the very fortunate position of having three advisors—a situation which in hindsight I wish I had taken more advantage of. I'd like to thank Harry Atwater, the professor with whom I interacted most frequently, for his unbridled enthusiasm and his incredible ability to put a positive spin on (what always seemed to me) the most disastrous result. I appreciated very much all my interactions with Kerry Vahala, and enjoyed being able to catch a glimpse of a different advising style. And I wish I had made the trek over to the Spalding building more often for discussions with Rick Flagan.

I was also fortunate to have two great collaborators in Doug Bell and Mark Brongersma. I have really enjoyed working with Doug. He never hesitates to ask the hard questions—a trait that leads to good discussions and ideas. I will also miss Mark's intuitive physical explanations.

There are others who have been key to this thesis. Renato "Plumber" Camata taught me the basics of aerosol nanoparticle synthesis and was a fun co-worker, as was Dr. T. Tambo, who introduced me to XPS and the right way to take care of equipment. Many thanks to Joyce Wong who did a lot of SEM with me—I appreciate both her time and her friendship. Thanks to Deborah Santamore for the manipulation work and the initial charging experiments, and thanks to Michele Ostraat for TEM help. Kyu Sung Min graciously handed over his ion implantation samples and showed me the ropes in the lab.

Thanks to Atwater group members past and present. In particular, to Regina Ragan for ordering fluoroware containers and Ge wafers, Rhett Brewer for the foresight and effort of buying another Linux machine, and Claudine Chen for the countless times she gave me computer help, as well as for all her behind-the-scenes efforts, and all those good meals and cakes. Thanks to Maggie Taylor for buying clean room wipes and Joseph Christopherson for organizing the bolts and for MBE help. Thanks too to the occupants of room 244 (Maribeth Swiatek, Jason Holt) for entertaining my many questions, which ranged from the mundane to the profound. Jason deserves a special mention for lending his dongle without complaint (go ask him what a dongle is). A thank you to John Hartman for always having the time and interest to discuss my scientific results.

Thanks to the Vahala group, in particular Per Olof Hedekvist, for putting up with me while I used their computers and for Matlab help.

I very much enjoyed the time I spent at FOM-AMOLF in Amsterdam. Thanks to Albert Polman for the invitation, to Michiel de Dood for all his help in the lab, and to the others in the opto-electronic materials group.

I'd like to acknowledge Alicia Alonzo, who as well as being a great friend, has heard every important practice talk I have ever given (including candidacy and defense), and who has greatly improved the quality of my scientific presentations.

Thanks to Rosalie Rowe for all her secretarial aid. I would also like to acknowledge the financial aid of the National Science Foundation and Intel, who provided me with generous fellowships.

Finally, thanks to all my friends who have made my time at Caltech most enjoyable (you know who you are), to my parents and to my fiancé (!!!), Olivier Duchemin. Lots to look forward to in life after grad school!

Abstract

Silicon nanocrystals are intriguing from both a fundamental and an applied physics point of view. The efficient room temperature luminescence exhibited by Si nanocrystals (as compared to bulk silicon) and the apparent size-dependent bandgap of Si nanocrystals are two incompletely explained phenomena. Meanwhile, the applied physicist may take advantage of the optical and electronic properties of small Si structures to build devices not possible with only bulk silicon.

In this thesis, nanocrystal samples produced by aerosol techniques were investigated. The aerosol samples were size-classified in the size range of 2–50 nm with a size variation of 15–20%. Conducting tip atomic force microscopy (AFM) was used to manipulate and investigate the samples' charging characteristics. The AFM was used to inject charge into single Si nanocrystals and to observe the dissipation.

The charging characteristics of samples made by ion implantation and annealing were also explored. An atomic force microscope was used to locally inject, detect and quantify the amount and location of charge in SiO_2 films containing Si nanocrystals (size $\sim$2–6 nm). By comparison with control samples, charge trapping was shown to be due to nanocrystals and not ion implantation-induced defects in these samples.

Two models were developed for quantitative charge imaging with an atomic force microscope, one appropriate for non-contact mode and the other for intermittent contact (tapping) mode imaging. From the models, estimates of the best charge sensitivity of an unbiased standard AFM cantilever were found to be on the order of a few electrons. The models were used to estimate the amount of charge injected in the charging experiments: in typical experiments, on the order of 60 electrons were injected in an isolated Si nanoparticle, and a few hundred electrons were injected in SiO_2 films containing Si nanocrystals.

Finally, for optical studies, nanocrystal passivation with hydrogen and SiO_2 were briefly investigated using photoluminescence and X-ray photoelectron spectroscopy.

Contents

List of Figures

List of Tables

Chapter 1 Introduction

1.1 Why study Si nanocrystals?

A silicon nanocrystal, a tiny piece of Si, consists of a few tens to a few tens of thousands of atoms and has typical dimensions of 1–10 nm. My personal interest in this topic springs from the desire to study the basic physics of something that is technologically interesting, and to use the non-intuitive and strange results of quantum mechanics to build devices that take advantage of non-newtonian effects. Silicon nanocrystals are a good candidate for such studies as they are interesting from both a pure physics and applied physics point of view. A nanocrystal's small dimensions make it an ideal system in which to study quantum confinement effects at room temperature, and its optical and electrical properties may be exploited for optoelectronic [1] and electronic [2] devices.

1.2 Optical properties and devices

An explosion of interest in zero-dimensional silicon was set off in 1990 [3] with Canham's discovery of the photoluminescent (PL) properties of porous silicon which he attributed to the "quantum confinement" of carriers. The meaning of "quantum confinement" in this context may be illustrated by considering the effective mass approximation for electrons and holes in a semiconductor and examining the "particle in a box" problem [4], i.e., an electron of effective mass m_e^* and hole of effective mass $-m_h^*$ in a 1-D infinite potential well (Fig. 1.1). The solution of the time-independent Schrödinger equation gives discrete energy levels with energies inversely proportional to the square of the width of the well—in other words, the smaller the width of the well (i.e., the size of the nanoparticle) the higher in energy the ground state. Since in this approximation the effective mass of the hole is negative, this effect gives rise
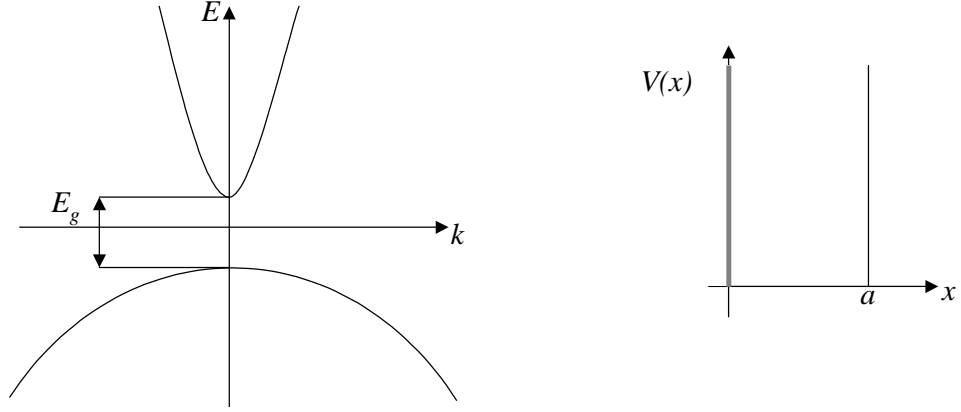
Figure 1.1: Schematic for (right) the conduction and valence bands in the effective mass approximation and (left) infinite square well potential for a particle in a box. The energy of electrons in the conduction band is $E_c = \frac{E_g}{2} + \frac{\hbar^2 k^2}{2m_e^*}$ and the energy of holes in the valence band is $E_v = -\frac{E_g}{2} - \frac{\hbar^2 k^2}{2|m_h^*|}$ (E_g is the bandgap, $\hbar k$ crystal momentum, $m_{e,h}^*$ the effective mass of the electron or hole). Since the ground state for a "particle in a box" is $E_{box} = \frac{\hbar^2 \pi^2}{2m^* a^2}$ (where a is the width of the well), for a confined system, $E_c^{confined} = E_c + \frac{\hbar^2 \pi^2}{2m_e^* a^2}$ and $E_v^{confined} = E_v - \frac{\hbar^2 \pi^2}{2|m_h^*| a^2}$. Thus in the confined system, $E_g^{confined} = E_c^{confined} - E_v^{confined}$, $E_g^{confined} = E_g + \frac{\hbar^2 \pi^2}{2a^2}\left(\frac{1}{m_e^*} + \frac{1}{|m_h^*|}\right)$.

to an increase in the bandgap [5]. Thus luminescence in the visible (400–800 nm or 1.5–3 eV), that is, the emission of visible light after exciting the sample with a bluer (higher energy) source, is often considered a signature of quantum confinement, since the PL signal of bulk silicon is in the infrared (1.1 eV).

Confinement effects are not only credited with increasing the bandgap and thus allowing visible luminescence in Si, but also with increasing luminescence efficiency. Bulk silicon is an indirect bandgap material—that is, a phonon (lattice vibration) is needed to moderate the recombination of an electron and hole in order to conserve crystal momentum. Since phonons are needed, this is an inefficient process (<0.001% at room temperature). When carriers are confined in real space, their wave functions spread out in k-space and the band structure is said to become more direct-like (i.e., no phonon is needed) [6] and thus more efficient (1–10%) [5]. Hence quantum confinement improves upon bulk Si for optical applications in several ways: it brings

the PL into the visible, allows tunability with size, and increases the quantum efficiency. However, the increased efficiency has been most often attributed to the fact that when carriers are confined in a small region, they cannot recombine at defects in another part of the material, and fewer carriers are available for nonradiative Auger recombination [7].

A nano-object, because of its incredibly small size (10^{-9} m), has a large surface-to-volume ratio compared to a macroscopic system. The surface of a nanocrystal therefore plays an important role. Nanocrystals that are unpassivated—i.e., with dangling bonds or other surface defects—will have their luminescence quenched via nonradiative recombinations involving these defect sites. Exactly what role nearby defects play remains an unanswered question in the long debate over the source of the luminescence in nanocrystalline silicon. Current theories suggest that an Si-O vibration may assist band to band indirect transitions [8], or that an Si=O bond in nanocrystals smaller than 3 nm (where the bandgap is large enough to stabilize the surface state) may trap an electron or exciton (bound electron-hole pair) and thus affect the photoluminescence [9].

While there remain many intriguing and outstanding problems regarding the optical properties of nanocrystals, potential applications have already begun to be realized. Silicon is of interest although more optically efficient materials exist (e.g., AlGaAs/GaAs and InGaAsP/InP) because of the easy compatibility with silicon IC processing [10] and the high quality of the Si/SiO_2 interface. Integrated nanoparticle/porous silicon-based light-emitting diodes have been realized [1], prototype optical interconnects on Si substrates studied [11] and photodetectors made (see for example Ref. [12] and references therein). As well, Si nanocrystals have been shown to greatly enhance the efficiency of Er-doped optical amplifiers [13]. The future for Si nanocrystals looks "bright."
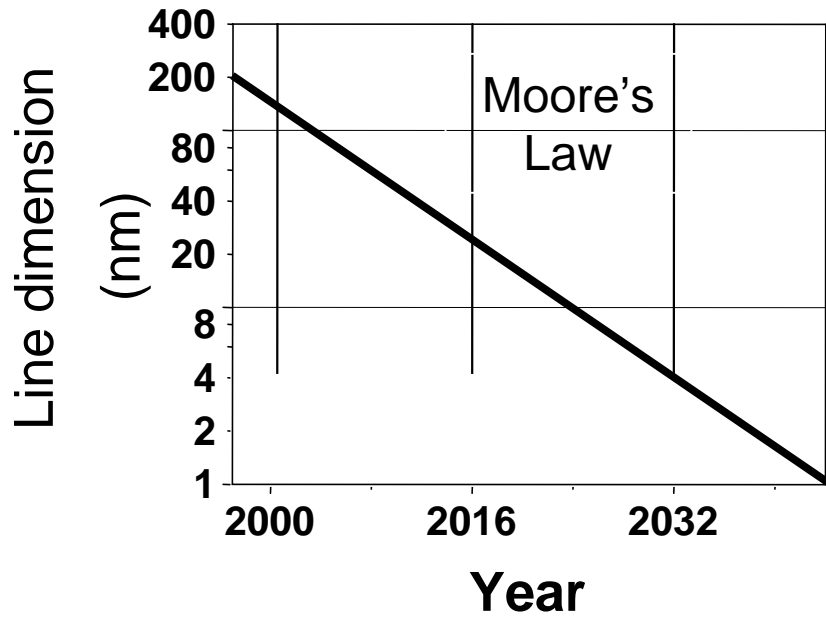
Figure 1.2: Moore's law: device dimensions in integrated circuits tend to halve in size every 18 months.

1.3 Electronic properties and devices

Si nanocrystals show promise for optical devices, although they are not yet competitive in areas currently dominated by other material systems. However, in the electronics industry, silicon is already the material of choice, and device dimensions are steadily decreasing. If Moore's law is to continue to hold and devices continue to shrink in size, the electronics industry will soon reach a regime where quantum effects, such as tunneling and confinement, become important (Fig. 1.2). The difficult question facing this multi-billion dollar industry is how to overcome the challenges of the "quantum limit." One idea is to abolish the transistor and replace it with a nanocrystal based device. A coupled quantum dot "quantum cellular automata" system, proposed by Lent et al. [14], is one such a possibility. A QCA cell consists of four nanoparticles connected by tunnel junctions (Fig. 1.3) and each cell has two electrons. Because of Coulomb repulsion and the ability of electrons to tunnel from one particle to the other, the electrons line up on one diagonal or the other. Since there

"1"　　　　"0"
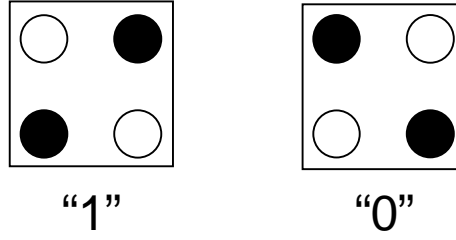
Figure 1.3: Quantum cellular automata cells, consisting of four nanoparticles connected by tunnel junctions, and two electrons. A charged nanoparticle is represented by a filled circle. Because of Coulomb repulsion, the two electrons line up diagonally from each other. Since there are two ground state arrangements, which may be labeled "1" and "0," binary logic is possible.

are two diagonals, there are two states, and thus this system is suitable for binary logic. Interconnects, AND, OR and NOT gates can be fashioned by arranging these cells in patterns, as information is transferred via the Coulomb interaction between adjacent cells (Fig. 1.4). Snider and coworkers [15,16] have demonstrated a prototype QCA cell in the Al/AlO_x material system (made by electron-beam lithography and shadow evaporation), which operates at dilution refrigerator temperatures (<1 K). The advantages of a nanoscale *Si nanocrystal* based QCA include room temperature operation and the usual advantages of using silicon. Room temperature operation is possible when the charging energy, $E_{charging} = \frac{e^2}{2C}$, the energy needed to add an electron, is greater than $kT{\sim}25$ meV, the thermal energy at 300 K. Since capacitance is proportional to size, a nanocrystal fulfills this requirement. The usual advantages of silicon include the large knowledge base and infrastructure, and the high quality of the Si/SiO_2 interface.

While throwing out the transistor and replacing it with a QCA cell is a somewhat revolutionary idea (and would require dots < 1 nm in diameter, might be very slow, and suffer from such problems as background charge [17]), a more practical potential technological use of Si nanoparticles is in a floating gate nonvolatile memory [2,18]. Such a device looks schematically like a transistor (Fig. 1.5), with the key difference that there is layer of silicon nanocrystals embedded in the gate oxide. In order to
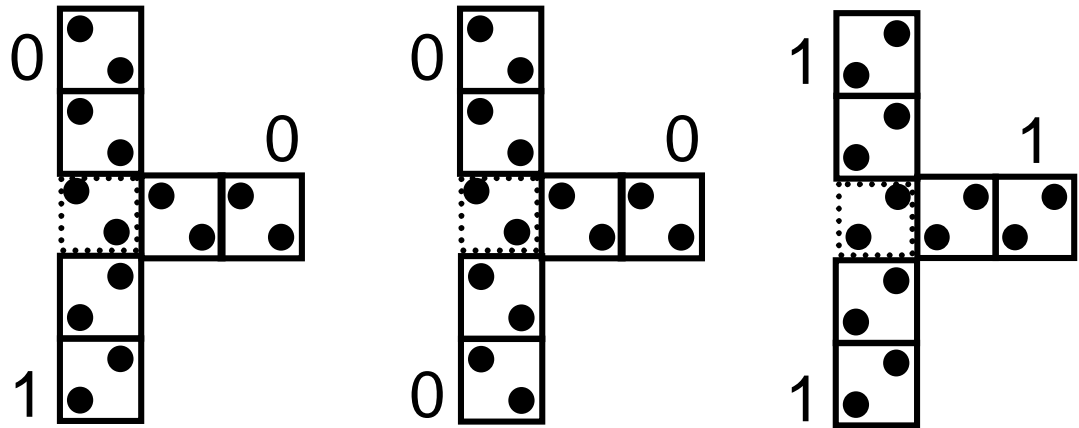
Figure 1.4: QCA AND gate. Only the charged nanoparticles are shown. Input signals are applied to the upper and lower branches of structure and the middle branch represents the output. One cell (represented with a dotted border) requires a slight bias for correct AND gate operation. Coulomb repulsion between cells causes them to align which, together with the biased center cell, produces the right output for an AND gate.
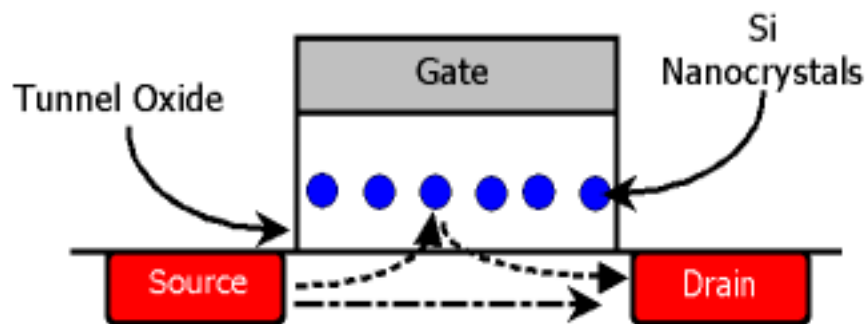
Figure 1.5: Schematic for a nanocrystal nonvolatile floating gate memory.
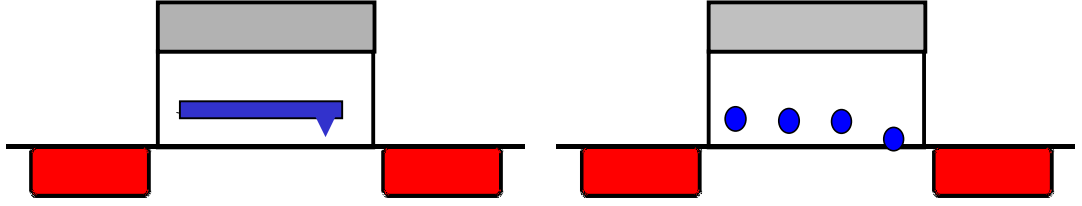
Figure 1.6: Fabrication error in a bulk polycrystalline floating gate (left) and the analogous error in a nanocrystal floating gate (right). Note that in the bulk gate case, all trapped charge will leak out because of this defect, while in the nanocrystal case, only one particle will lose its charge.

store a bit of information, the source or drain is biased to provide carriers to the channel, and a potential is applied to the gate, allowing carriers to tunnel through the thin tunnel oxide and be trapped in the nanocrystals. This layer of stored charge in the gate oxide shifts the voltage threshold of the device, and this shift can then be detected as a stored bit of information.

The advantage of a nanocrystal gate, instead of a bulk polycrystalline gate, arises from the discreteness of the gate rather than any quantum property. The gate discreteness results in greater error tolerance. A small error in a bulk gate allows all the stored charge to leak out, and the device does not work (Fig. 1.6). A similar error in a discrete gate, however, permits the charge to leak out of one nanocrystal, but all the others remain charged, and the device still functions. As well, such a device is scalable to single particle dimensions [19, 20]. More sophisticated devices that take advantage of the discreteness of nanoparticle energy levels and Coulomb blockade effects are also possible. Coulomb blockade refers to the extra energy needed to add an electron to an already charged object (i.e., $E_{charging} = \frac{e^2}{2C}$).

1.4   Outline of the thesis

Several types of nanocrystal samples and experiments are discussed in the chapters ahead. One type of sample consists of isolated aerosol-synthesized silicon nanocrystals (no top oxide) on Si and oxidized substrates (Chapter 2). A second type is

made by ion implantation and annealing (Chapter 3) and a third type involves aerosol nanoparticles deposited in the nonvolatile memory geometry (with a top oxide, Chapter 5). Conducting tip AFM (atomic force microscopy) was used to study the charging characteristics of these samples and these experiments are described in Chapters 2 and 3. Calculations have been done to investigate AFM images of charge (Chapter 4). Optical properties have been studied via photoluminescence measurements (both at Caltech and FOM in Amsterdam) to investigate quantum confinement and qualitatively determine defect densities, and XPS (X-ray photoelectron spectroscopy) was used to probe the surface characteristics—these results are reported in Chapter 5. In addition to my own work, I report on manipulation experiments done by Deborah Santamore, and isolated single nanocrystal charging performed by Doug Bell (Chapter 2). These studies all contribute to a better understanding of the properties of silicon nanocrystals and their possible technical applications.

Chapter 2   Single nanocrystal charging

2.1   Introduction

The expanding capabilities for nanoscale fabrication have spurred interest in single electron transistors and memory devices. While the size regime of most interest for exploitation of single-electron effects is below the resolution threshold for electron-beam lithography, techniques involving self-assembly or nucleation show promise for the creation of ultra-small device structures. However, practical devices have been limited by issues of size uniformity and spatial ordering of nanoscale features.

Floating gate nonvolatile memories are one of the most accessible applications for room temperature single-electron devices. An intermediate step towards the realization of single-electron nonvolatile memories is the replacement of the relatively large, conventional floating gate with a two-dimensional array of small, isolated nanoscale floating gates embedded in the gate oxide. Such devices have been demonstrated [2,18] using Si nanocrystals in a conventional floating gate memory configuration. Often nanocrystals are formed within an SiO_2 layer by implantation and annealing [21,22]. This technique produces an array of nanocrystals with statistical size and position distributions. The devices also exhibit a distribution of charge transit times during charging of an ensemble of nanocrystals. The physical reasons for this behavior are not completely understood, but could be related to a dispersion in thickness of the oxide barrier between the nanocrystals and substrate, interface states in the nanocrystals, or shifts in electronic levels or charging energies due to nanocrystal size variations.

Although nanocrystals in nonvolatile memory elements are buried within an oxide layer, it is also important to characterize the properties of isolated single nanocrystals. The nanocrystals studied in this chapter were fabricated using a novel, recently developed method for producing size-classified Si nanocrystals [23]. This method enables size classification with a standard deviation of less than 15–20% and nanocrys-
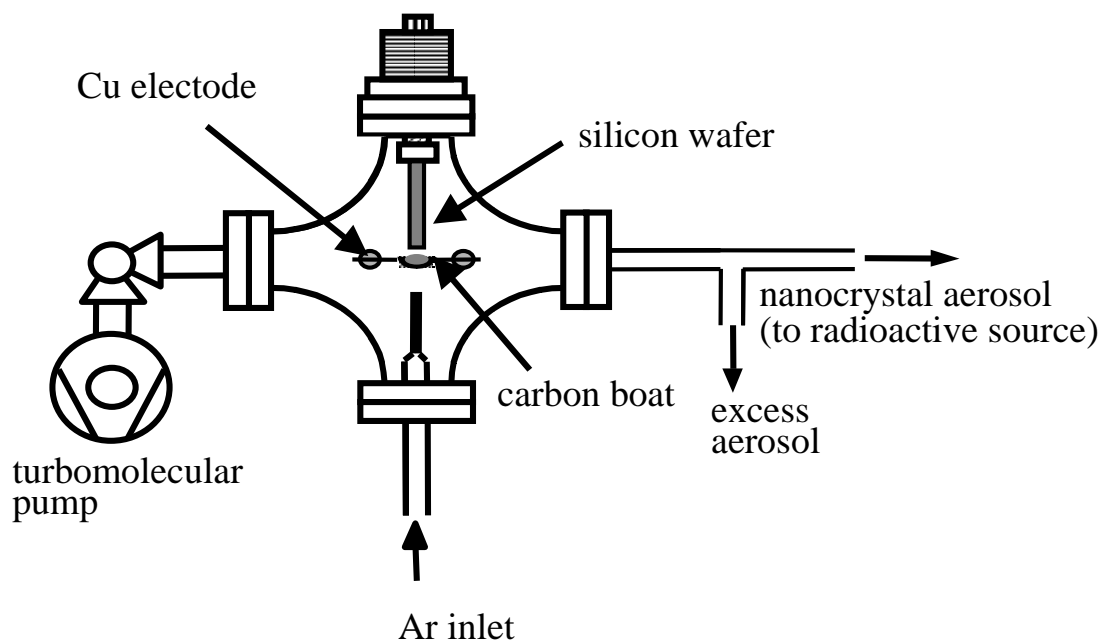
Figure 2.1: Schematic of chamber for nanocrystal synthesis by thermal evaporation [26].

tal sizes as small as 2 nm. In order to understand the electronic properties on a single-nanocrystal level, atomic force microscopy [24] (AFM) was performed with a conducting tip [25] to probe individual Si nanocrystals.

2.2 Aerosol synthesis of Si nanocrystals

The samples were made by decomposition of silane in a nitrogen carrier gas [27] or by thermal evaporation in Ar. Briefly, the thermal evaporation samples were made in a small chamber (Fig. 2.1), baked to provide a base pressure on the order of 10^{-9} torr, and back-filled with ultra-pure Ar to atmospheric pressure—if these precautions were not taken, SiO_x nanoparticles instead of Si nanocrystals formed, as determined by XPS (see Section 5.3). A piece of silicon was place in a carbon boat attached to Cu electrodes and resistively heated. Upon heating the silicon melted and evaporated, followed by the nucleation of small nanocrystals out of the supersaturated vapor. The aerosol—the Ar gas containing the Si nanoparticles—was then drawn
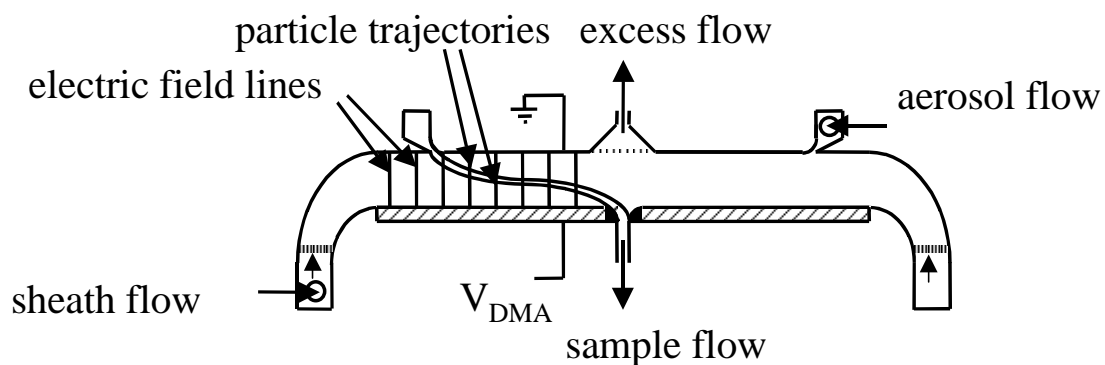
Figure 2.2: Radial differential mobility analyzer [26].
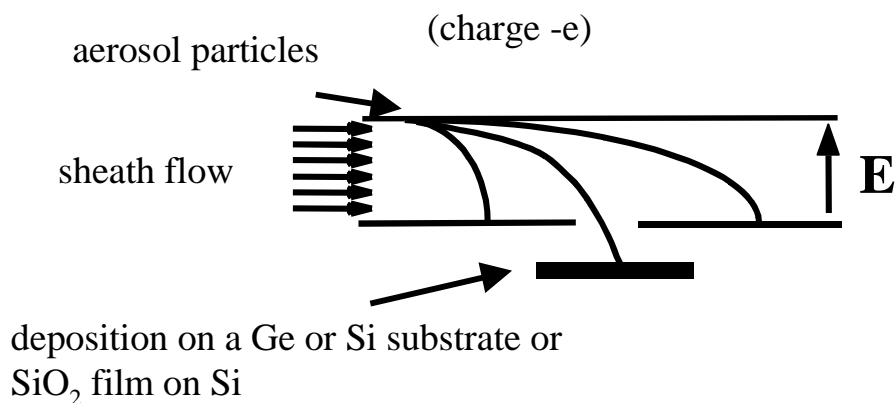
Figure 2.3: Basic principles of differential mobility analysis. A charged particle entering the region between the two plates will have a different trajectory depending on its size. With the voltage (field) chosen for a particular particle size, particles smaller than the target will be relatively undisturbed by drag and will quickly run into the second plate (leftmost trace). Particles larger than the target size will be much more affected by drag and will be carried further horizontally by the sheath flow before finally arriving at the bottom plate (rightmost trace) [26].

out of the synthesis region to be sorted by size using a radial differential mobility analyzer (RDMA) [28]. The aerosol was first exposed to a radioactive source (^{85}Kr, β radiation) so as to impart a unit charge to the nanocrystals, before entering the RDMA (Fig. 2.2). The RDMA works analogously to a mass spectrometer: roughly speaking, an RDMA consists of a set of parallel plates with voltage V and a horizontal sheath flow (typically 15 l/min, see Fig. 2.3) between them. A charged particle entering the RDMA will have two major forces on it: an electrostatic force, which is size-*in*dependent, and an aerodynamic drag force, which is size-*de*pendent. Thus by tuning the voltage between the plates, different sizes will be directed to the collection region and deposited on a substrate (for more details, please see Ref. [26], and references therein). Nanocrystal samples were collected on Ge substrates, oxidized and unoxidized Si substrates and holey carbon grids by electrostatic precipitation. The oxide thickness of the oxidized substrates was 100 nm.

Figure 2.4 [23] shows four examples of the size distributions obtained using the RDMA. This data was determined by measuring particle diameters on transmission electron micrographs (TEM) such as Fig. 2.5 of samples deposited on holey carbon grids. The crystallinity of the samples was determined from TEM dark field images. The voltages in Fig. 2.4 are those that were applied to the RDMA to collect that particular sample, and the other numbers represent the mean diameter, and the standard deviation (in parentheses). This data demonstrates we have size control within 15–20%.

2.3   Atomic force microscopy

Our main tool in these nanoparticle studies was the atomic force microscope. An AFM has three main modes of mapping topography: contact [24], non-contact [29] and intermittent contact or tapping [30]. The most important part of an AFM is the tip with its nanoscale radius of curvature (Fig. 2.6). The tip is attached to a micronscale cantilever which reacts to the van der Waals interaction and other forces between the tip and sample. In contact mode, the cantilever deflects due to the force
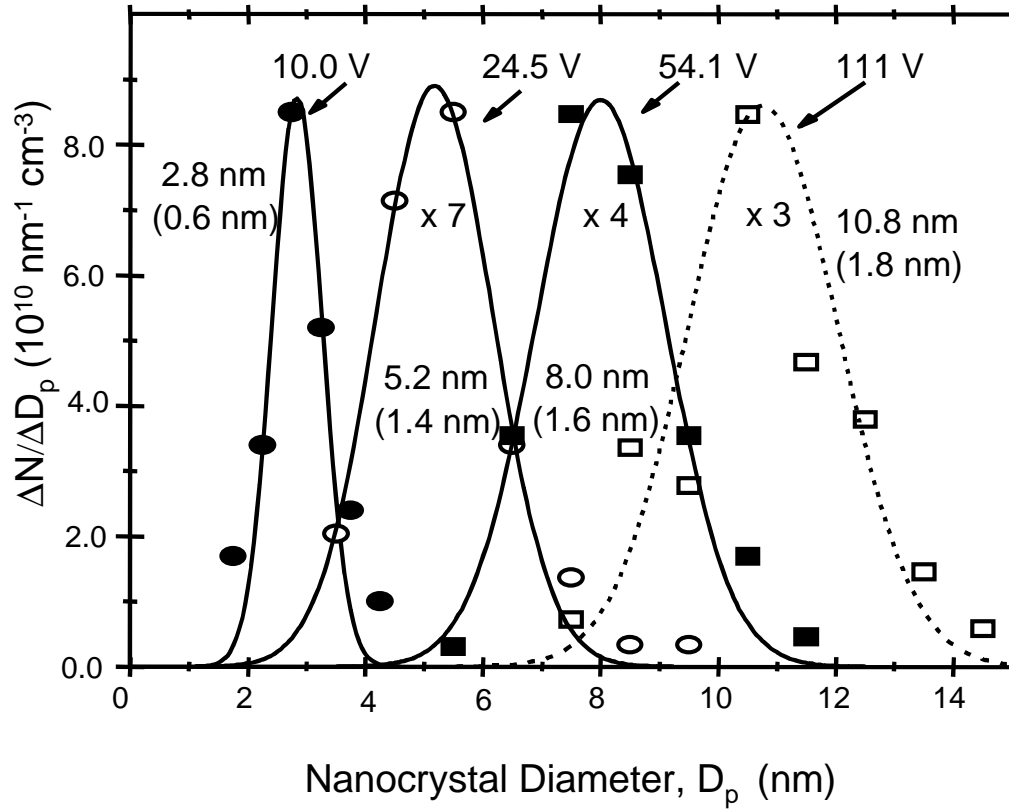
Figure 2.4: Nanocrystal size distributions for four samples after size classification, determined by fitting Gaussians to data measured from TEM images. Voltages applied to the RDMA, mean particle sizes for each distribution, and standard deviations to the fits (in parentheses) are shown [23].
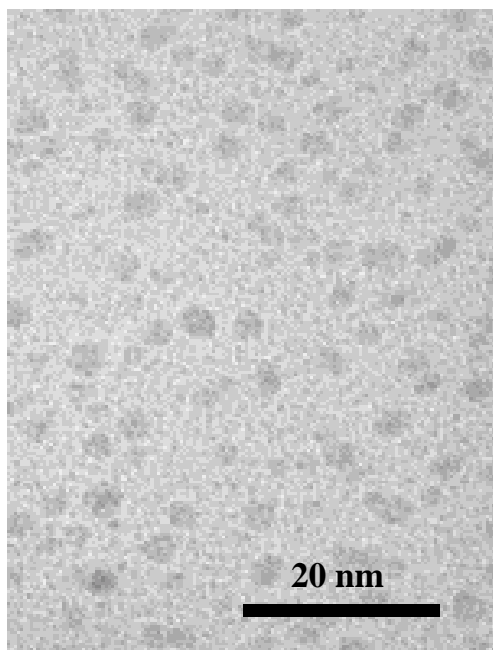
Figure 2.5: Transmission electron micrograph of size-classified silicon nanocrystals.
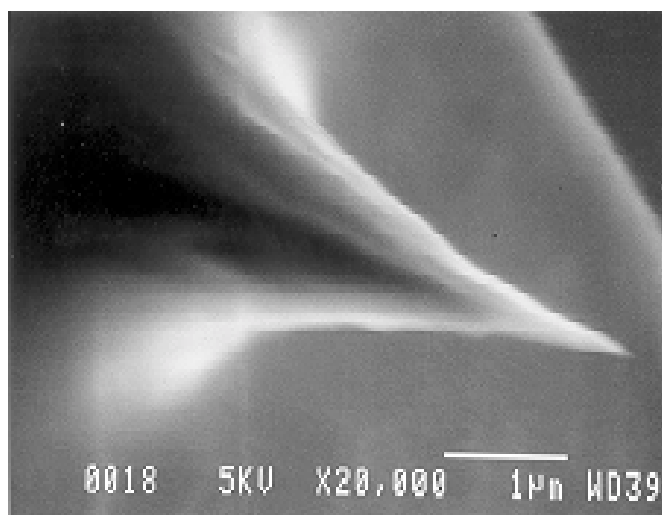
Figure 2.6: Secondary electron micrograph of an AFM tip.

detector   laser
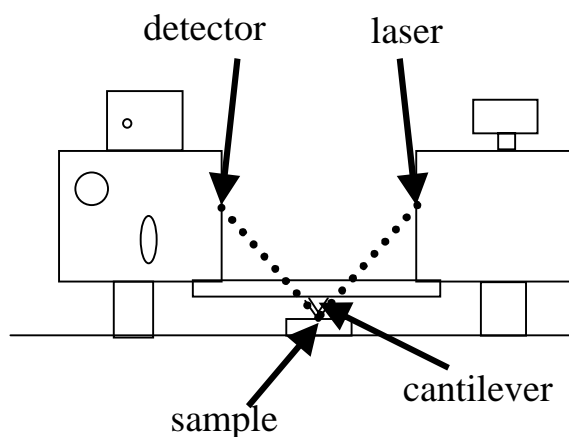
sample   cantilever

Figure 2.7: Schematic of an atomic force microcope (based on a Park Scientific Autoprobe CP). Dotted line represents the laser beam that is reflected off the back of the cantilever to the detector.

and this deflection is measured by reflecting a laser beam off the back of the cantilever (Fig. 2.7). The microscope produces an image by recording the feedback signal from the control loop that maintains a constant amount of cantilever deflection—i.e., tip-sample force or tip-sample spacing. In non-contact and tapping modes the cantilever is excited close to its resonant frequency, and the feedback loop maintains a constant tip oscillation amplitude—or roughly speaking, a constant force gradient or average tip-sample spacing. Please see Chapter 4 for more on non-contact and tapping mode imaging. In contact mode, tip-sample spacing is < 0.5 nm and the forces involved are on the order of 10^{-7}–10^{-6} N. In non-contact mode, tip-sample spacing is larger, typically ~ 10 nm, and the forces are from 10^{-12}–10^{-11} N. In tapping mode sampling by the tip is pointwise, with instantaneous forces comparable to contact mode but with smaller average forces.

2.4 Nanoparticle manipulation with an AFM

The forces bonding nanoparticles to substrates are believed to be van der Waals forces, of order 10^{-11}-10^{-9} N. This number is between the force values of contact
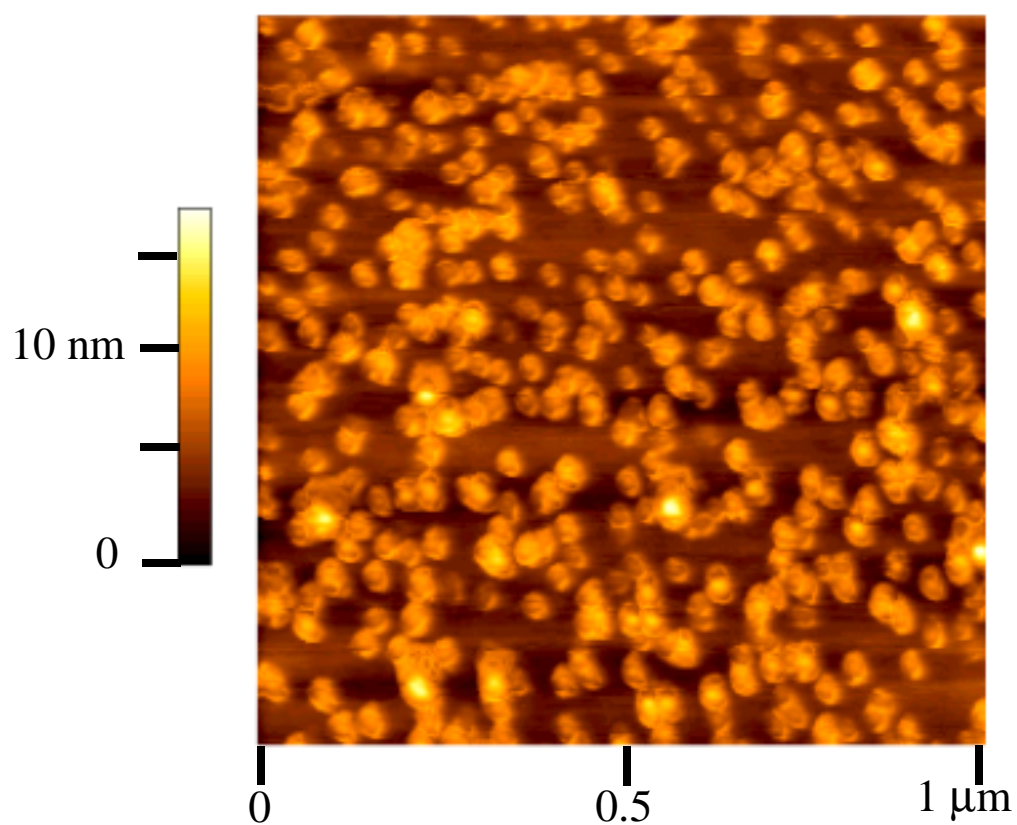
Figure 2.8: Non-contact mode image of a size-classified sample of silicon nanocrystals made by thermal evaporation.
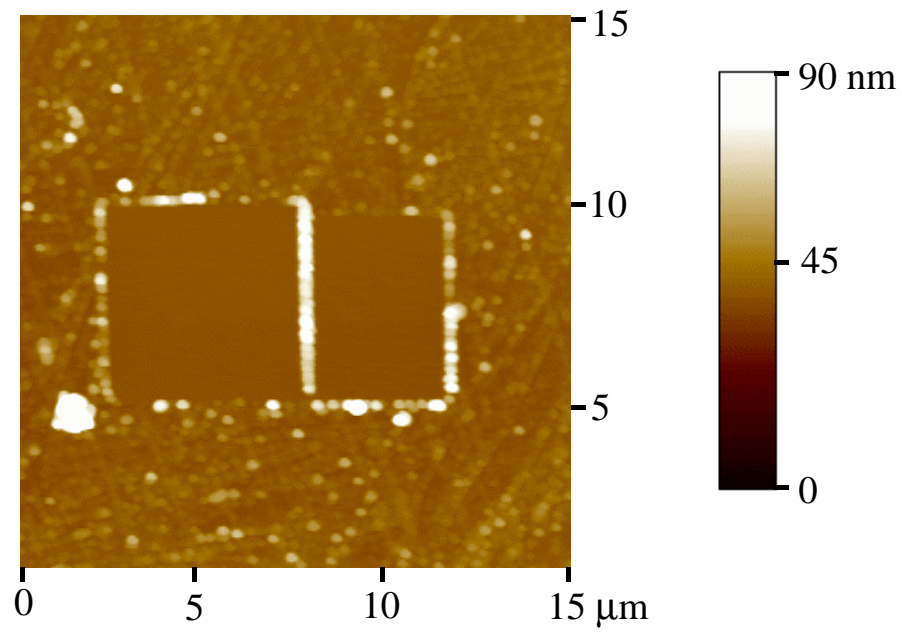
Figure 2.9: Tapping mode image after simultaneous multi-particle manipulation in contact mode.
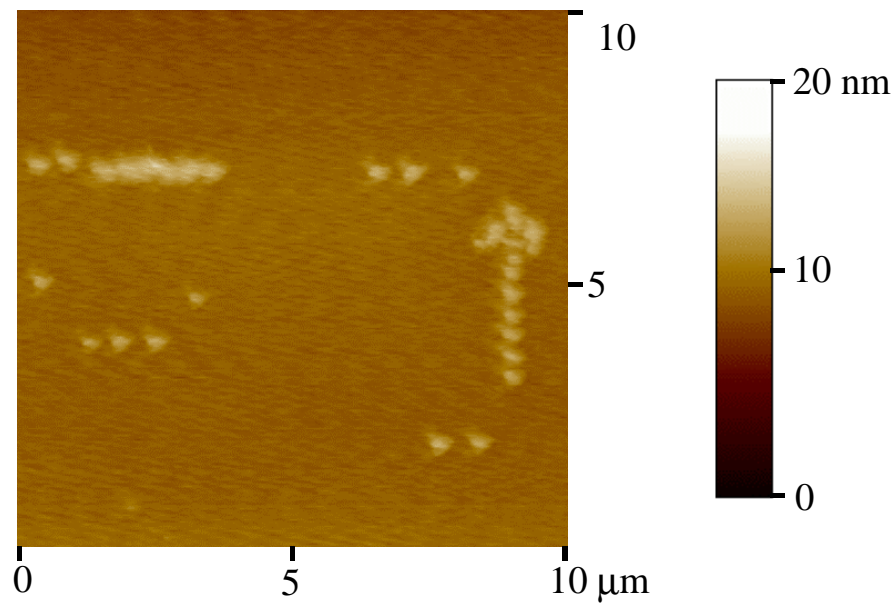
Figure 2.10: Tapping mode image after single particle manipulation in contact mode.

mode and those of non-contact/tapping modes—thus it is not surprising that it is possible to image particles in non-contact/tapping mode, and to manipulate particles in contact mode. Figure 2.8 shows a non-contact mode image of a size-classified aerosol sample made by thermal evaporation. Figures 2.9 and 2.10 are tapping mode images taken after contact mode particle manipulation. In Fig. 2.9, the particles have been "snow-plowed" out of the way to form thick lines and in Fig. 2.10 particles have been moved one by one to form an arrow shape. It appears that all the particles have the same, slightly triangular form upon careful inspection of Fig. 2.10. This is a common imaging artifact, from tip-sample convolution, that, in our case, is probably due to nanoparticles sticking to the AFM tip after contact mode manipulation. It was found that coating the Si AFM tips with Cr and Au reduced the tip-particle adhesion and the resulting image problem. AFM manipulation of nanoparticles was first demonstrated by Junno et al. [31] and an excellent computer-controlled system has been developed at USC [32]. The interest of having such a particle manipulation capability is the possibility of building novel nanometer structures for experimental investigation.

2.5 AFM single nanocrystal charging experiments

Since Si nanocrystals are of great interest as charge storage nodes in nonvolatile memory devices, the goal of this work was not only to demonstrate non-destructive imaging and manipulation but also to perform charge injection into a nanocrystal and monitor its discharge using tapping mode AFM. Single-electron transport through Si nanocrystals has recently been observed [33]. In other work [34], charging was performed on buried arrays of Co nanoclusters. The goal of the experiments described here was to accomplish charging of isolated Si nanocrystals on an insulating substrate. In this way individual nanocrystal electronic properties may be probed, and electron injection parameters can be more precisely controlled. Effects of oxide thickness and surface properties can also be studied on the single nanocrystal level. In addition, charging of bulk oxide defects, which could contribute for nanocrystals buried within

oxide layers, can be ruled out.

Tapping mode AFM was performed on the nanocrystal samples after transfer to the microscope enclosure; a surface oxide layer was thus expected to be present on the nanocrystals. The degree of oxidation was evaluated using X-ray photoelectron spectroscopy (XPS) performed on 15 nm Si nanocrystals deposited on a Ge substrate. Si 2p core level analysis showed a substantial unshifted Si peak after 2 hours of ambient exposure, indicating an oxide shell thickness of < 3 nm (see Chapter 5 for more on XPS). Oxidation of the AFM samples was minimized by storing the samples in flowing nitrogen; the AFM enclosure was also purged with nitrogen during data acquisition.

To perform nanocrystal charging, the AFM tip was halted directly over a nanocrystal, a voltage was applied, and the average tip-sample distance was decreased from tapping-mode distance to the point where measurable charge could be transferred (i.e., tip oscillation amplitude ~ 0). Average distance was controlled by monitoring the attenuation of the AFM cantilever oscillation amplitude. The tip was held at the desired position for a short time (usually 30 s) after which it was retracted for tapping mode imaging. Applied tip voltage during charging was -20 V.

Charging experiments were performed in flowing gaseous nitrogen. In addition to slowing the oxidation of the nanocrystal, the nitrogen environment served to minimize water exposure (estimate of relative humidity, $< 10\%$). The presence of water vapor in room air was found to greatly decrease the discharge time of nanocrystal samples made by ion implantation of SiO_2 films, suggesting that an adsorbed water layer provided a conduction path for the discharge process (see Fig. 3.6 on page 32). This decrease in discharge time was found to be reversible upon re-introduction of those samples into nitrogen.

The presence of excess charge in the nanocrystal produces an electrostatic contribution to the total force between the AFM tip and sample. The AFM feedback causes the tip to retract to maintain the requested oscillation amplitude, and the charging manifests as an increase in apparent height in an AFM image.

Figure 2.11 shows several sequential AFM images of a charged Si nanocrystal, taken from a larger series of image data. The apparent lateral diameter of the
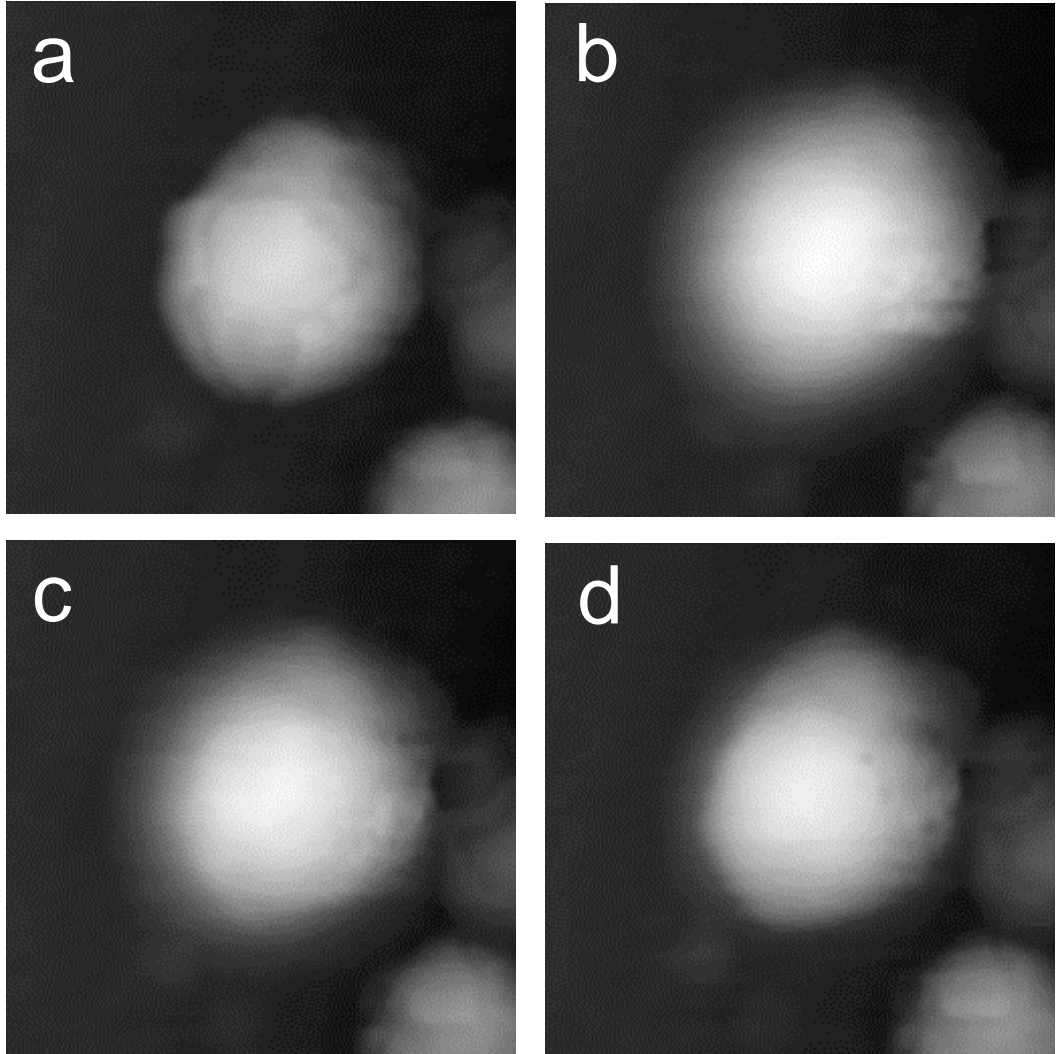
Figure 2.11: AFM images of the charging and discharging of a single Si nanocrystal. Nanocrystal size (height) as measured by AFM is about 28 nm. Imaged area in each panel is 200 x 200 nm. (a) Nanocrystal before charging. Images (b), (c), (d) were acquired at 45 s, 217 s, and 527 s after charging.

nanocrystal in the AFM images reflects the tip radius of curvature, nominally 25–50 nm, but height AFM measurements indicate a nanocrystal diameter of about 28 nm. These sequential images show the initial increase and subsequent decrease in the stored charge with time, indicated by a change in apparent height. This apparent change in height indicates that the AFM is sensitive to the injected charge. Resolution is observed to degrade when the nanocrystal is charged due to the long-range nature of the electrostatic force compared with the shorter-range forces that contribute in tapping mode imaging. The apparent heights for this nanocrystal data set are plotted in Fig. 2.12. It can be seen that a change in apparent height of about 5 nm occurs initially, and that after 1000 s the nanocrystal has only partially discharged.

Although additional observations of the charging/discharging process were made, there were cases for which no charging effect was seen. This was possibly due to excessive oxidation of the nanocrystal, prior contamination of the tip, accelerated discharging of the nanocrystal due to the presence of contamination or defects, or insensitivity to the small quantity of charge injected. Occasionally the tip appeared to damage the particle. One of the disadvantages of this technique is that it is hard to control the tip-sample distance precisely during charging and thus exact reproducibility is difficult. However, charging and discharging have been observed in nanocrystals as small as 4 nm, with an apparent height change due to charging of only about 1 nm.

2.6   Model results

A model of the response of the AFM tip to fixed charge was developed which will be discussed in more detail in Chapter 4. Briefly, the electrostatic force on the tip due to the charged nanocrystal was calculated by first assuming a uniform surface charge over the upper half of the nanocrystal then using the method of images to find the induced image charge in the tip. The Coulomb interaction between these two charge distributions was then calculated to determine the total electrostatic force between tip and sample. The tip's motion as a function of time was solved from the equation
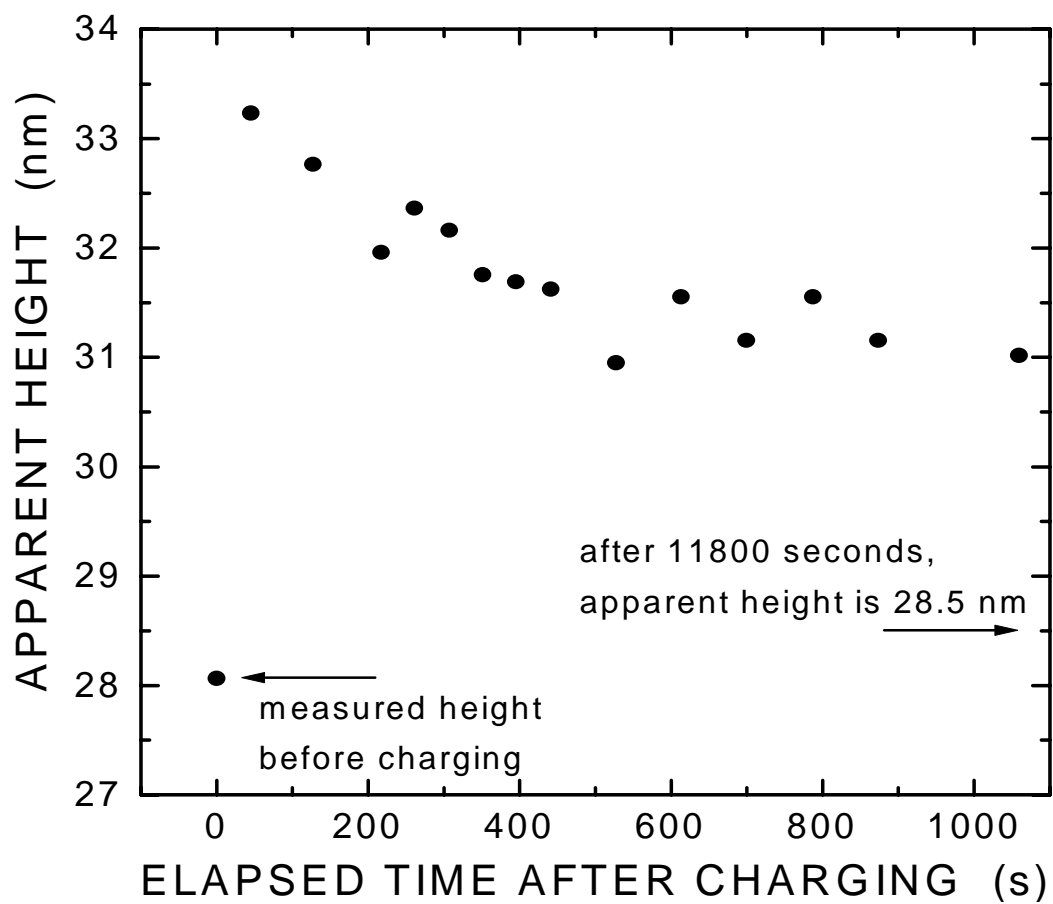
Figure 2.12: Apparent nanocrystal height before charging by AFM and during discharging. Heights were measured from a series of AFM images of a single nanocrystal. The images shown in Fig. 2.11 were taken from the same series.

for a simple harmonic oscillator:

$$m^*\ddot{z} + \gamma\dot{z} + k(z - z_{L0}) = F_o\cos(\omega t) + [F_{t-s}(z,t)]_z \qquad (2.1)$$

where tip mass (m=10^{-11} kg), damping constant (γ =10^{-11} kg), spring constant (k=2.16 N/m), driving force (F_o=0.48 nN) and driving frequency (ω =2πf, f=73.13 kHz) were estimated from experiments or tip manufacturer's specifications. The term representing the force interaction between the tip and sample, $[F_{t-s}(z,t)]_z$, had three components: one due to the van der Waals' force when the tip is not in contact with the sample [35] and another representing the contact forces [36], and the third representing the electrostatic term. The tip oscillation amplitude decreases approximately linearly with tip-sample spacing when the tip taps the surface. Model image contours can be generated by adjusting the average tip-sample spacing in the model (i.e., z_{L0}) to maintain a constant set-point amplitude (in this case 10.3 nm). The resulting calculated "image" is the set of average tip heights (z_{L0}) maintained by the tip as it scans over the charged particle, with a constant set-point oscillation amplitude. Figure 2.13 shows the measured and calculated contours across the nanocrystal of Fig. 2.11 for several charge states. These calculations yield a maximum stored charge of order 60 electrons.

2.7   Summary

We have demonstrated the ability to make size-classified ensembles of Si nanocrystals on insulating substrates using aerosol techniques. Size control is important for consistent performance if nanocrystals are to be incorporated into devices. Our methods of nanoparticle synthesis and size control are compatible with current silicon technology, another important factor when considering changes to an industry that prefers evolution to revolution. We have also used an AFM to manipulate particles, a technique useful for building nanostructures for novel experiments (see Chapter 6). Conducting tip AFM has been used to inject charge into single Si nanocrystals and to monitor
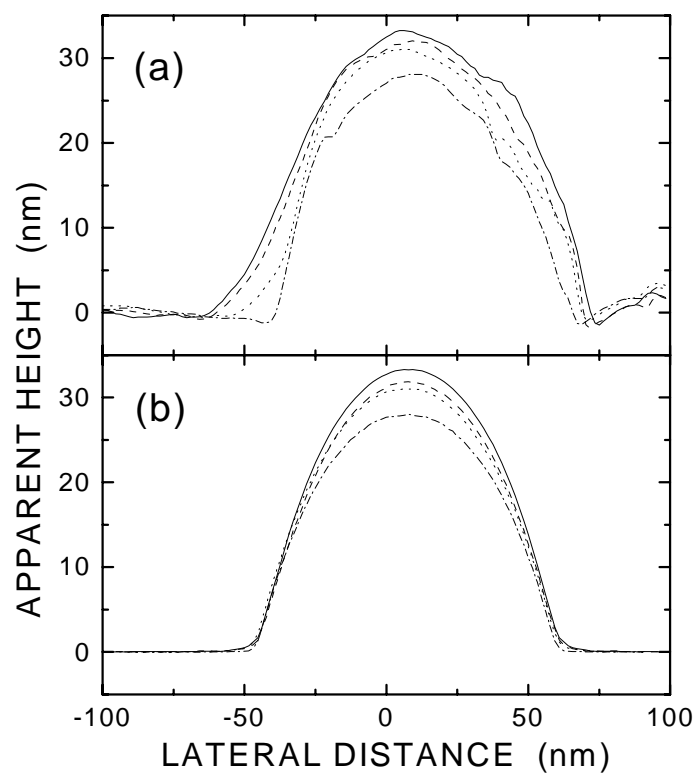
Figure 2.13: (a) Measured and (b) calculated apparent nanocrystal heights for several different values of excess charge. Calculated profiles are shown for (from bottom) 0e, 44e, 49e, and 56e charges on the nanocrystal.

the subsequent discharge. This technique could be exploited further to investigate discharging rates as a function of environmental and processing factors. For example, discharging rates as a function of oxide thickness might be looked into, or the effect of drying the sample and placing it in vacuum might be explored. As well, this technique might be used with other types of samples to investigate the charge trapping centers, as is done in the next chapter.

Chapter 3   Electronic properties of Si nanocrystal samples made by ion implantation and annealing

3.1   Introduction

Future developments in nanoscale silicon electronics require tools for local manipulation and probing of stored charge. Charge storage and manipulation at the nanoscale are particularly important to nonvolatile floating gate memory devices such as the newly-developed nanocrystal-based memories [2, 18] in which the floating gate consists of a dense array of Si nanocrystals embedded in the gate oxide (see Section 1.3, Fig. 1.5 on page 6). Such devices potentially offer both superior nonvolatile memory performance relative to conventional flash memories, and a simple design that is scalable to nanometer dimensions [19, 20]. Silicon, with its mature technology, is the material of choice for these devices as structures can be fabricated cheaply and reliably. In general, however, nanoparticle synthesis methods introduce defects in the oxide host which can affect charge injection and retention [37].

Traditional device analysis techniques such as capacitance-voltage measurements [37] give important macroscopic device information, but in order to probe the *local* properties of a device, a technique capable of detecting the presence and motion of a few localized charges is necessary. Current-voltage measurements are impractical because of the very low currents involved. Conducting tip atomic force microscopy (AFM) is sensitive to a variety of forces, including electrostatic, thus making it a good tool for mapping weak electrostatic potentials [25, 38] and capacitance [39] on the nanometer scale. It can also be used to inject electrons or holes into a localized region in materials such as polymers [40], thin insulating films [41], double barrier

$CeO_2/Si/CeO_2/Si$ structures [42], and Co nanoclusters embedded in SiO_2 [34]. For these reasons an AFM is a useful tool to study the injection and dissipation of charge in SiO_2 films containing ion beam-synthesized Si nanocrystals [43]. In this chapter we show from experiments on charge injection in silicon nanocrystal floating gates that charge trapping is due to the presence of nanocrystals and not defects from the implantation process. Using a generalized force model of the tip-sample interaction (see Chapter 4), we combine electrostatic modeling and AFM imaging to investigate the discharging dynamics of injected charge.

3.2   Si nanocrystal synthesis by ion implantation and annealing

The samples used in this study were made by ion implantation and annealing. A 100 nm wet thermally grown silicon dioxide layer on lightly B-doped Si substrates was implanted at room temperature with 35 keV Si^+ ions to a fluence of $4x10^{16}$ Si/cm^2 (Fig. 3.1). The samples were then annealed at 1100ºC for 10 minutes in vacuum (base pressure $< 8x10^{-7}$ torr) to allow the nucleation and growth of silicon nanocrystals (size $\sim$2–6 nm, as determined from transmission electron microscopy). Please see Ref. [44] for details of nanocrystal formation.

3.3   Charging of ion implanted samples– where is the charge stored?

In order to probe the charging characteristics of silicon dioxide films containing silicon nanocrystals, and to investigate the location of the charge trapping sites in these samples, AFM charging experiments were performed, similar to Section 2.5. Briefly, charge was transferred from the AFM tip to the samples by applying a potential to the tip (–10 V in this case), disengaging the feedback of the microscope, then lowering the tip toward the sample surface. The distance between the tip and sample
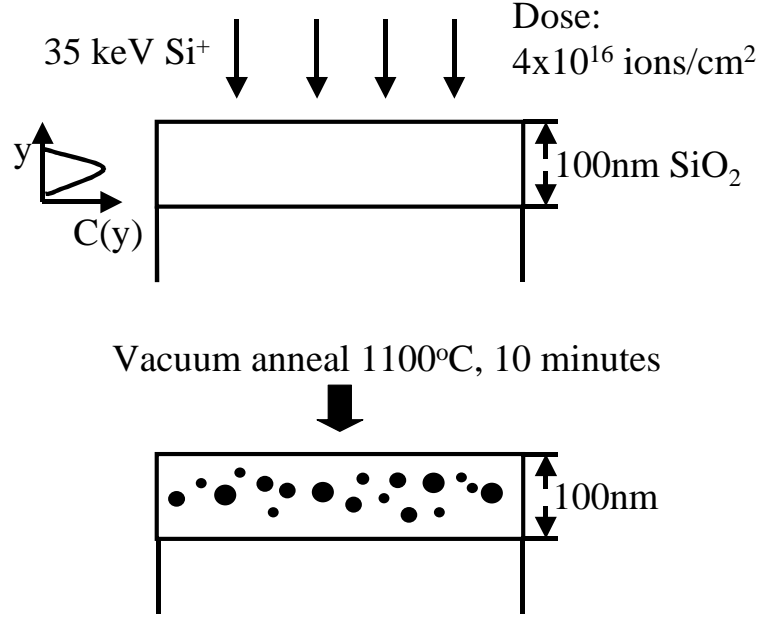
Figure 3.1: Synthesis of SiO_2 films containing Si nanocrystals by ion implantation and annealing. C(y) represents the ion concentration profile.

was monitored by observing the damping of the tip oscillations on an oscilloscope [45]. After contact and charge transfer, the feedback was re-engaged, the AFM tip grounded, and images made. The atomic force microscope (AFM) and highly doped ($> 10^{19}$ cm^{-3}, Debye length < 5 Å) Si tips were from commercial sources [46]. Images were taken in non-contact mode, with the sample stage grounded, in a box purged with N_2 gas (resulting humidity $< 10\%$).

Figure 3.2 (a) shows a non-contact mode AFM image of an Si implanted and annealed sample before charging, and Fig. 3.2 (b), (c) and (d) show the initial charging and subsequent discharging of the sample. Instead of observing the apparent increase in height of a particle as in the single nanocrystal charging case, the AFM image of charge now appears as a protrusion on the surface due to the electrostatic interaction between the image charge in the grounded tip and the charge in the sample.

In the single nanocrystal case it was fairly clear that the charge was stored in or on the nanoparticle since that is what changed size in the image. In this case, however, the answer to the question "where is the charge stored?" is not as obvious.
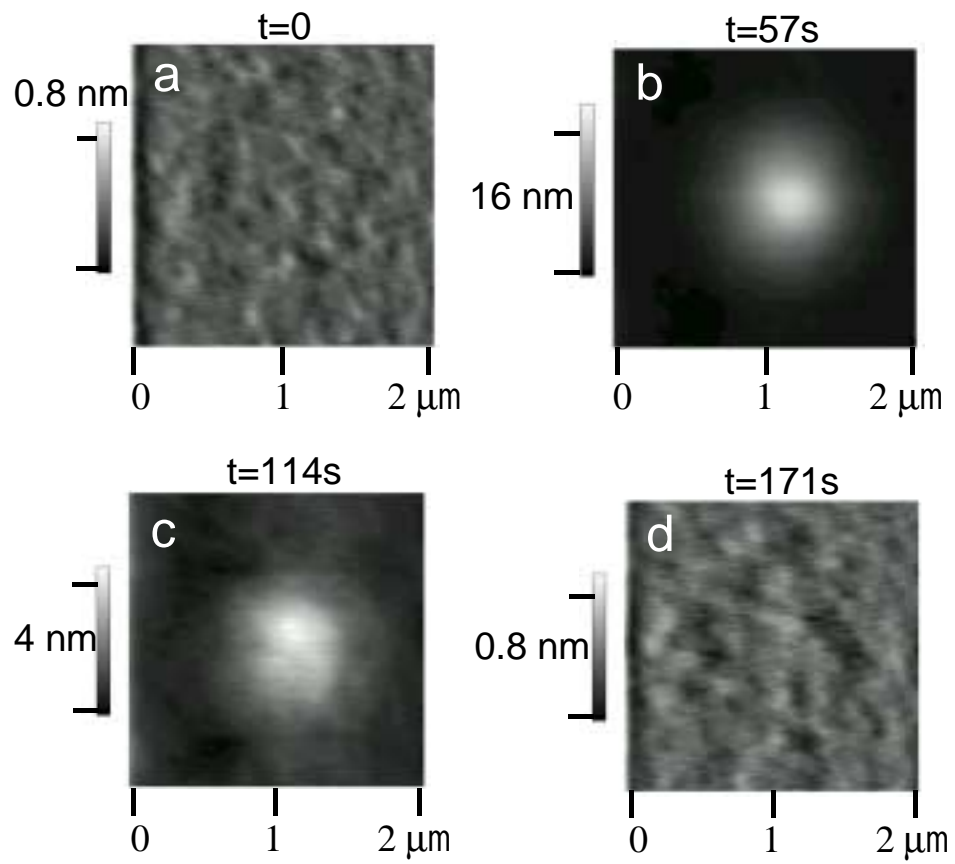
Figure 3.2: Charging of ion implanted samples—unetched.
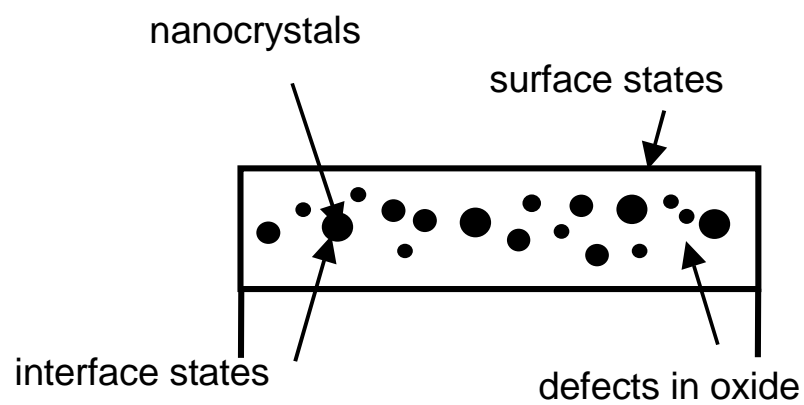
Figure 3.3: Possible locations of trapped charge.
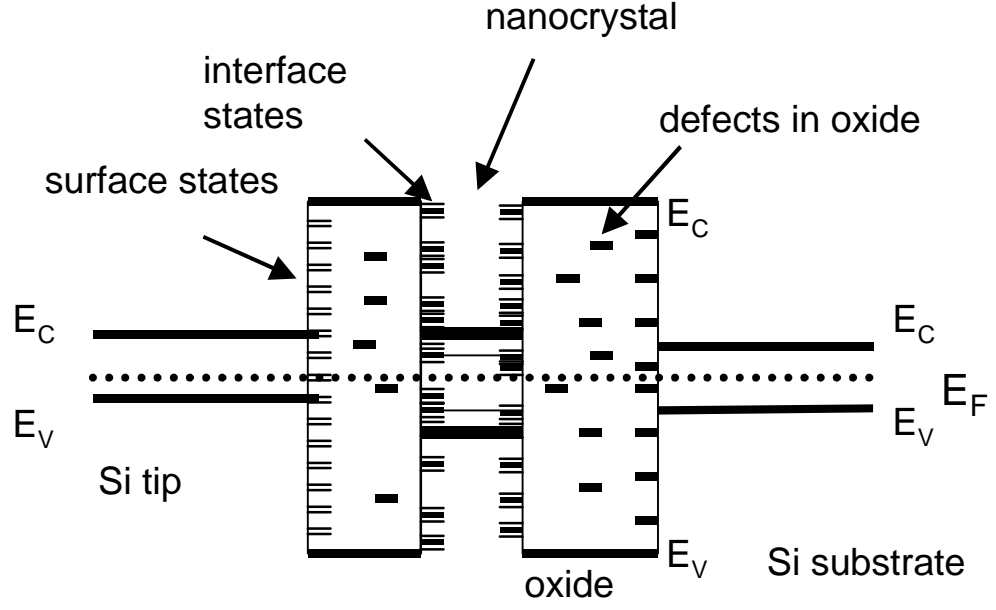
Figure 3.4: Schematic showing possible charge traps on an energy diagram. E_C, E_V and E_F represent the energy of the conduction band, valence band, and Fermi level respectively.

Possible charge traps include: nanocrystals; surface states that arise from the vacuum anneal (e.g., from contamination or the evolution of oxygen [47]); dangling bonds or other interface states between the nanocrystal and the oxide; and defects from the ion implantation process (Ref. [48] and references therein). Mobile ions are another possibility that might give rise to this effect. Figure 3.3 shows the possible locations of the trapped charge in real space and Fig. 3.4 is a schematic showing the possible charge traps in energy space.

In order to determine the location of the charge traps, we investigated two types of control samples. Control samples consisted of a) unimplanted (i.e., no nanocrystals, no defects from implantation) and b) Ar implanted SiO_2 films, implanted at room temperature with 50 keV Ar^+ ions to a fluence of 2.9×10^{16} Ar/cm^2. The inert element argon and the particular ion energy and fluence were chosen so as to produce samples without nanocrystals, but with the same ion implantation damage profile as the Si implanted samples (as calculated using TRIM [49]). The control samples were
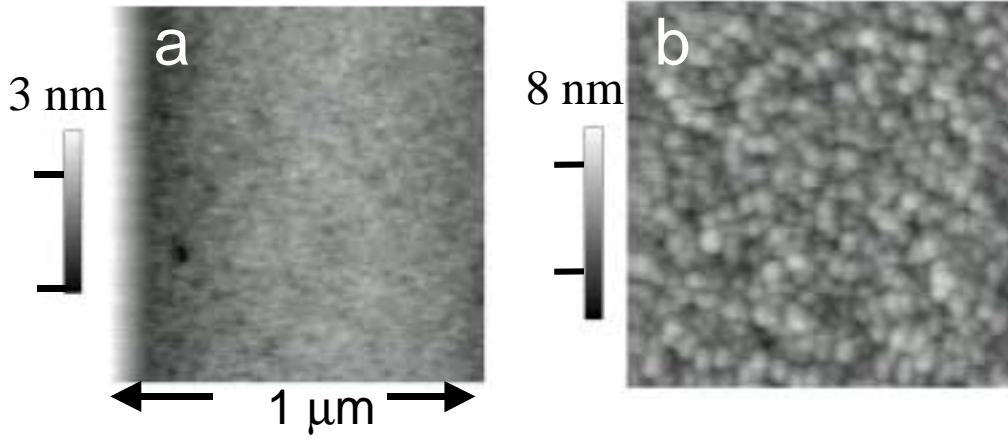
Figure 3.5: Etched (a) unimplanted and (b) Si nanocrystal samples. Note the difference in morphology.

annealed as in Section 3.2.

3.4   Etched samples

After annealing, it was found that *all* samples charged, both the nanocrystal *and* control samples. This result suggests that surface states from contamination or the evolution of oxygen during the vacuum anneal are the localized states that charge, or that the anneal allows mobile ions to diffuse into the sample.   To eliminate surface states and investigate if other charge trap sites exist, the samples were etched with buffered hydrofluoric acid [50] approximately halfway through the film, as measured by Rutherford backscattering spectroscopy (RBS). In Fig. 3.5 are AFM images of (a) an etched unimplanted control sample and (b) an etched silicon nanocrystal sample. Note the differences in morphology in the two cases: the unimplanted sample (a) is very smooth, with a root-mean-square roughness on the order of a few angstroms, while the roughness in the silicon nanocrystal sample is an order of magnitude larger. We believe the features in Fig. 3.5 (b) are individual nanocrystals. Their lateral extent is artificially enlarged due to tip-sample convolution. From this image, nanocrystal density is $\sim 6 \times 10^{10}$ cm^{-2}, similar to that measured from transmission electron mi-
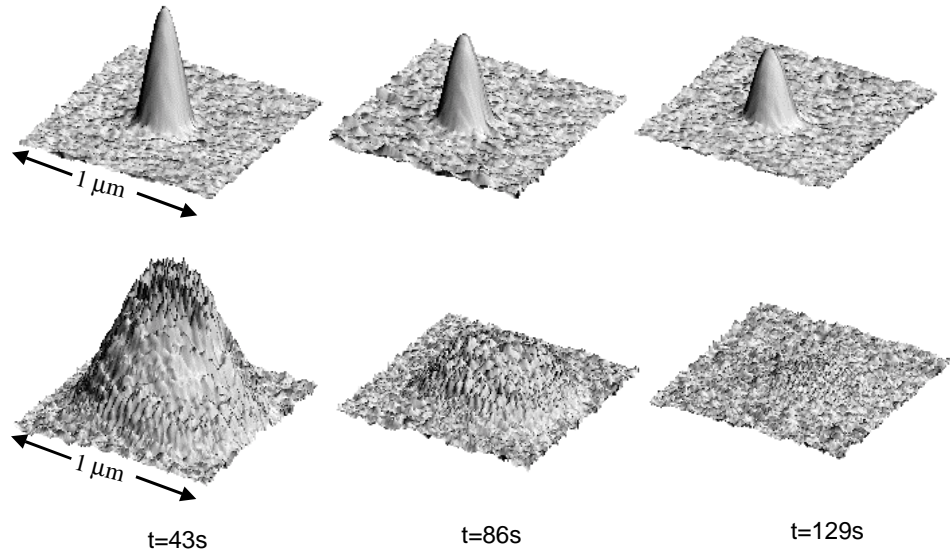
Figure 3.6: Charging and discharging of an unetched sample in a relatively dry environment (top row) and in a relatively wet environment (bottom row). In the first instance, the experiment was done in N_2 and in the second in air.

crographs (TEM). However, due to the relatively large radius of curvature of the tip (~ 50 nm), and the high density of particles, it is possible that not all nanocrystals are imaged with the AFM and that the actual particle density is somewhat higher.

Charging experiments were repeated on the etched samples, but no charging was seen. This supports the idea that surface states are responsible for charging and eliminates the possibility of mobile ions. However, since etching is a wet process, it is possible that a water layer on the surface affected the charging and discharging dynamics. Figure 3.6 of an *unet*ched sample, shows the differences involved in the charging and discharging of a sample in a relatively *dry* environment (in N_2, top row) versus in a relatively *wet* environment (air, bottom row). It is possible that in the "wet" etched sample case, charge was injected but dissipated too rapidly to be detected with the AFM. However, after a gentle 20 minute 200^oC anneal in vacuum to rid the surface of any water layer, no dramatic charging was seen.

The charging experiment was repeated once more on samples that had remained overnight in the microscope enclosure (Fig. 3.7) or in air. This time, it was found

t=0

t=57s after charging

12
nm

0.5 μm

16
nm

1
nm

1
nm

1 μm
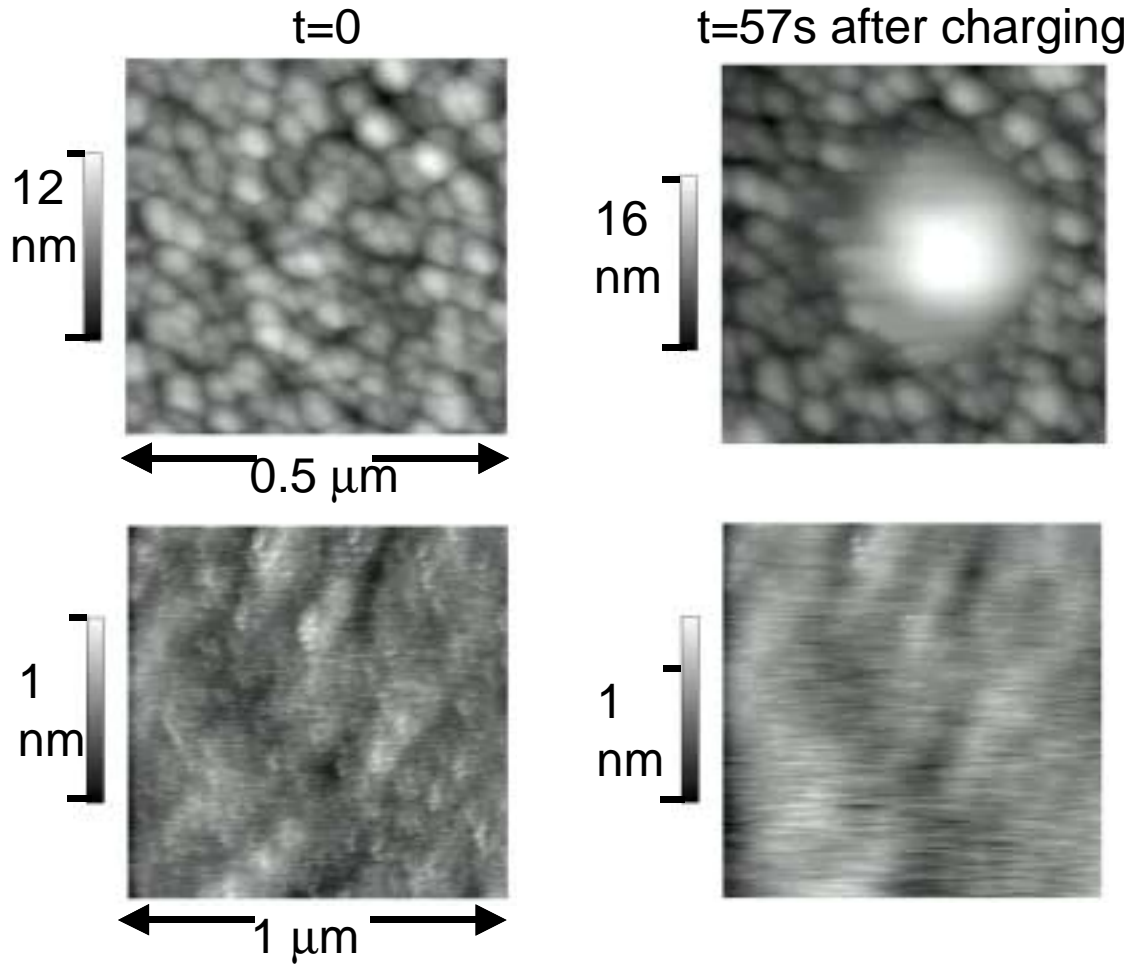
Figure 3.7: Charging results which demonstrate that charge is trapped in or on nanocrystals, and not in bulk oxide defects. In the top row we see localized charging in an etched Si nanocrystal sample, an effect not seen when the experiment is repeated with an Ar implanted SiO_2 film on Si (bottom row).

Immediately after etching   After air exposure
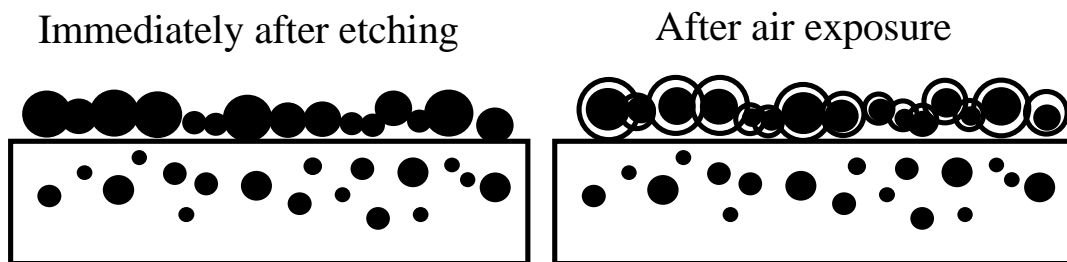
Figure 3.8: Explanation for the initial lack of charging of etched Si nanocrystal samples. After etching, the redeposited nanocrystals form a quasi-continuous layer (left sketch). After enough oxygen exposure, the conductivity decreases due to the growth of a native oxide (right sketch).

that the silicon nanocrystal sample *did* show localized charging, while the control samples, in particular the Ar implanted sample, did not. This result indicates that besides surface states, which can be removed by etching, it is the nanocrystals or nanocrystal interface states, and not bulk oxide defects from ion implantation, which store charge.

Our explanation for why the nanocrystal samples did not charge initially is as follows (see Fig. 3.8): humidity was ruled out as the factor responsible for a lack of charging since the post-etch anneal did not result in more than a suggestive charge signal, and samples that charged after an overnight purge (such as in Fig. 3.7 (b)) continued to do so after the sample and microscope were exposed to air. However, hydrofluoric acid etches SiO_2 much more rapidly than Si (about three orders of magnitude faster). Thus while the oxide is etched away, the Si particles remain in the solution. We propose that instead of being washed away, many of the particles from the etched-away SiO_2 are redeposited on the sample, forming a quasi-continuous layer. When charge is injected in such a layer, it can dissipate rapidly and not be detected. After enough exposure to oxygen, however, a native oxide forms on the nanocrystals, and the dissipation of the injected charge is less rapid and can be detected.

X-ray photoelectron spectroscopy (XPS) data (Chapter 5) in Fig. 3.9 of the Si 2p peak shows qualitatively the amount of oxidation that occurs immediately after etching and after 16 hours in a purged N_2 atmosphere. The small difference in the peak at
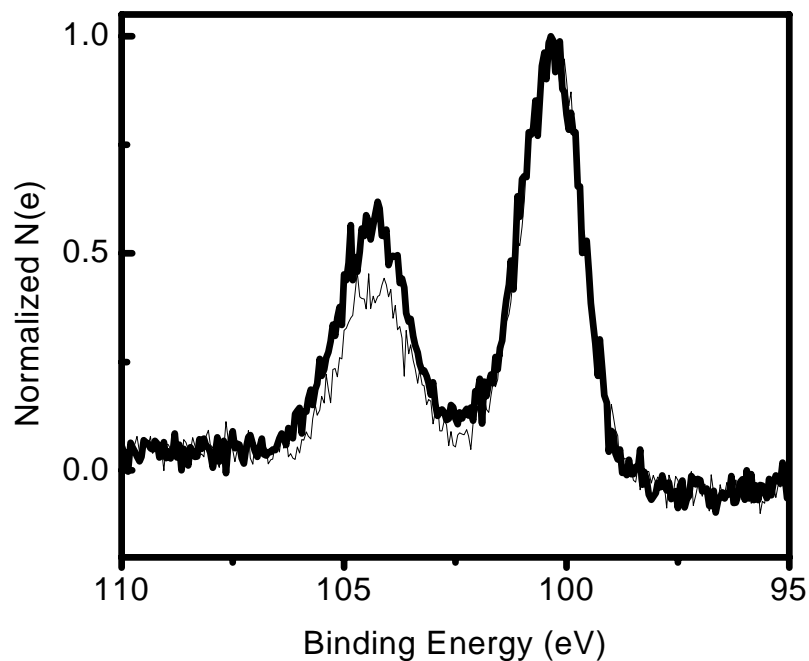
Figure 3.9: Si 2p XPS signal of an etched SiO_2 film containing Si nanocrystals immediately after etching (thin line) and after 16 hours in a purged N_2 atmosphere (thick line).
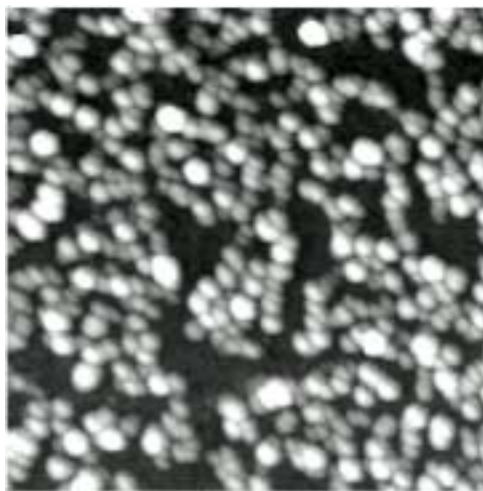
Figure 3.10: AFM image of an SiO_2 film containing Si nanocrystals, after a 5 minute etch in buffered HF. Note the many particles and few bare spots seen, despite the fact the oxide has been fully etched.
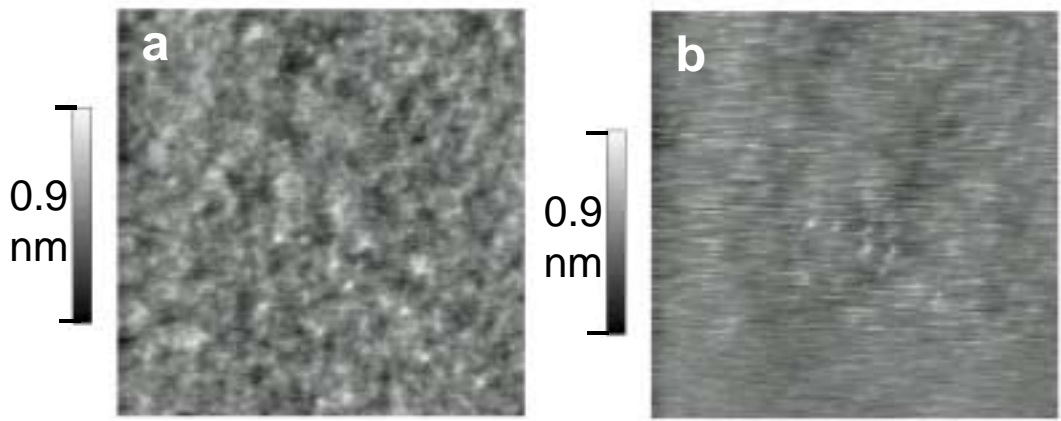
Figure 3.11: Charging attempt on an etched, unimplanted, annealed control sample. (a) Before charging attempt and (b) after. Note the "washed out" quality to the image in (b). Lateral dimension is 1 μm.

104 eV indicates that only a small increase in the oxide thickness (< 1 nm) is necessary to observe trapped charge. Evidence that supports our hypothesis that particles are redeposited on the surface during etching include AFM images of fully-etched samples which still show the presence of nanoparticles (Fig. 3.10) and photoluminescence (PL) studies which show a PL signal characteristic of nanocrystals [51] despite the fact that the SiO_2 film has been completely etched away. Faint charging on a fully-etched nanoparticle sample was seen, while a fully-etched unimplanted control sample (i.e., just a bare Si substrate) and a silicon-on-insulator sample did not charge.

While *localized* charging was not seen in general in the etched control samples, occasionally there was a "washed out" quality to the images after a charging attempt (Fig. 3.11). This was interpreted as a fast discharge transient, possibly related to a water layer. Note that Fig. 3.11 (b) was scanned from bottom to top, and the smoothest area is at the beginning of the scan. This is consistent with the hypothesis that charge has been deposited and is dissipating rapidly.

It should be noted that these results are statistical in nature, i.e., the experiments were repeated several times and the general results stated above. Because of poor control over the tip-sample separation distance (monitored simply by looking at the
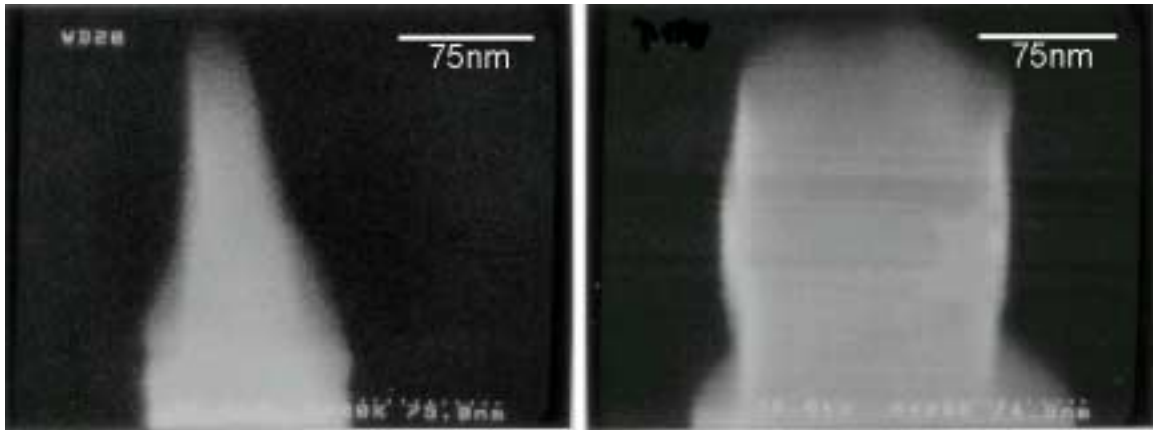
Figure 3.12: Secondary electron micrograph of an AFM tip before (right) and after (left) damage during charge injection.

tip oscillation amplitude on an oscilloscope), it was difficult to consistently charge a sample by the same amount. Occasionally, instead of observing the appearance of a charge "protrusion" that would decrease with time, a new, permanent feature would appear in the image. This was interpreted as voltage-induced oxidation or most often as deposition of material from the tip. As well, the shape and size of the tip were found to be important parameters relative to charging, which might be altered unintentionally during the experiment. Indeed the most charge injection tended to occur when the image had poor lateral resolution or a tip artifact—or in other words, when the tip was either blunted, or contaminated. A blunted tip would make a better contact, thus lowering resistance and increasing charge transfer, or a dangling particle at the end of the tip picked up while scanning would be an asperity with a small radius of curvature, thus producing a high field region conducive to charge injection. Figure 3.12 is of an AFM tip before (left) and after (right) damage by charge injection. In Chapter 6 we will discuss experiments that avoid the problem of tip damage during charging (page 88).
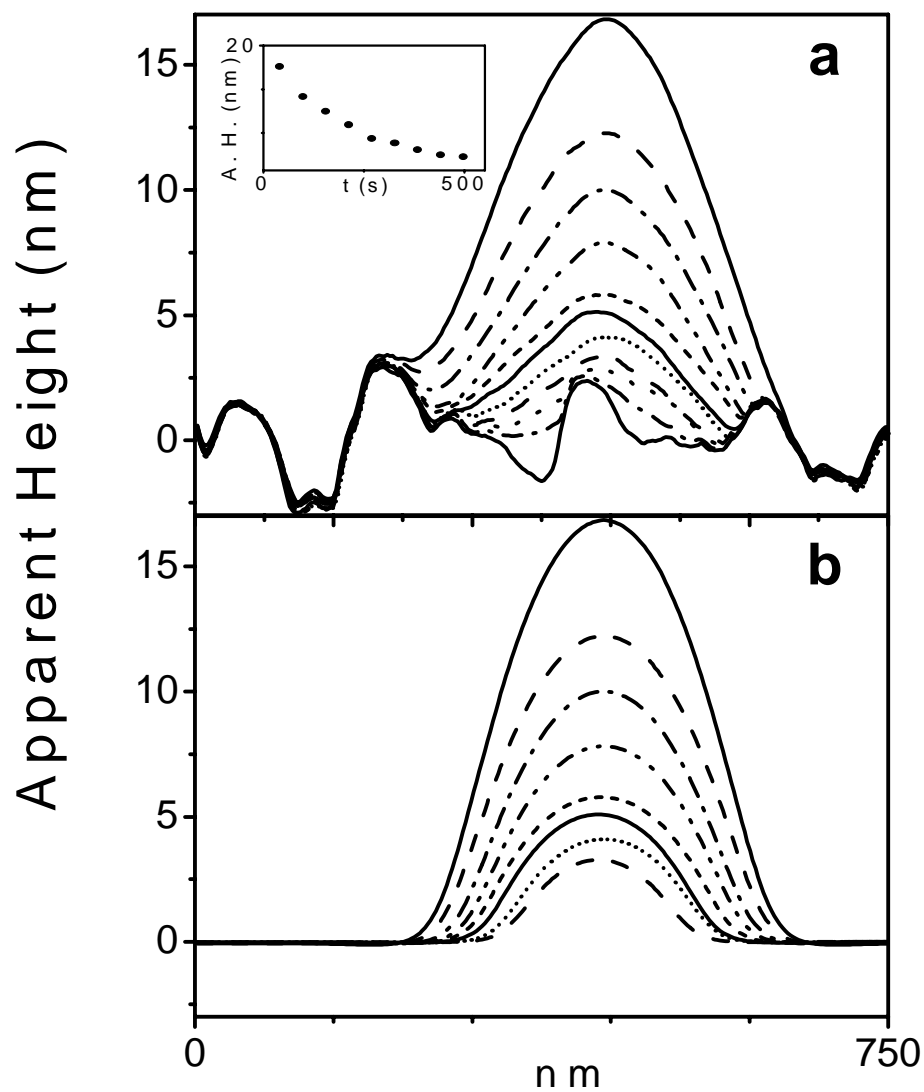
Figure 3.13: (a) Experimental discharge time series and (b) corresponding fits to the data. Inset: decrease of the apparent height (A. H.) with time. The first trace was taken approximately 40 s after charging, and each subsequent trace at 57 s intervals.
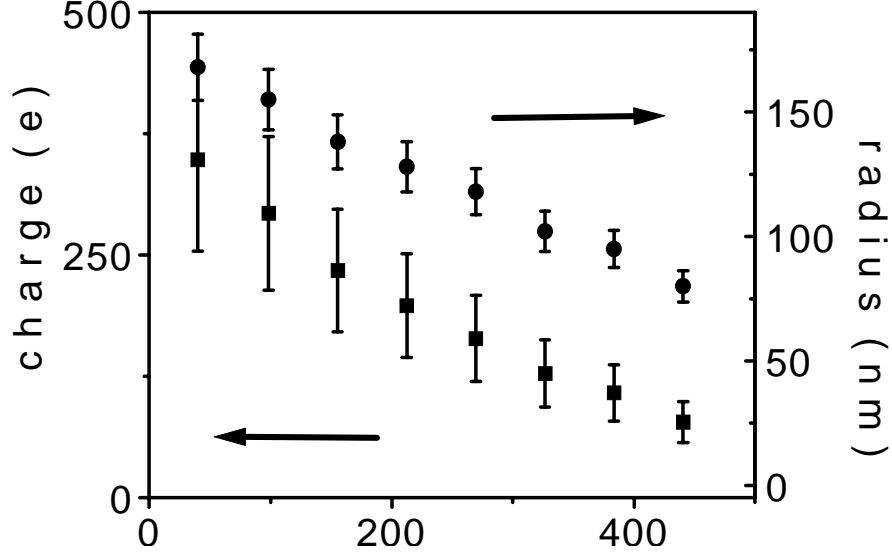
Figure 3.14: Quantity and location of the injected charge as a function of time, as determined from the fits (in Fig. 3.12 (b)) to the AFM discharging time series data (Fig. 3.12 (a)). Note the result that the area over which the charge is located decreases as the charge dissipates. Error bars estimated from errors in tip size, offset and set-point force gradient.

3.5   Modeling and charge dissipation

Besides using the AFM to determine charge trapping sites, we have also looked at AFM images of charge to investigate discharging dynamics. Figure 3.13 (a) shows a discharging time series—vertical cross-sections of subsequent AFM images are plotted on the same axes. In the inset to the figure the "apparent height" of the injected charge decreases from $\sim$ 17 nm to 3 nm in 500 s. Figure 3.13 (b) consists of the corresponding fits to the data, obtained by an iterative method similar to Section 2.6 and explained in more detail in Chapter 4. In Fig. 3.14 the amount and spatial extent of the charge as a function of time is plotted, demonstrating that the spatial extent of the injected charge decreases with time. Briefly, these results were determined using an electrostatic model as follows. The AFM tip was approximated by a grounded metallic sphere and the electrostatic force interaction between the injected charge on the sample and the image charge in the grounded tip was calculated. The charge

was assumed to be only on the sample surface, to reduce the complexity of the computation, but in principle the model could be easily expanded to include three-dimensional charge distributions. The charge distribution consisted of a disc upon which was imposed a grid (typical grid spacing, 5 nm). In principle, any arbitrary 2-D charge distribution may be assigned to this grid, but for a first approximation, the total assigned charge was uniformly distributed over the grid points. Polarization effects were ignored as were effects on the tip motion due to the surrounding medium (such as hydrodynamic damping) [52], and the nanocrystal topography was replaced with a flat plane. The electrostatic interaction between the tip and sample was then found by taking each charged grid point, and finding the resultant image charge induced in the grounded tip. The total Coulomb force was subsequently calculated by summing up the interaction of each grid-point charge with each image charge, i.e.,

$$\vec{F}_{electrostatic} = \sum_{i,j} \frac{q_{s_i} q_{t_j}}{4\pi\varepsilon_o D_{ij}^2} \hat{d}_{ij} \tag{3.1}$$

with q_{s_i} the ith grid-point charge on the sample, q_{t_j} the jth image charge in the tip and D_{ij} the distance between them (and $\hat{d}_{ij}$ a unit vector). Thus the total force was made up of two terms: one term due to the van der Waal interaction (between a sphere and plane) [35], and the second from the electrostatic contribution (equation 3.1). Only the z-component of the total force was included since only the vertical forces on the tip were measured. It was assumed that the microscope feedback loop maintained the tip at a constant force gradient, set by and estimated from the imaging parameters, an assumption valid for small tip oscillation amplitudes (as compared to the tip-sample separation distance). This assumption holds when $F_{coulomb} \gg F_{vdW}$ i.e., in the charged region. The equation

$$\left(\frac{\partial F_z}{\partial z}\right)_{tot} = \left(\frac{\partial F_z}{\partial z}\right)_{vdW} + \left(\frac{\partial F_z}{\partial z}\right)_{electrostatic} = constant \tag{3.2}$$

was solved (using Newton's method) for the height of the tip above the flat plane as it scanned over the charged region. This calculated profile was then compared to the data. By adjusting the initially assumed charge and charged area iteratively, a "best

fit" was found.

From this analysis it was determined that in a typical experiment $\sim 350\pm90$ electrons (or ~ 4 electrons per particle) are injected and leak away at a rate of $\sim 35\pm15$e/min. The decrease of the spatial extent of the charge with time may be interpreted in two ways. The data is only consistent with lateral surface charge diffusion if the charge migrates such that the instantaneous local charge density is below the detection limit (estimated to be ~ 3 electrons for a point charge for typical imaging parameters). Measurements in a humid environment (compared to an atmosphere purged with N_2, i.e., Fig. 3.6) suggest a lateral component to the discharge does exist (possibly via surface states), though clear, slow, lateral dissipation was only seen in experiments done in air (i.e., humid environment), and has been seen to increase when the sample stage is not grounded. A second interpretation is that the main dissipation path is not along the surface, but to the substrate (with a local current density of ~ 0.2 nA/cm^2). Possible vertical transport mechanisms include hopping conduction (via nanoparticles or via defects, from ion implantation or charge injection), tunneling (direct or Fowler-Nordheim) or thermionic emission (see Section 3.6). No enhanced dissipation due to the tip has been observed and discharging via ions from the air has been shown to be too slow a process to be a substantial contributor [53].

To test the hypothesis that vertical transport might be due in part to a high conductance path created by the field applied to the tip during charge injection, we investigated the charge distribution in Fig. 3.15—i.e., a model charge distribution that has no charge in the center in order to mimic a high conductance path. When the high conductance path radius was on the order of 14 nm, a dip was seen in the calculated AFM scan (Fig. 3.16). As this is something never observed experimentally, we rule out the possibility of creating a high conductance path of this size. However, if the radius is shrunk to ~ 5 nm, the calculated trace is very similar to traces seen in experiments. Thus we can put an upper bound on any possible high conductance path created, but cannot rule out that possibility entirely. Lateral and vertical current measurements during discharging would help elucidate the discharge path, though would be very challenging due to the very small currents involved.
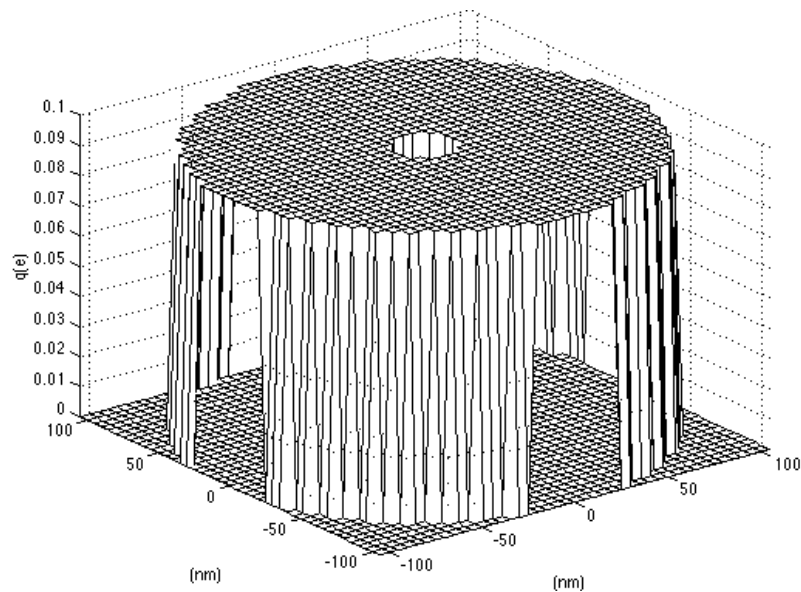
Figure 3.15: Charge distribution for test of transport via a high conductance path hypothesis.
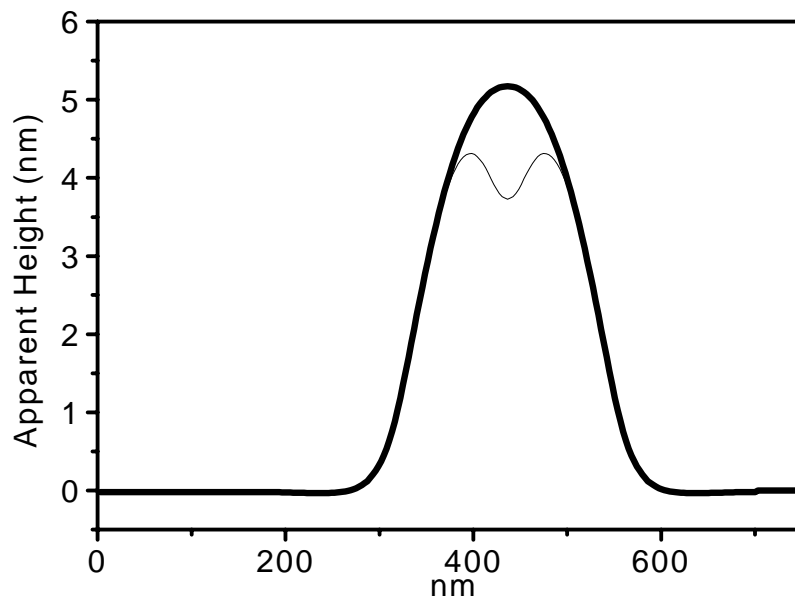
Figure 3.16: Effect of a high conductance path. Path radius about 14 nm (thin line) and path radius about 5 nm (thick line). A trace with no high conductance path is indistinguishable from the 5 nm case.

3.6   Charging: voltage and time dependence

In principle, if a nanocrystal's size is on the order of a nanometer, two charging effects can be seen if the charge is injected into the nanocrystal conduction band. First, because of quantum confinement and the discretization of the energy levels (see Chapter 1 and Fig. 3.17), a voltage threshold should exist, below which no charge can be injected, that is higher than that for a piece of bulk material. Second, because of the nanocrystal's small capacitance and the Coulomb blockade effect, steps should be seen in a charging versus voltage curve (due to the fact that the applied voltage is not high enough to lift the electron over the Coulomb barrier). As well, assuming good contact between the tip and particle, charging is expected to saturate with time.

To test the possibility that charge is injected into the conduction band of small nanoparticles, we performed charging versus voltage and charging versus charging time measurements. However, there are several flaws in this experiment. First, as mentioned above, it is difficult to accurately control the tip-sample spacing during charging, and thus reproducibility is a problem. Second, if the same location is repeatedly charged, it is difficult to know when all the charge has completely dissipated. Alternatively, if different locations are used, there may be spot-to-spot variations. Finally, as discussed in the previous section, the charge process itself may change the charging characteristics of the sample.

Figure 3.18 shows the variation of the apparent height of the charge signal with applied voltage. The experiment was done on an etched Si nanocrystal sample that had been air-exposed for several days. In general, the measurements were taken at 30–60 minute intervals, with the two important exceptions noted (charging time, 6 minutes). The general trend of the curve is that charging continues to increase with applied voltage. There is indeed a plateau in the curve, but its extent, together with the noise in the data, make it unreasonable to attribute it to Coulomb blockade effects. The three points at -4 V demonstrate the variation due to the difficulty of controlling the tip-sample separation. The middle value of the three measurements was taken at slightly different location, suggesting that spot-to-spot variation is less of a problem
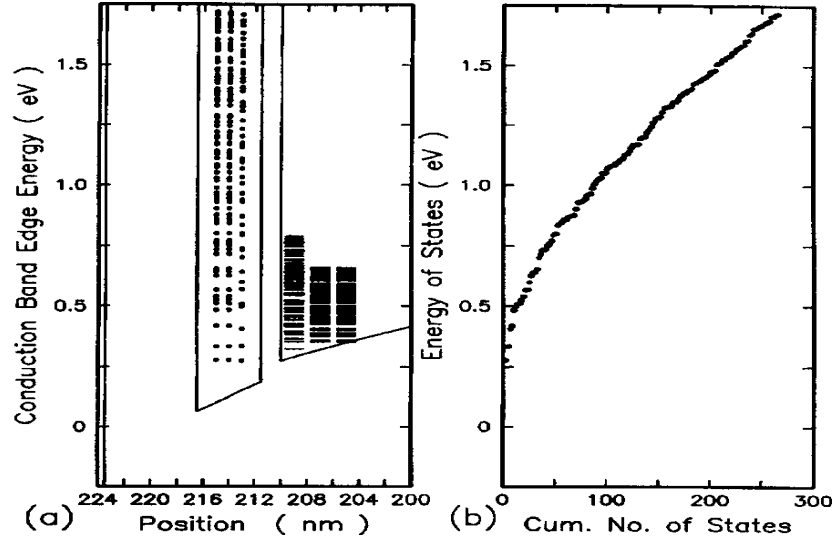
Figure 3.17: (a) Schematic showing the energy levels in a nanocrystal and adjacent Si substrate, separated by a 1.5 nm oxide, and (b) total number of states as a function of energy. A 5 nm box represents the nanocrystal and the device is under 2.5 V bias. From Ref. [54].
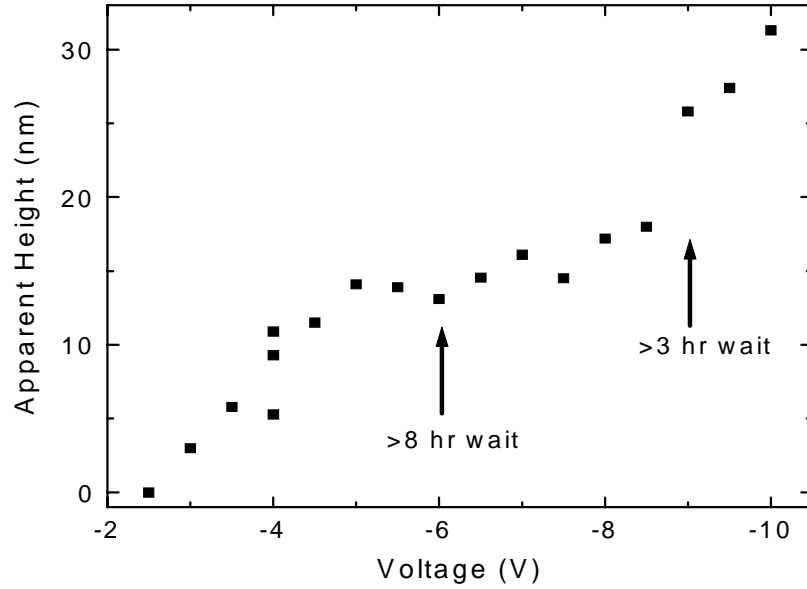
Figure 3.18: Apparent height of charge protrusion as a function of applied bias. No charging was seen for an applied voltage smaller than −2.5 V. The measurements were taken at approximately 30–60 minute intervals with the notable exceptions marked.
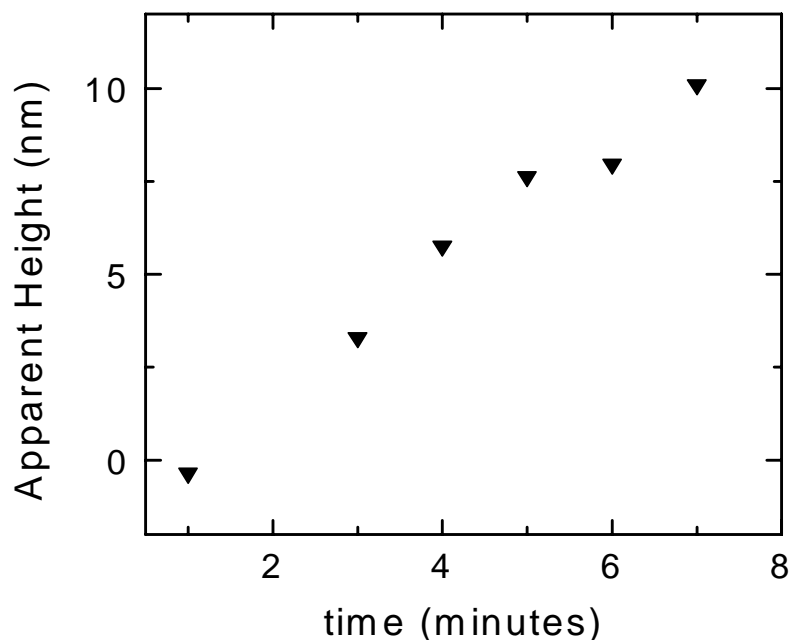
Figure 3.19: Apparent height of charge protrusion as a function of charging time (i.e., the amount of time the tip and sample are in contact with a voltage applied).

than tip-sample separation control. No charging was seen below -2.5 V—this is the threshold voltage for this sample.

Figure 3.19 shows the apparent height of the charge signal as a function of charging time (i.e., time the tip and sample are in contact with a voltage applied). The applied voltage was -7 V and the same sample was used. If the tip made good electrical contact with isolated nanocrystals, the apparent height would saturate at a very short time. This is not the case seen here, however, which indicates that charging is a much slower process and good electrical contact is not made.

The question of the precise charging mechanism is a difficult one. Figure 3.20 is a schematic band diagram that shows four possibilities. The schematic represents a highly doped Si tip, covered with a thin native oxide, separated by a thin air gap from an oxide covered Si nanocrystal (NC) on a grounded Si substrate (where band bending is ignored). One possible charging mechanism is hot electron transport or thermionic emission over the oxide barrier (possibly combined with breakdown of the air gap). A
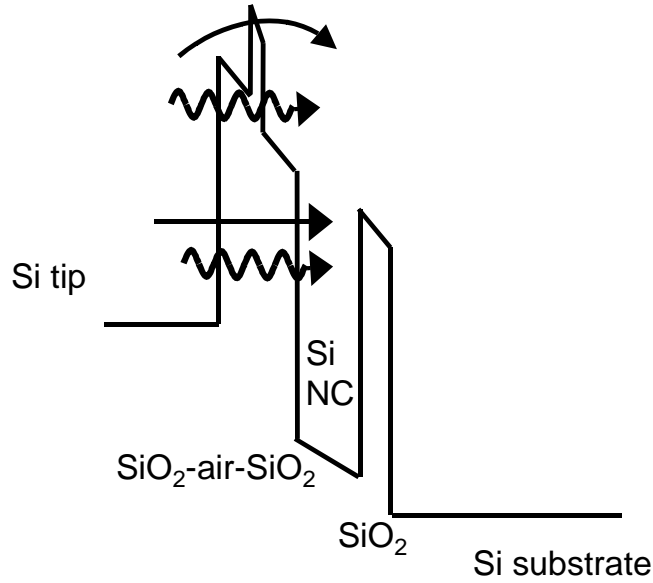
Figure 3.20: Schematic band diagram for charging showing four possible charge injection mechanisms: hot electron transport (curved arrow), Fowler-Nordheim tunnelling (curly arrow through the triangular part of the barrier), oxide breakdown (straight arrow), and direct tunnelling (lower curly arrow).

second is Fowler-Nordheim tunnelling [55] or strong field emission, i.e., field-assisted tunnelling through the triangular part of the barrier. Oxide breakdown is also a contender. Oxide breakdown involves the production of a high conductance path once the density of traps or defects (arising from stressing the oxide with applied voltages or currents) reaches a critical density [56]. Finally, if the barriers are thin enough, direct tunnelling through them is also possible. More detailed measurements of parameters such as charging threshold are needed as well as voltage and temperature dependent current measurements to determine the dominant charging mechanisms.

3.7 Summary

Atomic force microscopy is a useful technique to inject and detect charge on the nanoscale in technologically relevant materials such as Si nanoparticle-containing SiO_2 films. Using an AFM it is demonstrated that the charge trap centers in annealed,

Si implanted silicon dioxide films are due to the presence of nanocrystals and not simply due to process-induced defects in SiO_2. However, AFM charge injection is very sensitive to surface treatments, tip shape and size, and tip-sample spacing during charging. With the help of calculations (which will be discussed in more detail in the next chapter), the magnitude of the injected charge and the rate of its dissipation may be estimated.

Chapter 4   Two models for quantitative charge imaging by atomic force microscopy

4.1   Introduction

The ability to easily detect charge at the single electron level is becoming increasingly important as interest in charge storage at the few electron scale grows. The atomic force microscope [24] is a useful tool to detect small numbers of charges [38] as well as to inject charge into a localized region [34, 40–42, 57–59]. However, quantitative measurement of electrostatic charge has never been straightforward because of the complex factors involved such as tip shape, tip-sample distances, contamination or oxidation of tip and sample, and the exact nature of the tip-sample interaction. Models, varying in complexity from a parallel plate capacitor to finite element calculations, are always needed to interpret results quantitatively.

The first uses of the AFM to detect electrostatic forces modeled the system as a parallel plate capacitor [25] or considered the tip to be a point object [60]. Since then several different methods have been proposed for calculating the electrostatic force, ranging from simple analytical calculations [61, 62] and perturbative approaches [63] to more complex numerical simulations [64–69]. Much work has also been done in modeling of the tip-sample interaction in atomic force microscopy [52, 70–77]. In this chapter we combine both electrostatic and AFM modeling to interpret AFM images of charge. We describe two models for quantitative charge imaging, one appropriate for non-contact mode imaging, the second for intermittent contact (tapping) mode imaging.

4.2   Experiments

The models described in the next sections have been applied to two experimental situations, details of which may be found in previous chapters. Briefly, the non-contact mode experiments (Chapter 3) involved Si nanocrystal samples consisting of 100 nm silicon dioxide layers (wet thermally grown on Si substrates) that were implanted at room temperature with 35 keV Si^+ ions to a fluence of $4x10^{16}$ Si/cm^2. The samples were annealed at 1100^oC for 10 minutes in vacuum (base pressure $< 8x10^{-7}$ torr) to allow the nucleation and growth of silicon nanocrystals (size $\sim$ 2–6 nm). The AFM used was a Park Scientific (Thermomicroscopes) Autoprobe CP, operating in non-contact mode (driving frequency above resonance) using highly doped Si tips (spring constant $k \sim 3$ N/m) on triangular cantilevers from commercial sources [46]. Charge was injected into the samples by applying a voltage to the AFM tip, disengaging the microscope feedback and lowering the tip toward the sample. After charge transfer the feedback was re-engaged, the tip grounded and non-contact mode images made.

The tapping mode experiments (Chapter 2) involved samples of isolated Si nanocrystals made by an aerosol method and deposited on a 100 nm thermally grown SiO_2 layer on an Si substrate. In this case, the AFM tip was used to inject charge into isolated single nanoparticles that were subsequently imaged in tapping mode. The microscope was a Digital Instruments Nanoscope III (driving frequency below resonance) and the tips were Cr-coated Si (spring constant $k \sim 2$ N/m, from DI) on rectangular cantilevers.

4.3   Electrostatic model

The electrostatic force between the grounded tip and charged sample was calculated using the method of images. The tip (Cr-coated or made of highly doped Si) was approximated as a grounded, metallic sphere. This shape was chosen as it is an adequate approximation for our experiments (tip-sample distance d . 10 nm) and is simpler than more realistic conical geometries [64, 78]. With tip doping $> 10^{19}$ cm^{-3}
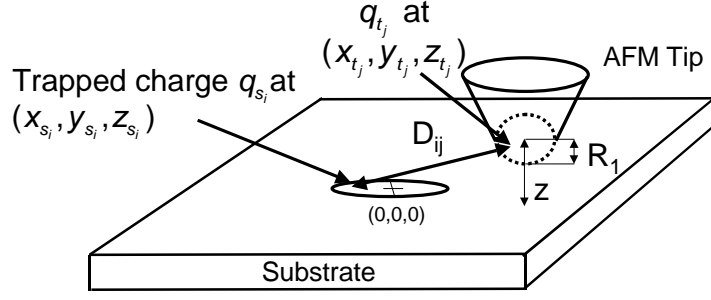
Figure 4.1: Schematic for non-contact mode model.

and the resultant Debye length < 5 Å, treating the Si tip as metallic is an excellent assumption for typical average tip-sample spacing in non-contact mode. The charge on the sample was assumed to be only on the surface and the charge distribution consisted of a disc or shell upon which was imposed a grid (typical grid spacing, 5 nm). The total charge was distributed uniformly over the grid points and any polarization effects and image charge in the substrate were ignored. These assumptions are justified for our particular samples, where a thick oxide separates the charge and the substrate and the charge is believed trapped on a circular area on the surface (ion implanted samples) or on the nanocrystal surface (single Si particle samples) as a result of the charge injection process. This is a first approximation—the model may be expanded to include arbitrary two or three-dimensional charge distributions, materials effects [62] and more realistic tip shapes. The electrostatic interaction between the tip and sample was found by taking each charged grid point and finding the resultant image charge induced in the grounded tip [79]. Once all the image charges (i.e., one for each grid point) were determined, the total Coulomb force was found by summing the interaction of each grid point charge with each image charge, i.e.,

$$\vec{F}_{electrostatic} = \sum_{i,j} \frac{q_{s_i} q_{t_j}}{4\pi\varepsilon_o D_{ij}^2} \hat{d}_{ij} \tag{4.1}$$

where q_{s_i} is the ith grid point charge, q_{t_j} is the jth image charge, D_{ij} the distance between them and $\hat{d}_{ij}$ a unit vector (see Fig. 4.1).

4.4 Model for non-contact mode imaging

Most ambient atomic force microscopes produce topographic images by exciting the AFM cantilever close to its resonant frequency and using a feedback signal to adjust the tip-sample spacing so that the cantilever's oscillation amplitude remains constant at a set-point value. In true non-contact mode, the oscillation amplitude of the cantilever is much smaller than the tip-sample spacing, and the AFM feedback may be said to maintain a constant force gradient between tip and sample [52]. For this statement to hold, the tip must never "tap" the surface (i.e., the interaction may only involve van der Waals forces and no contact potentials) and the tip may sample only a small part of the force curve during a period of oscillation. It is also assumed in this case that the tip-surface interaction affects only the resonant frequency of the cantilever, and does not significantly influence the tip oscillation amplitude at resonance. Finally, $k \gg F'_{t-s}$ is another condition required, where k is the spring constant of the cantilever, and F'_{t-s} is the force gradient between tip and sample, so that the force gradient is only a small perturbation to the harmonic motion of the cantilever [29]. In this case, the tip-sample force F_{t-s} can be expanded to first order, $F_{t-s}(z) \sim F_{t-s}(z = z_{L0}) + F'_{t-s}(z = z_{L0})(z - z_{L0})$ (z_{L0} is the equilibrium position of the tip), and F'_{t-s} has the effect of changing the effective spring constant of the cantilever so that $k_{eff} = k - F'_{t-s}$, thus producing a shifted resonant frequency,

$$\tilde{\omega}_o = \sqrt{\frac{k_{eff}}{m^*}} \tag{4.2}$$

where m^* is the effective mass of the cantilever. Please note that even though a microscope operating mode may be called "non-contact," if the conditions stated above are not fulfilled, this model is not valid and the tapping mode model of Section 4.5 must be used.

4.4.1   The model (non-contact mode, nanoparticle ensemble)

To produce calculated images of charge for non-contact mode imaging, we chose to solve (using Newton's method) the following equation,

$$\left(\frac{\partial F_z}{\partial z}\right)_{tot} = \left(\frac{\partial F_z}{\partial z}\right)_{vdW} + \left(\frac{\partial F_z}{\partial z}\right)_{electrostatic} = constant \qquad (4.3)$$

for z, the height of the center of the tip above a flat plane (see Fig. 4.1). Note that we consider only the z-component of the force since in normal AFM operation only that component is sensed. We include only van der Waals and electrostatic forces and omit the negligible contribution from air damping. Here the "*constant*" represents the set-point force gradient which is related to the set-point amplitude in the following way. The tip amplitude as a function of frequency ω is [80]

$$A(\omega) = \frac{a_d \omega_o^2}{\sqrt{(\frac{k - F'_{t-s}}{m^*} - \omega^2)^2 + \frac{\omega_o^2 \omega^2}{Q^2}}} \qquad (4.4)$$

(with A, the measured oscillation amplitude, a_d, driving amplitude, ω_o, resonant frequency of cantilever, m^*, effective mass, Q, quality factor, k, spring constant, F'_{t-s}, force gradient), so assuming a_d, ω_o, ω, m^*, Q, and k are constants, maintaining a constant cantilever amplitude may be considered equivalent to maintaining a constant force gradient. The set-point force gradient may be found experimentally by measuring the resonant frequency and the resonant frequency shift and using the approximation $\frac{\Delta\omega}{\omega_o} \approx \frac{1}{2}\frac{F'}{k}$ (where $\Delta\omega = \omega_o - \tilde{\omega}_o$), found by expanding the expression (4.2) above.

The equation for the van der Waals force gradient was found by taking the derivative and z-component of the following expression determined by integrating the Lennard-Jones pair potential, assuming a spherical shape for the tip and a flat plane for the sample, (valid for $z << R$) [80]:

$$\vec{F}_{vdW} = \frac{HR}{6z^2}\left(-1 + \frac{\sigma^6}{30z^6}\right)\hat{z} \qquad (4.5)$$

symbol	parameter	value	source
ρ_{Si}	number density of Si	$5.0\mathrm{x}10^{22}$ cm^{-3}	[81]
$\rho_{\mathrm{SiO_2}}$	number density of SiO$_2$	$6.81\mathrm{x}10^{22}$ cm^{-3}	[82]
ε	Lennard-Jones potential parameter (for Ar)	$1.67\mathrm{x}10^{-21}$ J	[83]
σ	Lennard-Jones potential parameter (for Ar)	0.34 nm	[83]

Table 4.1: Parameters for estimation of Hamaker constant

The symbol H represents the Hamaker constant and was estimated from $H = 4\pi^2\varepsilon\rho_{\mathrm{Si}}\rho_{\mathrm{SiO_2}}\sigma^6 \sim 3\mathrm{x}10^{-19}$ J (symbols and values in Table 4.1), and R is the tip radius of curvature, measured from scanning electron micrographs ($2 * R \sim 105$ nm). The electrostatic contribution is found by taking the derivative and z-component of equation (4.1).

4.4.2   Model results

Figure 4.2 shows an experimental line scan (solid line) of a charged region of an etched SiO$_2$ film containing silicon nanocrystals [58] superimposed on a calculated AFM scan (dotted line), determined using the model described in 4.4.1. The injected charge is imaged as a protrusion on the surface due to the extra electrostatic force interaction between the charged sample and the induced image charge in the tip. The calculated AFM scan was found by first assuming a charge distribution (i.e., total charge and charge disc radius), calculating a scan, comparing the result to the experimental data, then adjusting the charge distribution and recalculating the result and so on until a best fit to the two parameters (charge and disc radius) was found [58]. From the model, the imaged charge in Fig. 4.2 was estimated to be ~ 350 electrons, over an area of radius 170 nm (~ 60 nC/cm^2).

4.4.3   Charge sensitivity

When analyzing charge storage devices and imaging small numbers of charges, it is important to know the sensitivity of the technique being applied. For this reason, the model of Section 4.4.1 was used to estimate the AFM sensitivity to charge in non-contact mode. The error in the height measurement was estimated to be
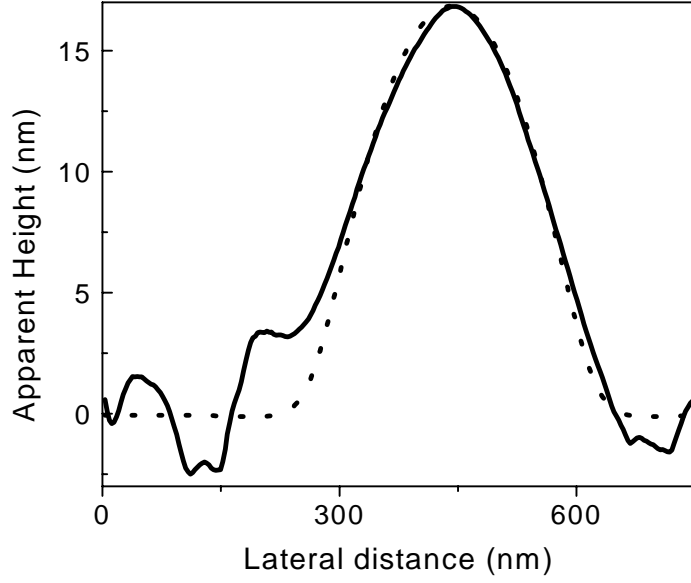
Figure 4.2: Experimental image (solid line) and calculated image (dotted line) of charge deposited in an SiO_2 film containing Si nanocrystals. Estimated charge: $\sim$350 electrons, over an area of radius 170 nm ($\sim$60 nC/cm^2).

$\sim 0.4-0.7$ nm by repeated measurement of a 4 nm particle under regular conditions. Figure 4.3 shows how the minimum detectable number of electrons varies with tip-sample spacing for three different types of charge distributions: a point charge (¥), charge spread out over a disc with radius 30 nm (●) and charge over an area with a 60 nm radius (N). The non-intuitive result is that the microscope is more sensitive to charge as the tip-sample spacing increases. This can be attributed to the fact that the van der Waals force falls off more quickly with distance than the electrostatic force—thus as the tip moves away from the sample, the relative contribution of the electrostatic force gradient to the total force gradient increases with respect to the van der Waals contribution. This curve reaches a minimum when the minimum detectable change in force gradient (estimated to be $\sim 10^{-5}-10^{-6}$ N/m [29]) due to electrostatic forces is reached at a height of ~ 50 nm. Note that a particular system or choice of parameters might result in a larger minimum detectable change in force gradient, and thus a smaller optimal height for electrostatic force detection.

Figure 4.4 shows the variation of the minimum detectable number of electrons as a function of tip radius. This result shows that the greatest sensitivity is found when the charge distribution is of order the same physical size as the tip—for a point charge, the greatest sensitivity occurs with a small tip, for an extended charge, the greatest sensitivity requires a larger tip. In this way the z-component of the force is maximized while the relative contribution of the van der Waals force is minimized as much as possible. From these calculations we estimate that the greatest charge sensitivity of an AFM operating in non-contact mode with typical parameters and cantilevers is on the order of a few electrons. Single electron resolution in normal AFM operation would require parameter optimization.

4.5   Tapping mode model

When the tip oscillation amplitude is large compared to the tip-sample spacing, the tip now experiences a wide range of force values during an oscillation cycle, including a repulsive contact force when it "taps" the surface. In this case the conditions stated in Section 4.4 no longer hold and a simple "non-contact" model can no longer be used. The microscope feedback still maintains a constant tip oscillation amplitude during scanning, but now the amplitude as a function of driving frequency can no longer be approximated by an analytical expression such as equation (4.4), and the amplitude at a specific tip-sample distance must be found by other means. To investigate this situation we take the cantilever to be a point mass of effective mass m^* at the end of a massless spring ($m^* = nm$, where m is the mass of the cantilever, and n depends on the cantilever geometry [84]). We examine the equation for a forced harmonic oscillator:

$$m^* \ddot{z} + \gamma \dot{z} + k(z - z_{L0}) = F_o \cos(\omega t) + [F_{t-s}(z, t)]_z \qquad (4.6)$$

where k is the cantilever spring constant, m^* the effective mass, z_{L0} the equilibrium position of the cantilever, $F_o = ka_d$ with a_d the driving amplitude, γ is the damping constant, ω is the angular driving frequency (chosen slightly below resonance,
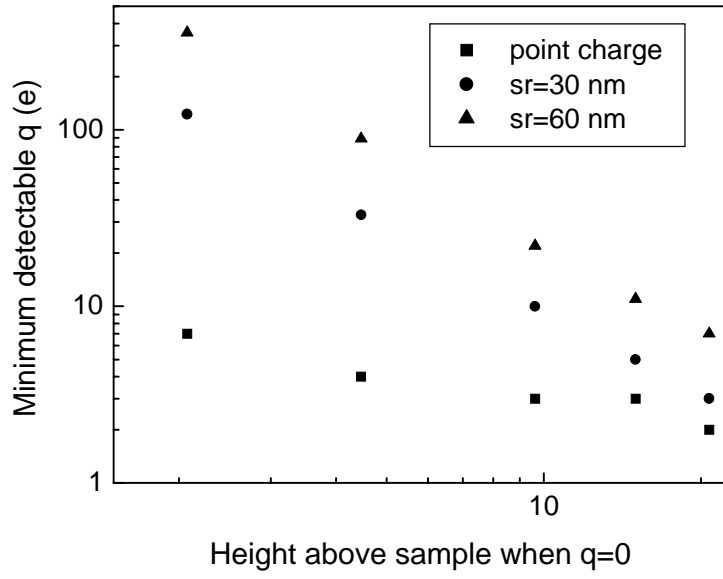
Figure 4.3: Minimum detectable number of electrons as a function of the tip-sample spacing (tip radius $R_1 \sim 52$ nm, charged region radii sr=0, 30 and 60 nm). Note the counter-intuitive result that the charge sensitivity increases with increasing distance, due to the fact the van der Waals force falls off more quickly with distance than the electrostatic force.
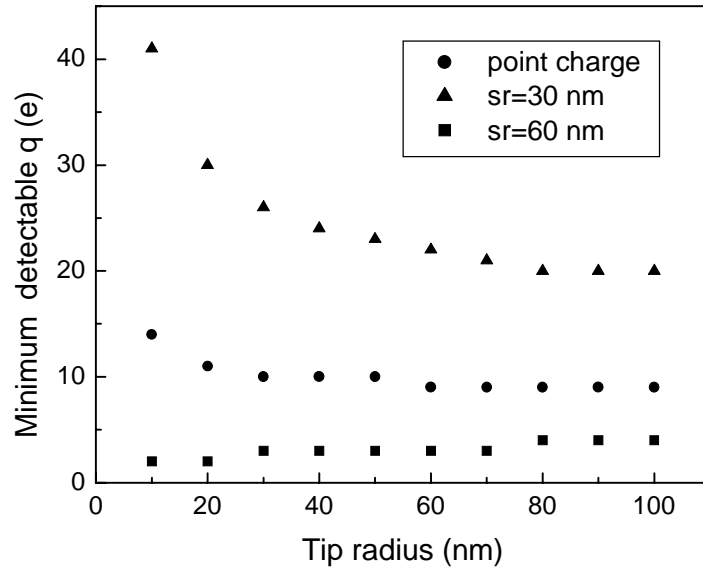
Figure 4.4: Minimum detectable number of electrons as a function of tip radius. Note that the best sensitivity occurs when the tip is of the same size as the charge distribution.

see Table 4.2 for values used) and $[F_{t-s}(z,t)]_z$ is the z-component of the tip-sample interaction force. This last term has three components: one due to the contact or tapping force interaction, one from the van der Waals force, and the third from the electrostatic force.

4.5.1   The model (tapping mode, single nanoparticle)

For this model, we considered a charged spherical particle (see Fig. 4.5). The electrostatic force was calculated as described in Section 4.3, by taking the tip at its mean height above the sample during an oscillation and finding the Coulomb interaction between the charge on a half or full shell grid on the particle surface and the induced image charge in the grounded tip. For the van der Waals force, the interaction (a) between two spheres (the tip and particle) and (b) a sphere and plane (the tip and substrate) were added, using the full equations of Hamaker [35]:

$$\vec{F}_{vdW} = \begin{cases} -\frac{H}{3} \left(\frac{32R_1^3 R_2^3 (r+\xi_o+R_1+R_2)}{(r+\xi_o)^2 (r+\xi_o+2R_1)^2 (r+\xi_o+2R_2)^2 (r+\xi_o+2(R_1+R_2))^2} \right) \hat{r} & \text{(a)} \\ \frac{H}{24R_1} \left(\frac{2}{x} - \frac{1}{x^2} - \frac{2}{x+1} - \frac{1}{(x+1)^2} \right) \hat{z}, \ x = \frac{(d+\xi_o)}{2R_1} & \text{(b)} \end{cases} \quad (4.7)$$

where d and r are defined in Fig. 4.5. The parameter ξ_o is determined by matching the value of F_{vdW} with the contact force at contact. Here contact is defined as the tip-sample position at which contact mechanics must be applied. Note that the dimensions d and z in Fig. 4.5 are measured with respect to the surface of the plane when the AFM tip is not in close proximity. For large energies of adhesion, however, the plane and tip may bulge toward each other, meaning contact may occur for $d > 0$.

The question of what form the contact force should take is not a trivial one [71, 86, 87]. Some possibilities are the Hertz theory [88] (includes no adhesion), the JKR theory (good for soft samples) [36], the DMT theory (best for rigid samples) [89], the JKR-DMT transition formalism (appropriate for all tip-sample parameters) [90], MYD/BHW theory (a general theory) [91, 92], and the impact oscillator model (consisting of a harmonically driven harmonic oscillator undergoing impacts with an infinitely rigid object) [93, 94]. In considering these theories we assume the tip
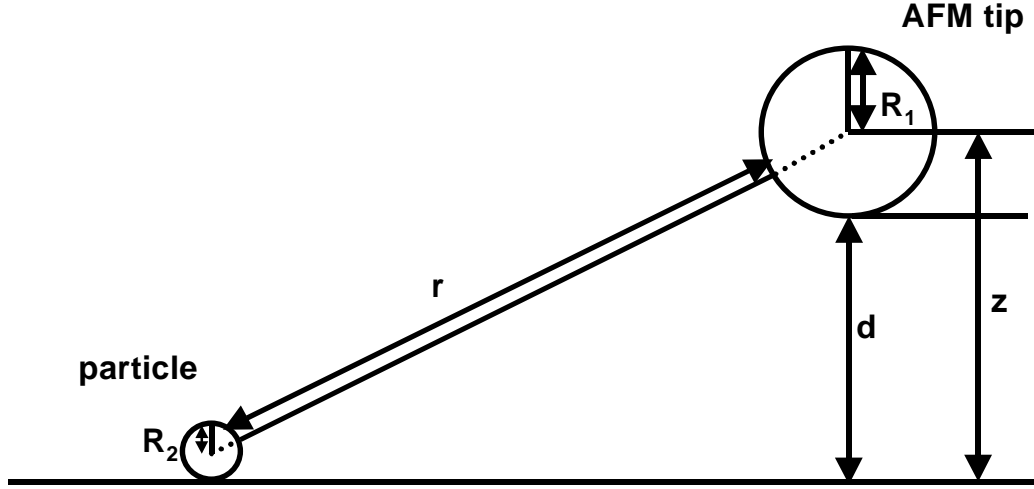
Figure 4.5: Definition of symbols in tapping model equations.

symbol	parameter	value	source
k	spring constant	2.16 N/m	$k = \frac{Ewt^3}{4l^3}$ [80], E (Young's modulus of Si) = 1.3x10^{11} N/m^2, w (width) = 28 μm, t (thickness) = 3 μm, l (length) = 225 μm [85]
m^*	effective mass	1x10^{-11} kg	$m^* = \frac{k}{\omega_0^2}$ or $0.24m$ [84]
a_d	driving amplitude	0.22 nm	Found by matching the calculated and measured free amplitudes (32 nm).
γ	dissipation coefficient	3x10^{-8} kg/s	$\gamma = \frac{m^*\omega_0}{Q}$, ω_o measured, $Q = \frac{\omega_0}{\Delta\omega}$, $\Delta\omega$ equal to width of resonance, i.e., width at $\frac{1}{\sqrt{2}}A_{\max}$ on an amplitude-frequency curve.

Table 4.2: Parameters for tapping mode model

symbol	parameter	value
R_1	tip radius of curvature	50 nm
R_2	sample radius of curvature	14 nm (particle) ∞ (plane)
R	reduced radius of curvature, $\frac{1}{R} = \frac{1}{R_1} + \frac{1}{R_2}$	11 nm (particle) 14 nm (plane)
W	work of adhesion	0.756 J/m^2
z_o	equilibrium interatomic distance	0.34 nm
H	Hamaker constant	1.8x10^{-18} J
E^*	reduced elastic modulus, $\frac{1}{E^*} = \frac{(1-\nu_t^2)}{E_t} + \frac{(1-\nu_s^2)}{E_s}$	5.8x10^{10} N/m^2

Table 4.3: Constants and material parameters for contact interaction I

and sample are elastic and ignore shear forces [87], hydrodynamic damping (small compared to the other forces involved) [52], and other possible contributions to the total force such as capillary forces. Our goal here was not to perfectly model the tapping interaction, but rather to use an applicable model to interpret charge images. To this end we investigated briefly both the JKR and DMT theories.

The parameter μ first defined by Muller et al. [91] may be used to delineate which of the JKR and DMT theories should be applied.

$$\mu = \frac{32}{3\pi} \left[\frac{2RW^2}{\pi E^{*2} z_o^3} \right]^{\frac{1}{3}}$$

See Tables 4.3 and 4.4 for symbol definitions. Roughly speaking, for $\mu \gg 1$, JKR is the better theory to choose (i.e., for soft samples, large energy of adhesion and large tip radii) and when $\mu \ll 1$, DMT is the appropriate theory (i.e., for rigid systems, low adhesion, and small radii of curvature) [95]. In our experiments in tapping mode, we have used an Si tip coated with chromium on Si samples covered with a native or thermally grown oxide [59] and hence estimate a value of the adhesion energy W ($W = W_{12} \sim 2\sqrt{\gamma_1^d \gamma_2^d}$ [96]) from the surfaces energies of Cr ($\gamma_1^d \sim 2070$ mJ/m^2 [97]) and SiO$_2$ ($\gamma_2^d \sim 70$ mJ/m^2 [98]). With the appropriate parameters for our experiments (see Tables 4.3 and 4.4) we get values of $\mu \sim 2$ for the flat part of our samples and $\mu \sim 1$ when imaging a 28 nm particle. While we are clearly in the JKR-DMT transition regime, we have chosen to look at the simpler JKR and DMT theories separately.

symbol	parameter	material	value	source
E_t	Young's modulus of tip	Cr	27.9×10^{10} N/m^2	[99]
E_s	Young's modulus of sample	SiO$_2$	7×10^{10} N/m^2	[100]
ν_t	Poisson's ratio for tip	Cr	0.21	[99]
ν_s	Poisson's ratio for sample	SiO$_2$	0.17	[100]

Table 4.4: Constants and material parameters for contact force II

4.5.2 JKR theory

For the JKR theory, the relationship between the force (F_{JKR}) and penetration depth (d) is:

$$
\begin{aligned}
a^3 &= \frac{3R}{4E^*} \left(F_{JKR} + 3\pi W R + \sqrt{6\pi W R F_{JKR} + 9\pi^2 W^2 R^2} \right) \qquad (4.8) \\
d &= \frac{a^2}{R} - \sqrt{\frac{2\pi W a}{E^*}}
\end{aligned}
$$

where a is the radius of the contact region. Figure 4.6 shows a calculated force-distance curve. Equation (4.7) was used when the tip and sample were not in contact and equation (4.8) when in contact (taking the z-component, see Tables 4.3, 4.4 for parameters).

Figure 4.7 shows how the calculated tip amplitude varies with frequency when the mean tip-sample spacing is 150 nm (i.e., free, solid line) and when the mean tip-sample spacing is 20 nm (i.e., tapping, dotted line). These curves were generated by solving equation (4.6) using Matlab/Simulink (ode45, based on an explicit Runge-Kutta (4,5) formula, the Dormand-Prince pair); different sets of initial conditions were chosen and the equation was allowed to evolve with time until it reached a steady state in each case. Figure 4.8 shows an example of the tip motion as it comes to its equilibrium amplitude. Note that in Fig. 4.7, more than one amplitude at a specific frequency is possible in the curve generated at a tip-sample height less than the free amplitude (¨)—whether the system settled into one steady state or another depended on what initial conditions were chosen. This result for a tapping amplitude-frequency curve is qualitatively similar to experimental and computational
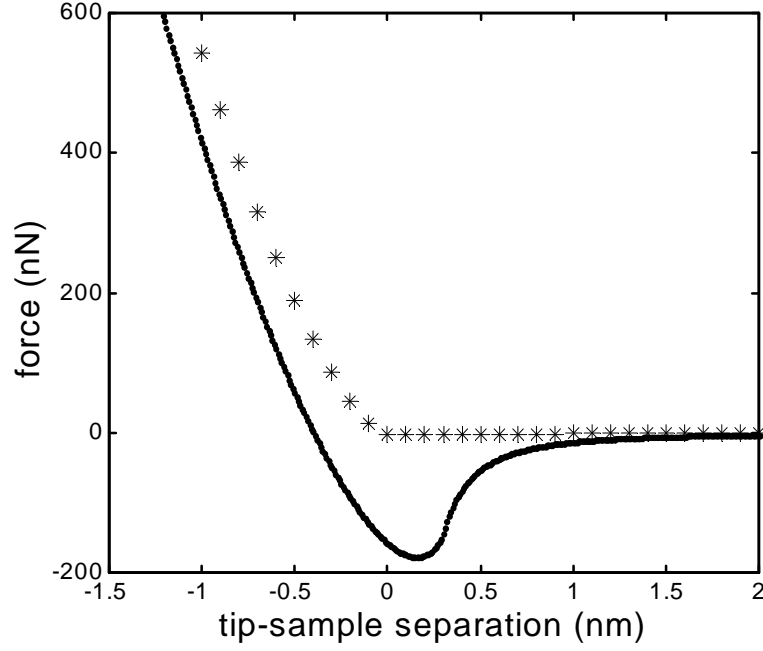
Figure 4.6: Force-distance curves for a 50 nm radius Cr-coated tip and an SiO$_2$ sample, using the JKR theory for the contact force with $W = 756$ mJ/m^2 ($\bullet$) or the DMT theory with $W = 10$ mJ/m^2 ($*$).

results seen by others [72–76, 101–103], with its truncated, extended peak. However, differences include curvature to the "flat" part of the truncated peak, the width of the plateau, and the small region just below resonance where in principle three solutions are possible.

Figure 4.9 shows a calculated amplitude-distance curve above a 28 nm particle (cantilever driven below resonance). The tip was brought in slowly from far away, and the tip motion was allowed to evolve for 1.2–3.6 ms at tip-sample spacing d, before moving to $d + \Delta d$ ($\Delta d = 0.1$ nm typically). Far from the sample, the tip oscillation amplitude is constant, then is seen to increase slightly before decreasing linearly with tip-sample spacing. The initial increase in amplitude is due to the fact that the resonance frequency $\tilde{\omega}_o$ is shifting down toward the cantilever driving frequency as the tip interacts with the attractive force of the sample. Occasionally in these amplitude-distance curves, discontinuous jumps to another solution were seen (see Fig. 4.9 (a)),
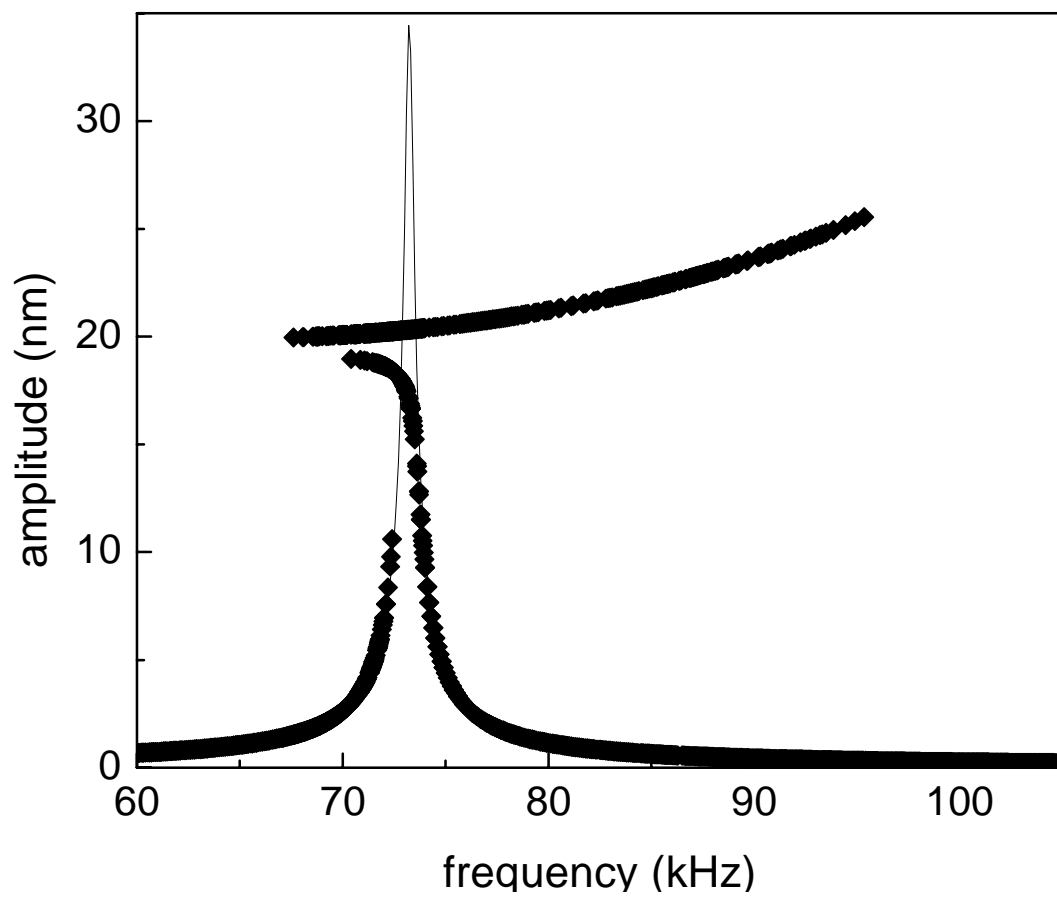
Figure 4.7: Amplitude versus frequency curves: solid line, mean tip-sample spacing 150 nm, (¨) mean tip-sample spacing 20 nm. Note that when tapping more than one amplitude at the same frequency is possible.
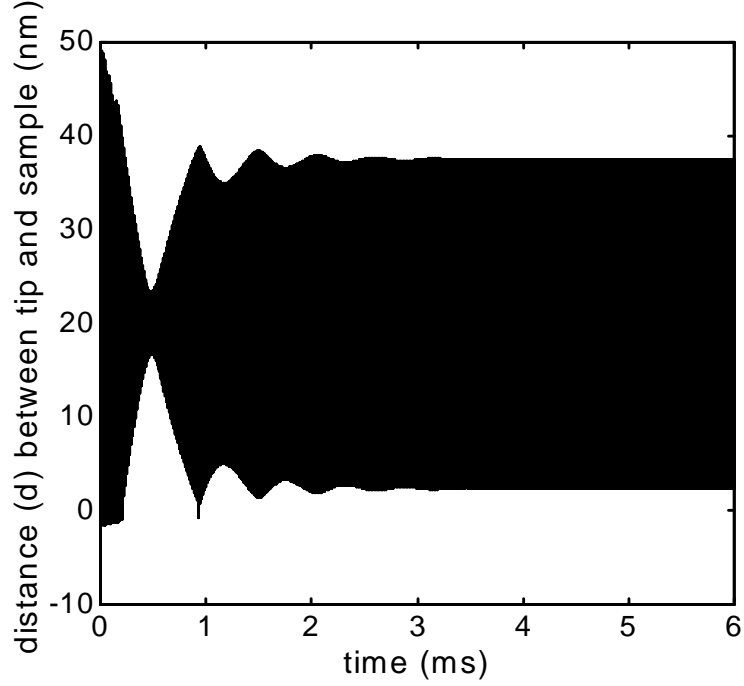
Figure 4.8: Tip motion as a function of time as it evolves to steady state.

especially when the tip-sample spacing was small, or when the amplitude-distance curve was generated above a particle (i.e., weaker tip-sample forces). The existence of the discontinuity also depended on Δd, suggesting more of a dependence on initial conditions [102] than on the strength or other property of the attractive force [104]. The features we find are similar to those seen by others experimentally and computationally [101, 105], and are qualitatively similar to our experimental traces. Unlike Anczykowski et al. [105], we calculate a step-like discontinuity for a driving frequency less than the resonant frequency. Experimentally (for $\omega > \omega_o$) when lowering the tip towards the sample, we have also seen a discontinuous jump in the amplitude accompanied by a phase shift, as discussed in the literature [101, 104, 106, 107].

If instead of slowly lowering the tip and allowing its motion to evolve, various initial conditions (position and velocity) are chosen for the tip at each height d, we generate an amplitude-distance curve as seen in Fig. 4.10. Here we have two tip-sample separations possible for one amplitude—the particular solution is again

determined by which initial conditions are chosen. The solution dependence on the initial position of the tip (z_i) with initial velocity zero was briefly investigated. It was found that when the tip was "plucked" with large displacement (i.e., z_i larger than the maximum z at steady state amplitude), two solutions were possible, but when $z_{steady\_state}^{\min} < z_i < z_{steady\_state}^{\max}$, in general only one solution was found though occasionally two were seen (see Fig. 4.11). Thus there exist sets of initial conditions (or points in phase space) that lead to particular solutions [102, 108]. This phenomenon has been used to explain distortion in experimental images [101, 102, 108, 109] and the switch from one solution to the other has been attributed to a transition from a purely attractive to a partly repulsive interaction regime [101, 105, 110].

To test this hypothesis, all the attractive forces in the force lookup table generated in the model were set to zero and an amplitude-distance curve was calculated. Next, the same procedure was repeated but this time all the repulsive forces were set to zero. Finally, a third amplitude-distance curve was produced without altering the initial force table. The results are shown in Fig. 4.12. These results demonstrate that the increase in amplitude before the linear decrease depends on the attractive force. They also support the idea that the discontinuities in amplitude-distance curves are the result of switching from a purely attractive to a partly repulsive interaction regime, since such a discontinuity is only seen in the case where both attractive and repulsive forces are present. As well, note that before the discontinuity occurs, the amplitude-distance curve is virtually identical to the attractive-force-only case, and after the discontinuity, the curve is very similar to the repulsive-force-only case.

To produce a calculated tapping mode image and ensure we arrive at an appropriate solution, at each lateral position we produce an amplitude-distance curve (such as Fig. 4.9) and find the tip-plane separation necessary to maintain the set-point amplitude. It was found that the image of a 28 nm particle calculated in this way produced a particle height that was slightly depressed. The error increased with decreasing particle size and with increasing energy of adhesion (W)—the latter suggests structures of different materials of the same height may produce slightly different AFM results. This depression in height was attributed to the fact that both the van der Waals
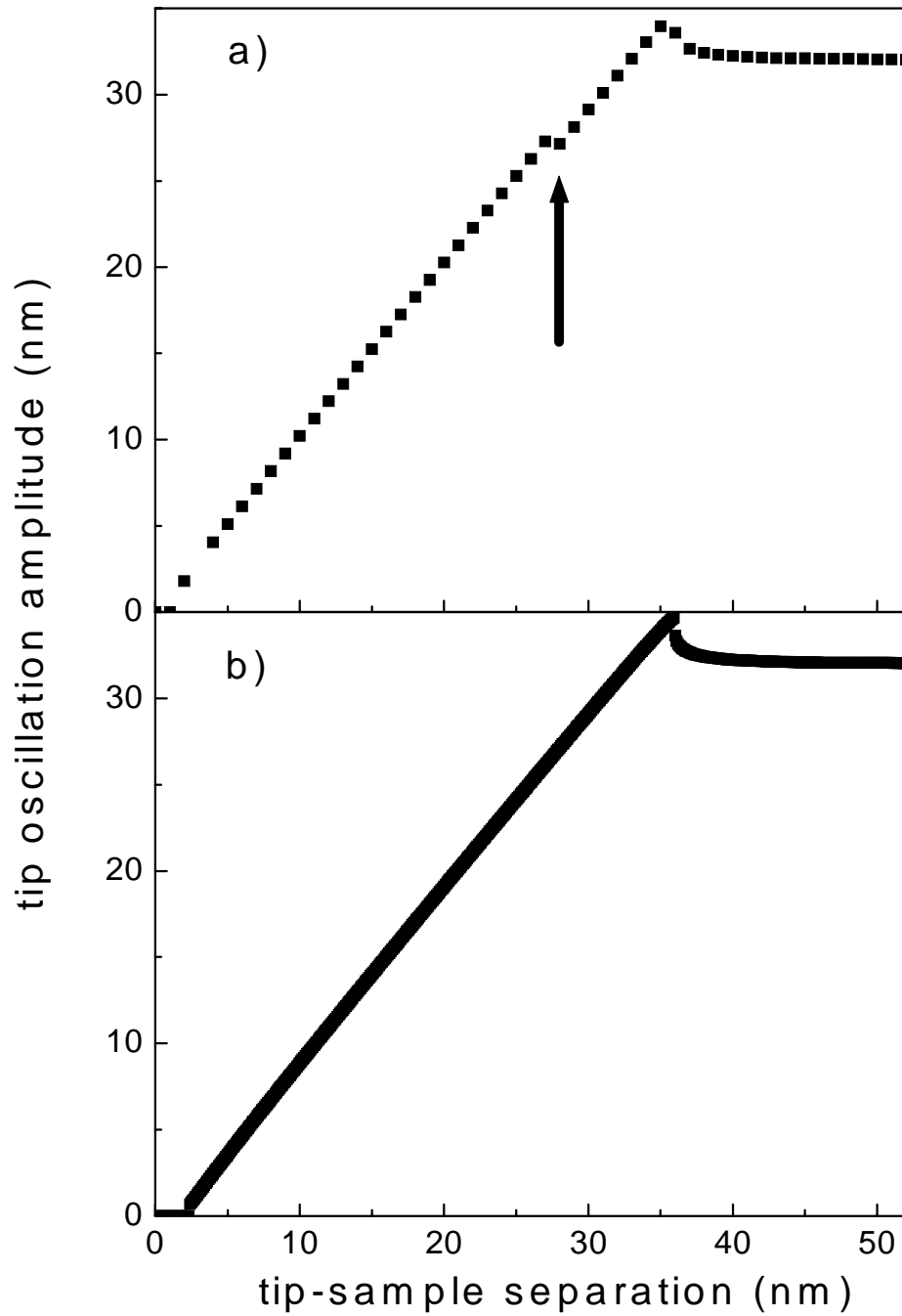
Figure 4.9: Amplitude-distance curves above a 28 nm particle. In a) the amplitude was calculated at 1 nm intervals while lowering the tip toward the surface and in b) the amplitude was calculated every 0.1 nm. Note the discontinuous jump in a).
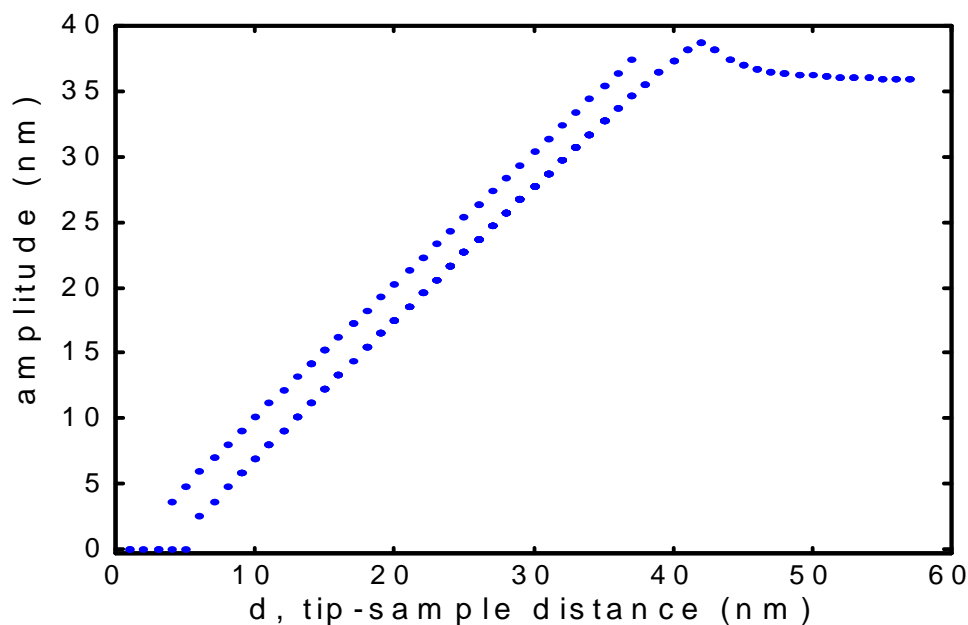
Figure 4.10: Amplitude-distance curve showing the two possible solutions at each tip-sample distance. These curves were generated by choosing different initial conditions.

and contact forces between a tip and nanoscale particle are smaller than those between a tip and plane, due to the large difference in the radius of curvature (R_2) of the imaged object (see Fig. 4.13). To correct for this phenomenon, we used a slightly larger particle in the model to arrive at the correct measured particle height (e.g., $R_2 = 14.99$ nm instead of 14.03 nm). Height anomalies have been observed experimentally in tapping mode and have been attributed to differences in adhesion (capillary forces) [111].

Figure 2.13 (a) on page 24 shows an experimental data series of a 28 nm particle that has been injected with charge with a Cr-coated Si AFM tip [59]—from the initial increase and following decrease in apparent height we conclude that charge is indeed being injected and is then dissipating. Figure 2.13 (b) are the calculated fits to the data in (a) (see Chapter 2), determined from the tapping mode model. From these fits we estimate that the initial amount of charge injected was on the order of 60 electrons.
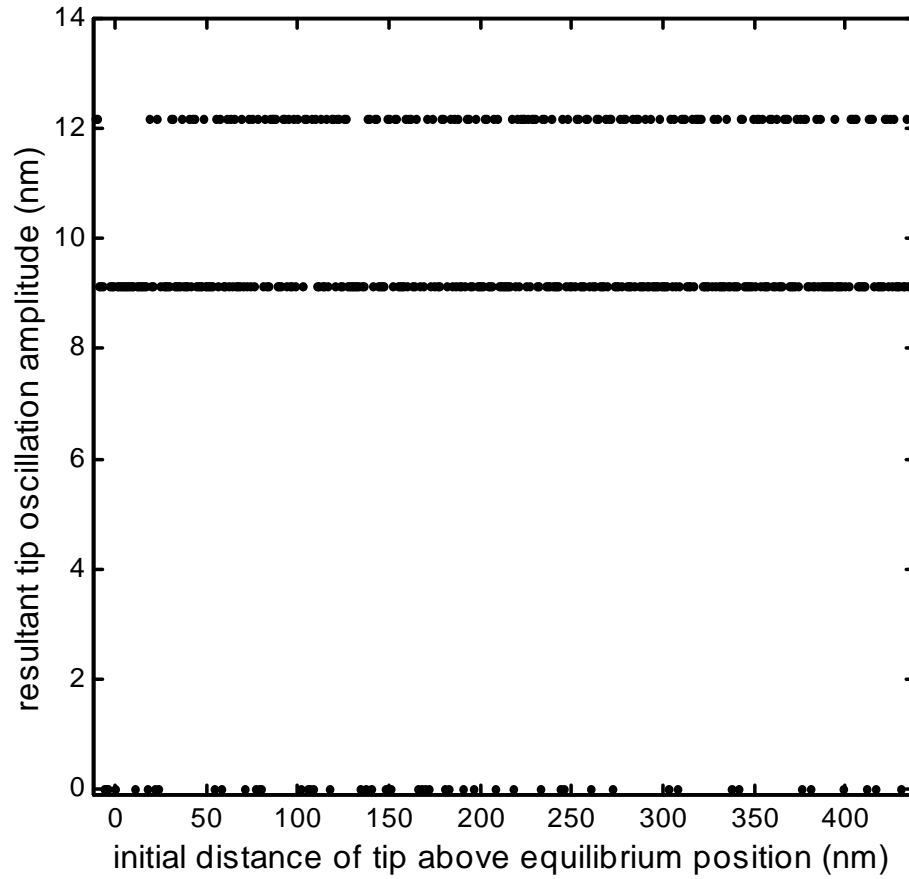
Figure 4.11: Tip oscillation amplitude as a function of initial displacement of tip about its equilibrium position (initial velocity=0). Note that in general both solutions are possible, except for a small range about the equilibrium value where the lower amplitude solution dominates. For some initial conditions, trapping by the sample (i.e., amplitude ∼0) was also found.
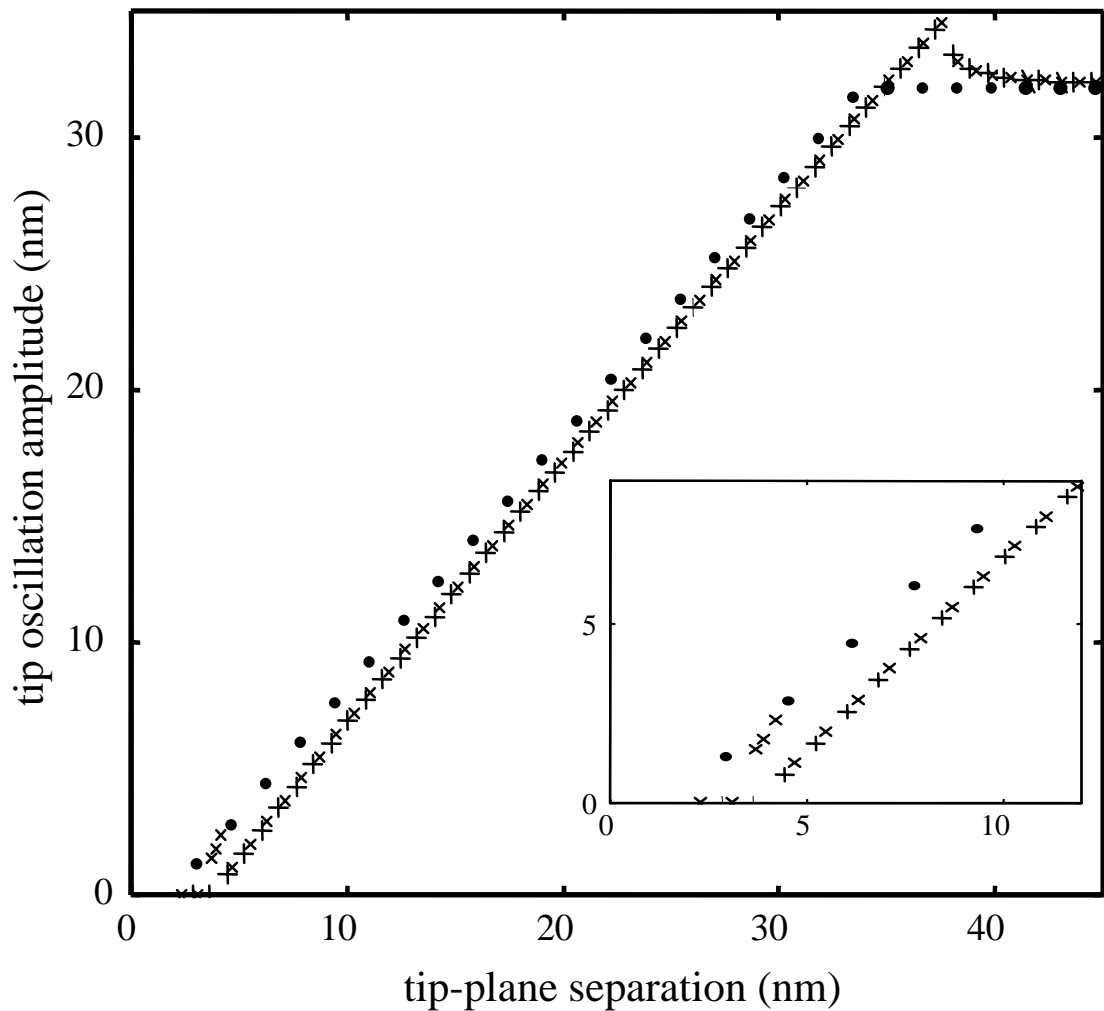
Figure 4.12: Amplitude-distance curves for repulsive-force-only case (•), attractive-force-only case (+) and for the case with both attractive and repulsive forces (x). Note that when there are both attractive and repulsive forces present there is a discontinuous jump from one solution to a second solution; the curve changes from almost identical to the attractive-force-only curve, to very similar to the repulsive-force-only curve. Inset: blow up of region including discontinuity.
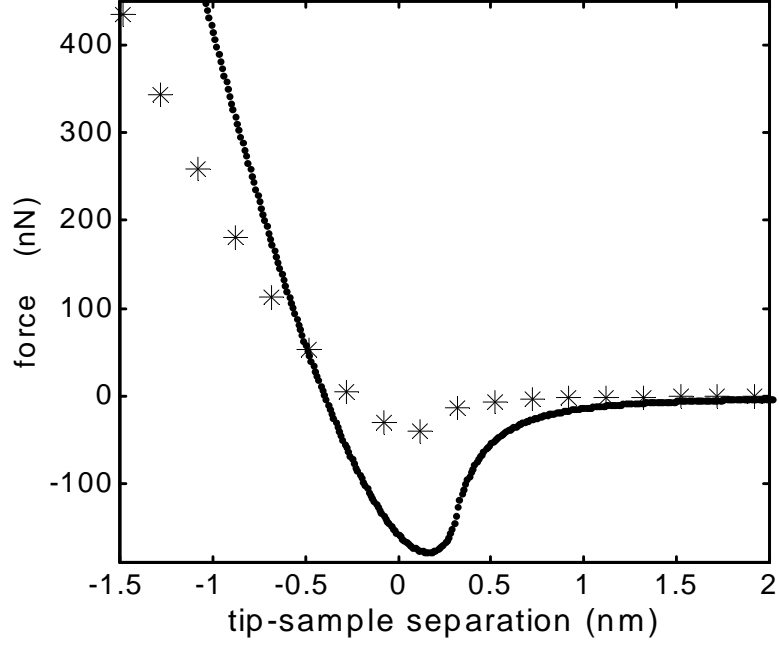
Figure 4.13: Force-distance curves above a particle ($*$) and above a plane ($\bullet$) with $R_1 = 50$ nm, $R_2 = 14.99$ nm, $W = 0.756$ mJ/m^2 (JKR). Note that in general the magnitude of the tip-plane force is larger than the tip-particle force.

4.5.3 DMT theory

Since the system is in the JKR-DMT transition regime, and since the adhesion energy W is a difficult parameter to measure and might well be lower than our estimate in Section 4.5.1, we have also briefly investigated tapping using the DMT theory. Here the important equations are:

$$
\begin{aligned}
a^3 &= \frac{3R}{4E^*}\left(F_{DMT} + 2\pi W R\right) \\
d &= \frac{a^2}{R}
\end{aligned}
\tag{4.9}
$$

We have considered adhesion energies of $W = 1$ mJ/m^2 and 10 mJ/m^2. Figure 4.6 shows a force-distance curve for the DMT theory together with one for the JKR case—the effect of a smaller W is clearly seen in the lack of a large attractive force at contact. For the smaller W (1 mJ/m^2) and the DMT theory, we found all particle heights were imaged correctly in the calculation. For the $W = 10$ mJ/m^2 case, a

contact theory	W	number of electrons imaged
JKR	756 mJ/m^2	56e, 49e, 44e
DMT	1 mJ/m^2	49e, 43e, 38e
DMT	10 mJ/m^2	50e, 43e, 38e
DMT/JKR	756 mJ/m^2	56e, 48e, 43e

Table 4.5: Comparison of results for number of charges injected for different contact forces

slightly larger particle height ($R_2 = 14.49$ nm) was again used to get the correct measured value. Finally, the situation $W = 756$ mJ/m^2, with a DMT interaction between the tip and particle, and a JKR interaction between the tip and plane was considered. In all cases, fits to the data in Fig. 2.13 (a) were made and the results are summarized in Table 4.5. The small spread in the results ($\sim 13\%$) shows that the exact form of the contact force is unimportant for quantitative charge imaging. Closer to the detection limit, the different force types yield a similar variation ($\sim 12\%$).

4.5.4   Charge sensitivity

Charge sensitivity was briefly investigated in tapping mode analogously to the non-contact mode case (Section 4.4.3). Figures 4.14 and 4.15 are the corresponding graphs to Fig. 4.3 and 4.4 respectively. Similar trends are seen in both cases. In order to achieve greatest charge sensitivity, the appropriate tip size for the charge distribution should be chosen, and the tip-sample distance or set-point should be optimized.

4.5.5   Lateral resolution

Besides charge sensitivity, we used the models to estimate lateral charge resolution. To do this we assumed a charge distribution consisting of two point charges (50 electrons each) arranged symmetrically on either side of the origin on the y-axis. We then successively reduced the distance between the two point charges and calculated an AFM scan in each case ($R_1 = 50$ nm). The results are found in Fig. 4.16. From this we estimate that such point charge distributions are resolvable if they are $\sim$ 40– 50 nm apart (50 nm tip radius). This suggests that individual charged nanocrystals
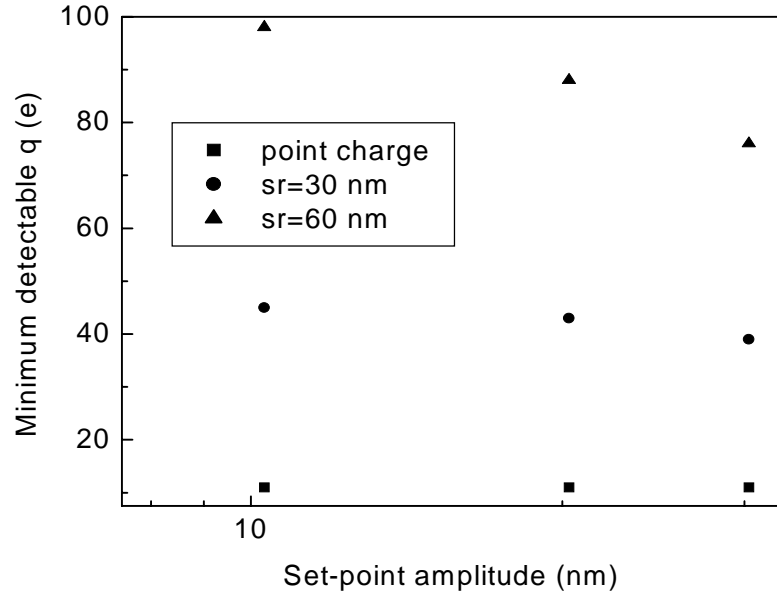
Figure 4.14: Minimum detectable charge as a function of set-point amplitude, or equivalently tip-sample spacing (tip radius $R_1 \sim 50$ nm, charged region radii sr=0, 30 and 60 nm). Analogously to the non-contact case, sensitivity increases as tip-sample spacing increases.
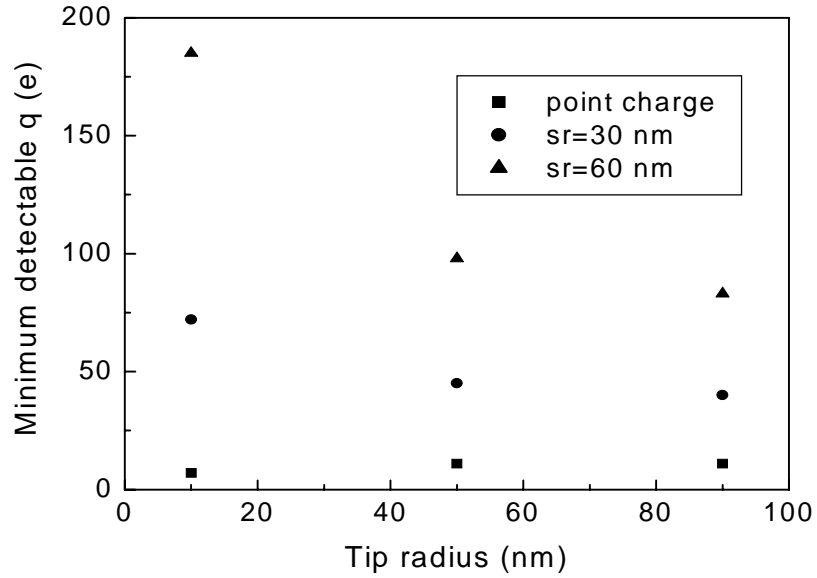
Figure 4.15: Minimum detectable charge as a function of tip radius. Analogous to the non-contact case, the best sensitivity occurs when the tip and charge distribution are of the same order.
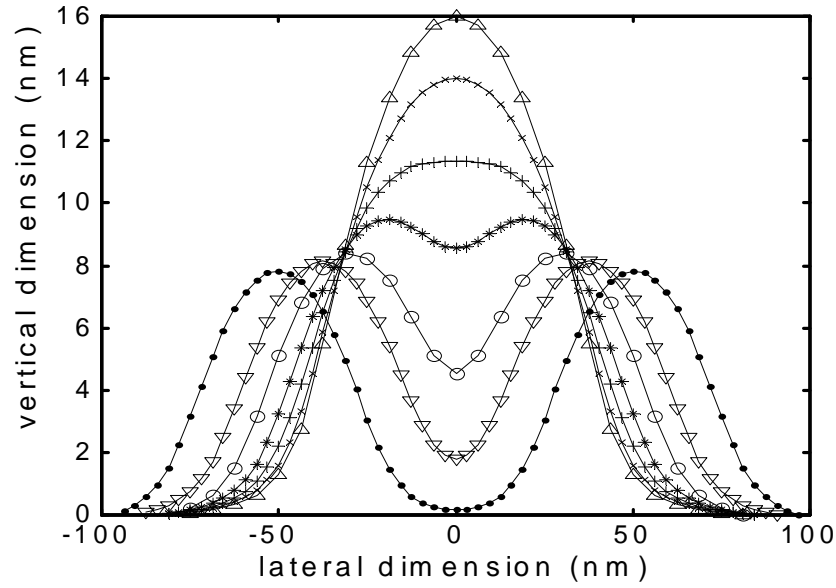
Figure 4.16: Calculated AFM scans of two point charges, separated by various lateral distances. Each point charge consists of 50 electrons. In the scans shown, they are 15 ($\triangle$), 25 (x), 35 (+), 45 (∗), 60 (o), 75 (O) and 100 (•) nm apart.

in our ion implanted samples (such as those in Fig. 3.7) are not resolvable since they are estimated to be ∼ 20 nm apart.

4.6 Model refinements

Many small improvements to the basic models in this chapter might be made. In particular, the models could be expanded to include three-dimensional charge distributions, and include the effects of dielectric layers, and image charges in the substrate. As well, the effects of damping could be considered (more important for liquids) [52, 112] as well as capillary forces. The models could be made more versatile and include more topographic situations than just a planar sample or a single particle. In the above, the forces on the tip from the particle and plane are added. This is a good approximation when the tip is directly above the particle, but perhaps is insufficient at the particle's edge. The effect of this assumption should be more carefully evaluated and refinements made if necessary. Also, charge on the sample

is assumed static and does not move as the grounded tip scans over it. In reality, the charge may be free to move on the surface of the particle if it is trapped in the conduction band, and this approximation may be what results in an underestimate of the charged particle's width (see Fig. 2.13). This too should be further explored. As well, the charge interaction should be calculated at each point in the oscillation, not just at the mean position z_{L0}. The forces on the large-area cantilever (relative to the tip) might also be included, though they would have only a small effect. The effect of a constant force on the results was tested by adding a constant value to all numbers in the force table and calculating an amplitude-distance curve. The resulting curve was virtually identical to such a curve calculated using an unaltered force table (see Fig. 4.9 (b) for example) but was shifted horizontally along the tip-sample separation axis. This shift may be interpreted as follows: if a constant attractive force is added to the interaction, the cantilever bends toward the sample and tapping occurs at a larger cantilever-sample spacing (but same tip-sample spacing). For this reason forces on the cantilever (as opposed to the tip) have been ignored as they are approximately constant and only result in a shift of the amplitude-distance curve.

4.7 Summary

We have presented two models for quantitative AFM charge imaging—one valid in non-contact mode, the other in tapping mode. Comparisons among different theories for the contact force show that the exact form of this force is unimportant for quantitative charge imaging. We have applied these models to two experimental situations, have found good fits to the data and have made quantitative estimates of the imaged charge. Estimates of the sensitivity of AFM charge imaging suggest that the charge resolution is a few electrons for standard AFM cantilevers and imaging parameters. From the models we have determined that the charge sensitivity may be improved by increasing tip-sample height and choosing an appropriate tip radius for the charge distribution imaged.

Chapter 5   Optical properties of Si nanocrystals

5.1   Introduction

There has been a flurry of activity in the study of the optical properties of silicon nanostructures since Canham's seminal paper in 1990 [3]. (Canham's paper has been cited more than 2500 times). This enthusiastic quest to determine the origin of photoluminescence (PL) in nanosized silicon has come to pass at a time of rapid development in the area of optical communications. Thus the understanding and control of Si nanocrystal optoelectronic properties have become an even more enticing objective.

The goal of our work in this area is to determine if luminescence from Si nanocrystals is due to quantum confinement effects or to defect states, and to prepare well-passivated nanocrystals suitable for optoelectronic applications. Possible luminescence mechanisms are shown in Fig. 5.1 [113].   If quantum confinement is the reason for the luminescence signal, then: 1) luminescence should be (almost) independent of what material passivates the dangling bonds at the nanocrystals' surface and 2), the PL wavelength should shift towards the smaller wavelengths (higher energies) with decreasing particle size (see Section 1.2). To demonstrate the latter, control of particle size is needed—as discussed in Section 2.2, we have the capability to make nanocrystal samples with narrow size distributions. The challenge of this chapter is the production of samples with fully-passivated surfaces (i.e., no defects) using different passivating materials, in order to study nanocrystal photoluminescence.
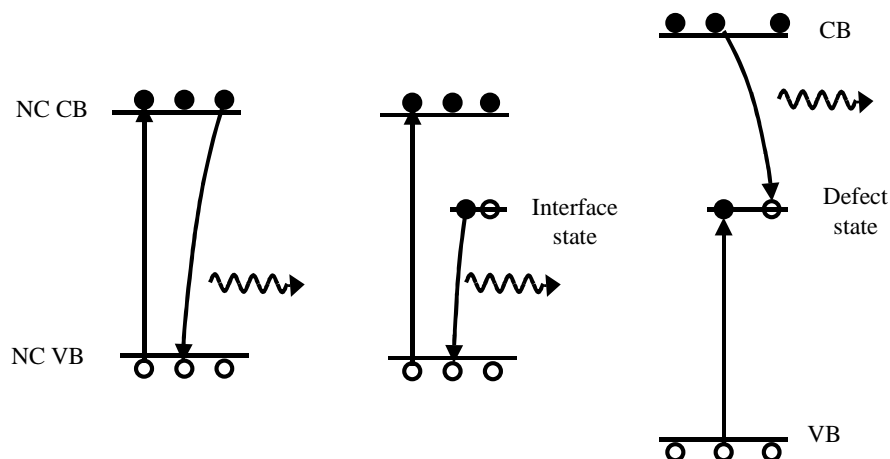
Figure 5.1: Possible mechanisms of visible PL. Straight arrows represent excitations and curved arrows represent recombinations. Left: band-to-band transitions and recombinations in nanocrystals (NC), between holes in the valence band (VB) and electrons in the conduction band (CB). Center: recombination involving a trapped hole or electron at an interface state. Right: recombination involving electrons or holes in the passivation material's conduction band or valence band, and trapped carriers in a defect state in the passivating material.

5.2   Passivation of Si nanocrystals

A silicon atom in the interior of a piece of silicon forms covalent bonds with four other silicon atoms. An atom on the surface, however, will have one or more valence electrons not bonded to Si atoms. If these valence electrons do not take part in a covalent bond with another material (e.g., hydrogen or oxygen), these "dangling bonds" will give rise to localized defect states, providing sites for nonradiative recombination of an exciton (electron-hole pair), thus destroying the photoluminescent efficiency of the material. When such states exist, the material is said to be "unpassivated." These defect states might also be a source of luminescence along with bulk defects in the passivating material (see Fig. 5.1). Thus it is important to find a material that well passivates the nanocrystals and has a low bulk defect state density. The passivating materials considered here are SiO_2 and hydrogen, and the techniques used to evaluate the passivation are X-ray photoelectron spectroscopy (XPS) and photoluminescence (PL). Silicon nitride was considered as a passivating material but was rejected due

to its high defect density and optically active defects [114, 115]. Fourier transform infrared spectroscopy (FTIR) was attempted to learn more about the nanoparticle surface, but the signal was too small for the typical nanoparticle areal densities of our samples.

5.3   Hydrogen passivation– PL and XPS

Passivation with hydrogen has several advantages. A hydrogen passivation layer is only one atom thick and is of high quality—no "bulk" defects exist. In principle, applying hydrogen termination to a nanocrystal will not change the particle size and such a termination is stable enough to transfer samples from one chamber to another.

Two types of samples were used for the hydrogen passivation experiments: 1) unclassified Si nanocrystals produced by laser ablation and collected by electrostatic precipitation on a Ge substrate [26] and 2) a 1.5–2 nm Si layer on a Ge substrate grown by molecular beam epitaxy [116].

The first H-passivation experiments were on the unclassified laser ablation samples. The samples, after several days air exposure, were dipped in hydrofluoric acid (48% HF, balance distilled water) for 10 s. In this way, the HF etched the native oxide on the particles and left the samples hydrogen terminated. Photoluminescence measurements were made using a thermoelectrically cooled 256x1024 CCD detector and a grating spectrometer. An Ar^+ laser ($\lambda = 457.9$ nm) at a power of 5–15 mW and spot size ~ 0.5 cm^2 was used to excite electron-hole pairs in the sample (see Fig. 5.1). The light emitted by the electron-hole pairs upon recombination was recorded by the CCD detector, that was cooled to –56ºC. Exposure times of 100 ms or 1 s were used and a filter blocked the laser line. A background scan was taken and the grating and detection efficiencies were taken into account.

Figure 5.2 shows the PL signal measured before the HF dip, then immediately afterwards, then after 7, 17 and 22 minutes of laser exposure. The PL signal was much less intense immediately after the HF, due in part to nanocrystal removal from the surface—material was seen to fall off of this very high coverage sample during
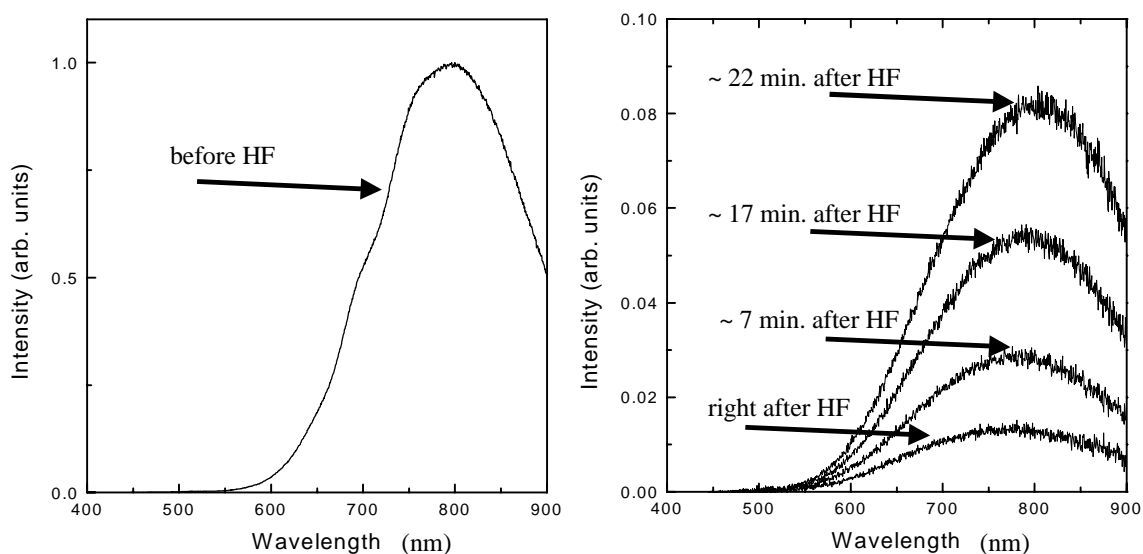
Figure 5.2: PL as a function of wavelength of an unclassified Si nanocrystal sample (right) before and (left) after a 10 s HF dip. While the PL intensity is in arbitrary units, the decrease in the PL signal after HF dipping is apparent due to the decrease in the signal-to-noise ratio. Note the increase in PL intensity with laser exposure.

the dip. The longer the sample was exposed to laser light, the more intense the PL signal became. Thus the PL signal was thought to be from defects in the native oxide and the effect of increasing intensity with laser exposure was attributed to "photo-oxidation" [117], i.e., an increase in the oxidation rate under laser excitation. This demonstrates the main disadvantages of hydrogen passivation—an H-passivated Si surface is stable only a limited time in air, and quite unstable in air under laser irradiation.

The next hydrogen passivation experiments were done in a small Si nanocrystal deposition chamber which could be purged with N_2 or evacuated to high vacuum (10^{-6}–10^{-7} torr) [26]. This system also included an insitu PL measurement setup, and was connected to a surface analysis system (XPS, Auger spectroscopy). A Kaufman ion beam source was also available. Thus a sample could be made, size-classified and deposited, loaded into the surface analysis system for XPS measurements, brought back for irradiation with the ion source, reloaded for XPS analysis, then again moved
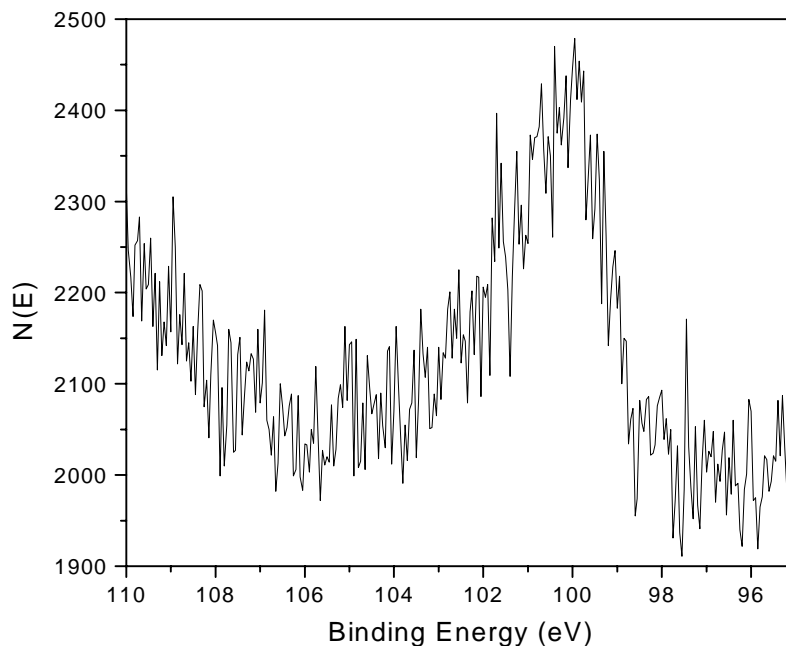
Figure 5.3: XPS Si 2p peak of an Si nanocrystal sample size classified at 10 nm. Note: 2p refers to the orbital from which the electrons originated, and N(E) is the number of electrons detected at a particular energy.

to the deposition/implantation/PL chamber for insitu PL measurements—all without air exposure.

Figure 5.3 shows the XPS signal for an Si nanocrystal sample, size-classified at 10 nm and deposited on a Ge substrate (see Section 2.2). This sample was made in this purged system and immediately transferred into the surface analysis chamber (base pressure 10^{-9} torr). In X-ray photoelectron spectroscopy [118–120], X-rays (from a 15 keV electron beam impinging on an Al electrode) knock out core electrons from the sample. A cylindrical mirror analyzer measures the kinetic energy of the ejected electrons, and since the X-ray energy is known, the binding energy of the ejected core electron may be determined. From this measurement, not only can the elemental composition of the sample be determined, but also the chemical state— i.e., the binding energy of a 2p core electron from a silicon atom bonded to four other Si atoms is about 99–100 eV, while the binding energy of a 2p core electron
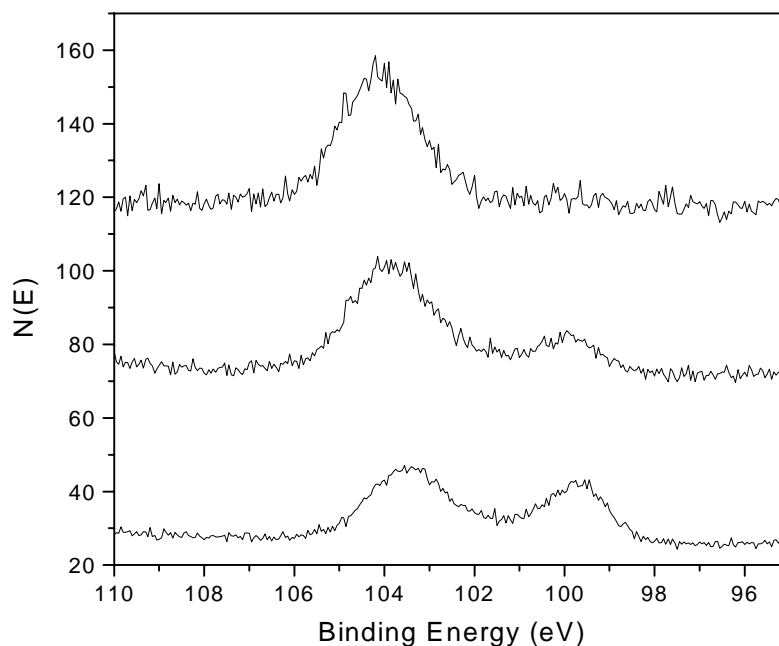
Figure 5.4: XPS Si 2p signal before exposure (bottom), after 50 s D$^+$ exposure (centre) and after 11.5 minutes D$^+$ exposure (top), offset for clarity. Note the increase in oxidation with deuterium exposure.

from a silicon atom bonded to four oxygen atoms is approximately 103–104 eV. A peak seen between 100 and 103 eV is interpreted as the signal from a sub-oxide, i.e., from Si atoms bonded to 1, 2, or 3 oxygen atoms, with the remaining bonded to Si. Examining the Si 2p peak in Fig. 5.3, most of the signal is at $\sim$ 100 eV, demonstrating the presence of silicon. The small shoulder to the high binding energy side of the peak, however, denotes the presence of a thin layer of SiO$_x$. This is not a surprising result, despite having made the sample in a purged atmosphere and transferring it immediately to UHV, since an unpassivated Si surface is extremely reactive.

An attempt to produce a hydrogen passivation layer was made using the Kaufman source. The sample used was the 1.5–2 nm layer of Si grown on Ge. Deuterium was implanted at the low energy of 100 eV for 50 s to a fluence estimated to be $\sim$ 2x10^{15}/cm^2. (A 2 μA current was measured by a Faraday cup with a 0.26 cm^2 opening). The sample was transferred immediately afterwards into the UHV cham-

Synthesis method	Further processing
direct growth/LP-CVD	–
CVD	annealed 30 minutes, 1000°C
CVD	unannealed
aerosol synthesis (3–4 nm Si core)	1.5 nm oxide shell grown by passing aerosol through an oxidation furnace.

Table 5.1: Nanocrystal samples

ber. XPS analysis (Fig. 5.4) of the Si 2p signal shows an *increase* in the oxidation after deuterium exposure. After a total exposure of 11.5 minutes, the sample was completely oxidized (Fig. 5.4). Thus our conclusion is that the vacuum of our deposition chamber is not sufficient for these studies, and that a possible water layer on the sample led to deuterium-induced decomposition of H_2O, producing oxidation [121]. These results, the difficulty of producing an oxygen-free system, and the high quality and technical relevance of SiO_2, indicate that silicon dioxide is the preferred passivation material for silicon nanocrystals.

5.4   Silicon dioxide passivation– PL studies

The advantages of SiO_2 as a passivating material are mentioned above. Some of the disadvantages include the possible loss of size classification upon oxidation, and the difficulty of controlling and measuring the degree of oxidation of nanoparticles. To investigate the passivation of nanocrystals with SiO_2 (and to qualitatively probe the samples for defects), we studied several different types of nanocrystal samples. They were made in the nonvolatile memory geometry: a 5 nm tunnel oxide was thermally grown on highly B doped ($\sim 10^{19}$ cm^{-3}) Si substrates, on top of which were deposited nanocrystals made by "direct-growth" (also called LP-CVD or low pressure chemical vapor deposition), CVD deposition of a silicon-rich oxide, or aerosol synthesis [27]. Details of the samples may be found in Table 5.1. Following nanoparticle synthesis, a 12 nm high temperature oxide was deposited on the samples [18]. A control sample consisted of a 5 nm thermal oxide on Si (no nanoparticles, no top oxide).

Detector	Filter	Laser	Spot size	Grating resolution
GaAs	50% at 550 nm	488 nm, $\sim$4-5 mW	$\sim$1 mm^2	$\sim$3 nm
GaAs	50% at 495 nm	458 nm, $\sim$4-5, 10, 17 mW	$\sim$1 mm^2	$\sim$3 nm
AgOCs	50% at 550 nm	458 nm, $\sim$22 mW	$\sim$4–10 mm^2	$\sim$6 nm

Table 5.2: PL experimental configurations

The photoluminescence measurements were done using GaAs (sensitive to 300–900 nm wavelengths) and AgOCs (sensitive to 400–1100 nm) photomultiplier tube detectors and an Ar$^+$ laser. Details of the experimental configurations may be found in Table 5.2. Time-resolved measurements used a multichannel photon counting system.

Three types of PL measurements were made: PL intensity as a function of wavelength, PL lifetime measurement at a particular temperature and wavelength, and PL intensity of a certain wavelength as a function of temperature. Measurements were made following a 10 minute 1100°C vacuum anneal. Further measurements followed a forming gas anneal that used the following recipe: 10% H$_2$, 90% N$_2$, 120 s at room temperature, 600 s at 800°C, 120 s at room temperature, gas flow 5 l/min. The purpose of the first step was to anneal out any defects in the oxide. The reason for the forming gas anneal was to passivate any remaining defects with hydrogen.

Figure 5.5 shows the photoluminescence intensity as a function of wavelength for the samples after the 1100°C anneal. The control sample displays no luminescence and the most intense signal is from the CVD samples. In Fig. 5.6, a PL lifetime trace taken on an annealed CVD sample at a wavelength of 600 nm shows a lifetime of less than a microsecond. This very short lifetime is characteristic of defects—longer lifetimes, on the order of tens of μs, are expected when indirect transitions are involved, i.e., in the case of Si nanocrystals [6]. Thus we attributed this luminescence to defects and proceeded with the forming gas anneal.

After the forming gas anneal, all the photoluminescence that had been previously detected was quenched, confirming defects as the source. A new luminescent signal arose, however, in the CVD samples, peaked at about 920 nm (Fig. 5.7). Figure 5.8 is the corresponding lifetime trace taken at 100 K (at a wavelength of 920 nm).
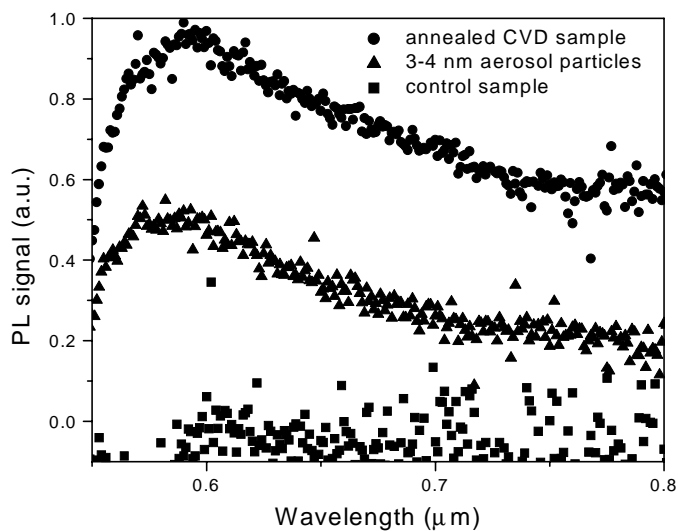
Figure 5.5: PL intensity as a function of wavelength after a 10 minute 1100^oC vacuum anneal. The control sample shows no luminescence. The direct growth sample PL signal (not shown) is very similar to that of the aerosol sample. The annealed CVD Si-rich oxide sample has the strongest luminescence signal.
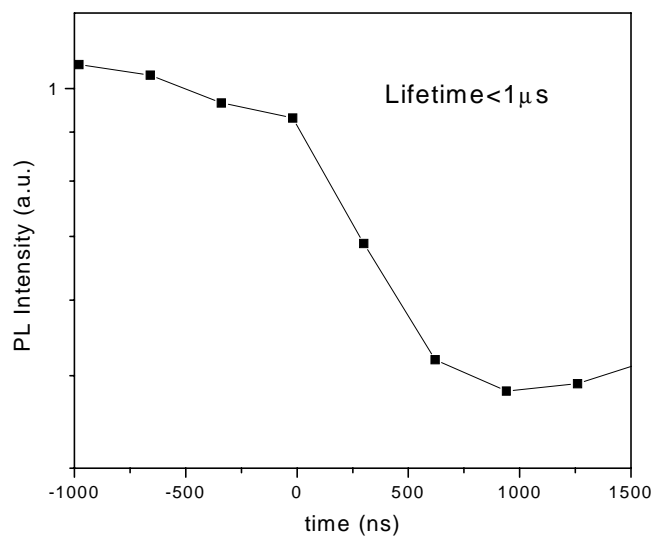
Figure 5.6: Time resolved PL of annealed CVD sample, at $\lambda = 600$ nm. Note the very short lifetime, characteristic of defects.
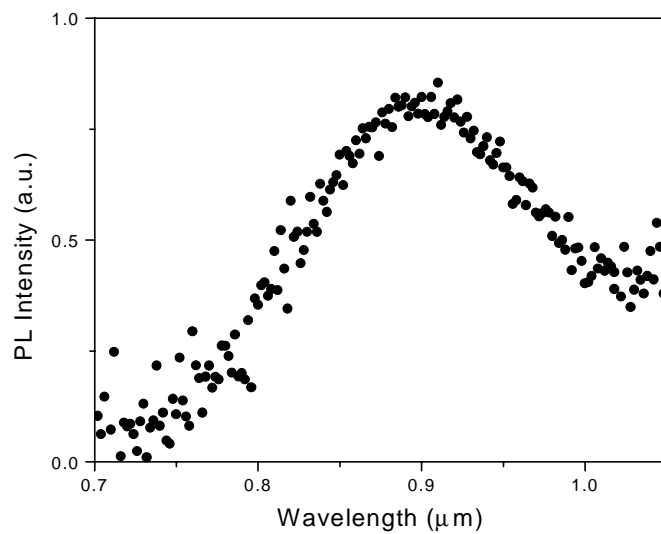
Figure 5.7: PL intensity as a function of wavelength after the forming gas anneal of the CVD Si-rich oxide sample (initially unannealed).
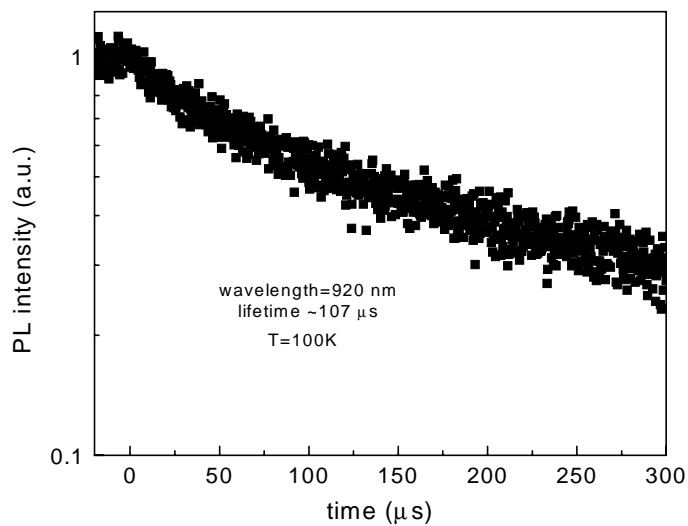
Figure 5.8: Time resolved PL of forming gas annealed CVD sample, at $\lambda = 920$ nm. The lifetime is on the order of 100 μs, a typical value for nanocrystals.
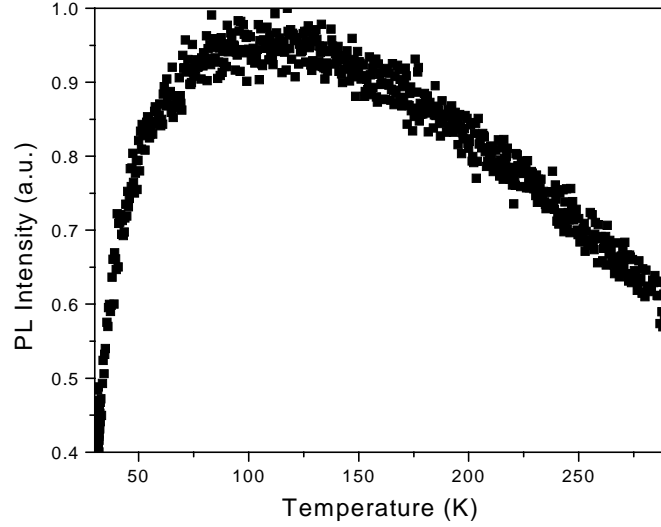
Figure 5.9: PL intensity at $\lambda = 920$ nm as a function of temperature. The initial rise and fall of intensity with increasing temperature is due to the fact that the radiative and nonradiative rates have different temperature dependences.

The resulting lifetime is ~ 100 μs, a typical value for a nanocrystal sample. Figure 5.9 shows the intensity at $\lambda = 920$ nm as a function of temperature. An initial increase and subsequent decrease in the integrated PL signal with temperature has been seen by others and is explained by modeling the system with a two-level (singlet and triplet) excited state, split due to the exchange interaction between the confined electron and hole [122]. Finally a PL signal seen near 1.1 μm (bulk Si bandedge) was attributed to the high doping of the substrate [123].

These results indicate that silicon dioxide, when combined with hydrogen, well passivates silicon nanoparticles. The fact that no nanocrystal luminescence was seen in the direct growth and aerosol samples may be due to complete oxidation of the particles, to the formation of a continuous nanoparticle film (thus preventing any quantum confinement) or to the presence of defects.

5.5   Summary

Indisputable evidence of the origin of visible luminescence is still elusive though much progress has been made. In this quest, passivation is of utmost importance as a poor passivation layer can lead to the luminescence quenching, or defect signals. Silicon dioxide, in combination with hydrogen, is a satisfactory passivation material.

Chapter 6   Conclusions and future prospects

6.1   Introduction

It has been said "an author never finishes a book, he merely abandons it" [124]—it may be equally said that "a scientist never ends an experiment, she simply moves on to the next one." In this chapter, improved and complementary experiments involving silicon nanocrystals will be discussed, as well as future innovative ideas. In conclusion, the results of this thesis will be summarized.

6.2   Unfinished business

AC-EFM and DC-EFM

The term electrostatic force microscopy (EFM) most often refers to AC-EFM [40], i.e., EFM involving an ac voltage. In this type of electrostatic imaging, a voltage, $V = V_{dc} + V_{ac}\sin(\omega_e t)$ [125], is applied between the tip and an electrode on the backside of the sample (ω_e is much higher than the feedback-loop frequency response, but much lower than the tip oscillation driving frequency, ω [40]). The interaction between the charge on the surface (Q_s) and the charge on the tip (Q_t), due to both the applied voltage and the induced image charge, is approximated as a point charge interaction (i.e., $F_{ts} \approx \frac{Q_s Q_t}{4\pi\varepsilon_0 z^2}$). To find the interaction between Q_e (the charge on the back electrode, $Q_e = CV$) and Q_t ($Q_t = -(Q_s + Q_e)$) the tip–back electrode system is approximated as a parallel plate capacitor. Thus $F_{te} \approx \frac{1}{2}\frac{\partial C}{\partial z}V^2$ (from the derivative

with respect to z of the energy of a capacitor). The total force is:

$$F \approx \frac{Q_s Q_t}{4\pi\varepsilon_o z^2} + \frac{1}{2}\frac{\partial C}{\partial z}V^2 \tag{6.1}$$

and the force gradient components, oscillating at ω_e and $2\omega_e$, respectively, are

$$\frac{\partial F}{\partial z}(\omega_e) \approx (\frac{\partial^2 C}{\partial z^2}V_{dc}V_{ac} - \frac{Q_s V_{ac}}{4\pi\varepsilon_o z^2}\frac{\partial C}{\partial z} + \frac{Q_s C V_{ac}}{2\pi\varepsilon_o z^3})\sin(\omega_e t) \tag{6.2}$$

$$\frac{\partial F}{\partial z}(2\omega_e) \approx -\frac{1}{4}\frac{\partial^2 C}{\partial z^2}V_{ac}^2\cos(2\omega_e t) \tag{6.3}$$

Thus by detecting changes in the tip oscillation amplitude at ω_e and $2\omega_e$ using a lock-in amplifier, and relating them to the force gradient (see Section 4.4), the charge on the sample may be estimated. The weaknesses of this technique include the assumptions of point charge distributions and treating the tip-sample geometry as a parallel plate capacitor, as well as the necessity of knowing $C(z)$, capacitance, and z, the tip height above the sample. From the $2\omega_e$ signal, $\frac{\partial^2 C}{\partial z^2}$ may be estimated, and must be integrated to find $\frac{\partial C}{\partial z}$ and $C(z)$ [126]. The precise height of the tip above the sample is always difficult to calibrate, though techniques exist [45]. Finally, as discussed in Section 4.4, the oscillation amplitude must be small compared to the tip-sample spacing for the relationships between amplitude and force gradient to hold. The advantage of this technique is that it has been shown to have 1 e [38] and even 0.1 e [126] sensitivity.

DC-EFM, as its name suggests, involves applying a dc voltage to the AFM tip. In this case, the tip-sample system is most often modeled as a parallel plate capacitor [34], and the change in force gradient detected as a change in phase of the oscillation [42]. The disadvantages of this technique are similar to the AC-EFM case.

A careful comparison of the charge imaging technique presented in this thesis with more traditional EFM methods would quantitatively pinpoint the strengths and weaknesses of each technique, leading to the new directions for improved imaging. In particular, perhaps the most accurate *and* most sensitive method would be to use DC- or AC-EFM in combination with the type of detailed modeling discussed in

Chapter 4.

Calibration

Calibration in electrostatic imaging is very important yet very difficult. An ideal calibration sample—with a known charge distribution—is hard to come by. One method of calibration is to take a structure of known capacitance (e.g., a sphere), apply a voltage to it, image it, then estimate the charge from the expression, $Q = CV$. However, the precise capacitance, considering the surroundings, is difficult to determine. Another solution is the following: take two pieces of a flat, conducting sample and join the pieces with a very thin insulating layer, determine $C(z)$ as best as possible (either experimentally, or via calculations), then apply a known potential to one half of the sample. Then use the difference in height between the two halves and C, and V, to determine Q. Alternatively, just a single flat surface might be used, and instead of the height signal, the piezo extension before and after the voltage is applied may be recorded and related to changes in height. Other possible methods include looking at calculated and measured force-distance curves, with and without applied voltages.

A possible but exotic calibration method involves a gated "quantum dot" or nanocrystal, small enough so that Coulomb blockade effects are apparent [127] (i.e., $kT < \frac{e^2}{2C}$, see Section 1.3). Thus as the gate voltage is changed, the effect of adding one electron at a time is detected and used for calibration. A single good calibration, or a combination of several of the methods mentioned above would validate electrostatic imaging, and allow it to be called truly quantitative.

6.3 Complementary experiments

Charging of nonvolatile memory samples

An interesting experiment would be to use the techniques described in this thesis to inject charge into nanocrystal samples made in the nonvolatile memory geometry (see

Section 5.4). Because of the thin tunnel oxide between the substrate and nanocrystal layer (Fig. 1.5), the charge may now be injected from the substrate by grounding the tip and biasing the substrate. Such an arrangement means that tip damage (such as that seen in Fig. 3.12) may be avoided. The 12 nm top oxide may be gently etched to rid the sample of surface states. AFM charging experiments would complement the more traditional capacitance-voltage measurements that have been done on these samples [18].

Where is the charge stored? Interface states or nanocrystals?

While the experiments in Chapter 3 demonstrated that nanocrystals are necessary for charging, they did not resolve if the charge was trapped in an interface state or in the nanocrystal conduction band. A different technique is necessary to answer this question. Since the interface states are expected to be of different energies than the nanocrystal conduction band (Fig. 3.4), thermal- or photo-excitation might be used to eject the charge from charge traps (which may be then detected via current sensing techniques or by AFM). Thus by identifying the energy of the trap sites, the type of trap may be determined. Alternatively, hydrogen or deuterium may be used to passivate any interface states [43], thus eliminating this type of charge trapping site. Both the above experiments must be executed carefully in order to avoid further ambiguity—in the first case, the cross-sections for various photoexcited processes must be taken into account, while in the second, the effect of mobile ions in the film must be considered. A third type of experiment is to prepare samples containing different mean nanocrystal sizes (and hence samples with nanocrystals of different bandgap energies due to the quantum size effect). A voltage threshold dependence (minimum voltage necessary for charging to occur) on nanoparticle size would indicate that the nanocrystal is the site of charge storage.

Transport in SiO_2 films containing Si nanocrystals

The question of charge transport mechanisms in our SiO_2 samples containing Si nanocrystals is left unanswered. Charging experiments on samples with different
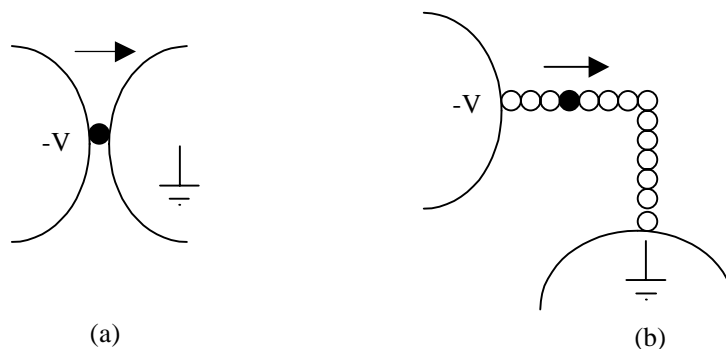
Figure 6.1: Transport measurements on (a) a Si nanocrystal between two electrodes and (b) a Si nanocrystal "nanowire" formed by AFM particle manipulation.

particle densities and sizes and different oxides thicknesses would shed light on this question. Experiments, such as particle density dependent or temperature dependent conduction measurements [128,129], could demonstrate the existence of hopping conduction in our films. As well, modeling of the transport, and fitting the observed experimental decay rate, would elucidate the transport mechanisms in these films and complement our charging experiments.

6.4 New directions

Our world is getting smaller—both literally and figuratively—and nanotechnology is leading the way. Due to the privileged role of silicon, Si nanocrystals are at the forefront.

Our capabilities in size control of Si nanoparticles open up many device possibilities. In particular, besides nanocrystal nonvolatile floating gate memories and quantum cellular automata, size-classified Si nanocrystals might be used to form 3-D photonic crystals.

The ability to manipulate the location of nanoparticles allows us to make interesting structures for novel experiments. For example, a nanoparticle might be pushed with the AFM between two electrodes for transport experiments (Fig. 6.1 (a)) [130].

The ability to locally inject charge gives rise to new tools and interesting experiments—for example charge injected in an Si "nanowire" (formed by AFM manipulation) may be observed and investigated (Fig. 6.1 (b)).

Electrostatic modeling allows the interpretation of AFM images of charge in these new experiments and suggests ways of increasing an AFM's sensitivity to charge.

Finally, optical analysis such as photoluminescence experiments on well passivated samples allows the probing of physical phenomena. For example, the suggestion that "blinking" of photoexcited Si nanocrystals is due to ionization [131] may be tested by simultaneously applying a field with an AFM tip and making PL measurements with an NSOM (near-field scanning optical microscope).

In this work we have developed the techniques highlighted above and have used them to investigate the optical and electronic properties of silicon nanocrystals. In particular, we have used an AFM to inject charge into single Si nanoparticles (made by aerosol synthesis and size selected) and have observed the charge dissipation. SiO_2 films containing Si nanocrystals have also been locally charged, and through a series of experiments it has been demonstrated that nanocrystals are necessary for charge trapping. Electrostatic models (for both non-contact and tapping modes) have been developed for quantitative estimates of the charge injected and to investigate the discharging dynamics. Passivation studies and PL experiments have shed "light" on nanocrystal optical and passivation properties. The results and techniques developed in this thesis lead to new, interesting investigations of the nanoscale.

Appendix A Matlab code for electrostatic models

A.1 Non-contact mode

This section contains the Matlab code for non-contact mode imaging. It has been used on Windows, Macintosh and Linux platforms (Matlab 5.0-5.3). It solves equation 4.3 using Newton's method.

PROGRAMS

- prefith—must be run first, defines parameters, sets up charge distribution

- newtjh—solves for z (height of tip above sample)

The above two files are the ones you need to run. Below are files called by them.

imqjf—finds value and location of image charges
ftbjh—calculates the total force gradient and derivative of force gradient
tbjf—calculates individual force gradients and derivatives

Notes on notation:

- f and df are used to refer to the functions f=(force gradient–K) and df=derivative of (force gradient–K), K is the set-point force gradient.

- In Matlab, % precedes a comment. Comments in the following will be *italicized* for clarity.

prefit.m:

In the first section, various parameters are assigned values. These must be entered by the user (using the appropriate units noted in the code) and the file saved before running. They depend on:

- the number of points in the scan that is to be fit (tlength)

- the number of pixels in a scan and the lateral length of the scan (int)

- the initially assumed amount of charge (q) and the radius of the area over which it is spread (sr), and grid spacing for the charge grid (ints)

- the standard deviation of the charge distribution (s), if a Gaussian distribution is to be used

- the AFM tip radius of curvature (R1)

- appropriate material parameters for the tip and sample materials being used—in our case, Si and SiO$_2$ (nsi, nsio2, sigma, epsilon)

The output generated is the charge grid qs at (xs, ys) and the half charge grid qsh at (xsh, ysh). Note that the calculation is currently set up for symmetric charge distributions.

****

global R1 X Y xs ys xsh ysh qsh ints A B K range int e0 qs sr s
%Run this to assign values to variables and define charge distribution
%Sets up parameters for Newton's method, except for initial values.
%Solves for z (height of tip above sample in nm) for constant force gradient equal to K.
%Tip is conducting sphere, charge on sample is disc with uniform density or Gaussian profile.
%Factors of 10^27 and 10^-36 in kq and kvdw give force gradient in N/m with distances in nm
%Note: range/int must be an integer, sr/ints must be an integer

tlength=128; *%number of points in the curve you are fitting*

int=750/256; %*length of AFM scan in nm divided by number of pixels*
range=tlength*int; %*length in nm of curve you are fitting*
sr=160; %*charged area radius in nm*
q=606*1.6*10^-19; %*total charge, in C*
ints=5; %*grid spacing for source (i.e., charge on sample) in nm*
%s=300; %*sigma for Gaussian of charge distribution, if Gaussian distribution is to be used*
R1=52.5; %*tip radius in nm*
X=[0:int:range]; %*X,Y lateral position of tip wrt origin about which charge distribution is centered.*
Y=0*X;
e0=8.85*10^-12; %*units C^2/Nm^2*
sigma=0.34; %*sigma for Ar in nm, for vdW, see Table 4.1 and equation 4.5*
epsilon=1.67*10^-21; %*epsilon for Ar as for sigma, in J*
% *number density of Si, SiO2 in m-3, see Table 4.1*
nsi=5*10^28;
nsio2=6.81*10^28;
kvdw=10^-36*(4/3)*(pi^2)*epsilon*nsi*nsio2*sigma^3*R1;
A=(kvdw)*sigma^3;
B=(2/15)*(kvdw)*sigma^9; % *dF/dz=A/z^3-B/z^9*
K=0.0068; %*Set-point force gradient, estimated using frequency shift, in N/m.*

%*Below sets up charge distribution*
tots=(2*sr)/ints+1;
x=ones(tots);
source=zeros(tots);
count=0;
ys=[ints:ints:sr];
xs=(sqrt(sr.^2-ys.^2));
for i=1:sr/ints-1
    si=round((tots-(2*xs(i)/ints+1))/2)+1;
    sf=tots-si+1;
    if (abs(si-sf)+1)==tots
        count=count+1;
    end
    source(sr/ints+1-i,si:sf)=x(1,si:sf);
    source(sr/ints+i+1,si:sf)=x(1,si:sf);
end
totc=2*count+1;
si=(tots-totc)/2+1;
sf=tots-si+1;
source(1,si:sf)=x(1,si:sf);
source(2*sr/ints+1,si:sf)=x(1,si:sf);
source(sr/ints+1,:)=x(1,:);

```
[xs,ys]=meshgrid(-sr:ints:sr);
xsh=xs(sr/ints+1:2*sr/ints+1,:);
ysh=ys(sr/ints+1:2*sr/ints+1,:);
qs=source;
```
%qs=exp(-(xs.^2+ys.^2)./(2*s^2)).*source; %*for Gaussian profile–MUST BE COMMENTED OUT IF A GAUSSIAN PROFILE IS NOT DESIRED*
```
N=sum(sum(qs)); %Normalization
qs=q*qs./N;
qsh=qs(sr/ints+1:2*sr/ints+1,:);
```

****

newtjh.m   This function can be run only after prefith has been run. The input requires an initial "guess" or set of height values (dd). A good starting place is the data to be fit, with the appropriate offset added (i.e., the height of the tip above the sample in a charge-free region). The input also requires the number of iterations to be performed (itt). The output is the height (d) of the tip above the sample for the chosen scan, and the error (err). If the error is unacceptable, more iterations are needed. If the calculated scan does not match the scan that is being fitted, the charge distribution in prefith.m must be altered.

****

```
function [d,err]=newtjh(dd,itt)
%dd is a set of initial values (e.g., data to be fit)
%Run this to solve for z using Newton's method
%d is answer, err is error
%Need to run prefith.m first.

for i=1:itt
    [f,df]=ftbjh(dd);
    dd=dd-f./df;
end
[err,junk]=ftbjh(dd);
d=dd;
```

****

Other functions called by newtjh.m: ftbjh.m Note: lines that are too long have been split across several lines.

****

```
function [ftot,dftot]=ftbjh(z)
%This function calculates the force gradient and the derivative of the force gradient,
to be used in Newton's method
global int range X Y xs xsh ysh ys R1 sr qs qsh ints A B K s
tots=(2*sr/ints)+1;
f=0*z;
df=0*z;
for l=1:range/int+1


%find the image charge values and location
    [xt,yt,zt,qt,dqtdz,dztdz,dxtdz,dytdz,d2qtdz2,d2ztdz2,d2xtdz2,d2ytdz2]
        =imqjf(z(l),X(l),Y(l),xsh,ysh,R1,qsh);
%first, ii=1 row, where ys=yt=0
    ii=1;
    for jj=1:tots
        if qt(ii,jj)~=0
[fi,dfi]=tbjf(xs,ys,xt(ii,jj),yt(ii,jj),zt(ii,jj),qs,qt(ii,jj),dqtdz(ii,jj),dztdz(ii,jj),
        dxtdz(ii,jj),dytdz(ii,jj),d2qtdz2(ii,jj),d2ztdz2(ii,jj),d2xtdz2(ii,jj),d2ytdz2(ii,jj));
        f(l)=f(l)+sum(sum(fi));
        df(l)=df(l)+sum(sum(dfi));
        end
    end
%next, rest of rows, which, due to symmetry, need to be multiplied by 2.
    for ii=2:sr/ints+1
        for jj=1:tots
            if qt(ii,jj)~=0
[fi,dfi]=tbjf(xs,ys,xt(ii,jj),yt(ii,jj),zt(ii,jj),qs,qt(ii,jj),dqtdz(ii,jj),dztdz(ii,jj),
        dxtdz(ii,jj),dytdz(ii,jj),d2qtdz2(ii,jj),d2ztdz2(ii,jj),d2xtdz2(ii,jj),d2ytdz2(ii,jj));
                f(l)=f(l)+2*sum(sum(fi));
                df(l)=df(l)+2*sum(sum(dfi));
            end
        end
    end
end
%add van der Waals as well
ftot=-f+A./z.^3-B./z.^9-K;
dftot=-df-3*A./z.^4+9*B./z.^10;
```

****

Functions called by ftbjh.m: imqjf.m   Note: lines that are too long have been split across two lines.

****

function [xt,yt,zt,qt,dqtdz,dztdz,dxtdz,dytdz,d2qtdz2,d2ztdz2,d2xtdz2,d2ytdz2]
  =imqjf(zz,xx,yy,xs,ys,R1,qs)

%Finds location and value of image charges
yw=sqrt((zz+R1).^2+(xx-xs).^2+(yy-ys).^2);
qt=-R1*qs./yw; yp=R1^2./yw; xt=xx-(xx-xs).*(R1./yw).^2;
yt=yy-(yy-ys).*(R1./yw).^2;
zt=zz+R1-(zz+R1).*yp./yw;
dqtdz=R1*qs.*yw.^(-3).*(zz+R1);
dztdz=1-(R1./yw).^2+2*(zz+R1).^2.*yw.^(-4).*R1.^2;
dxtdz=2*((xx-xs)./yw.^4).*R1.^2.*(zz+R1);
dytdz=2*((yy-ys)./yw.^4).*R1.^2.*(zz+R1);
d2qtdz2=R1*qs.*yw.^(-3)-3*R1*qs.*yw.^(-5).*(zz+R1).^2;
d2ztdz2=6*R1.^2.*(zz+R1).*yw.^(-4)-8.*(zz+R1).^3.*R1.^2.*yw.^(-6);
d2xtdz2=2*((xx-xs)./yw.^4).*R1.^2-8*((xx-xs)./yw.^6).*R1.^2.*(zz+R1).^2;
d2ytdz2=2*((yy-ys)./yw.^4).*R1.^2-8*((yy-ys)./yw.^6).*R1.^2.*(zz+R1).^2;

****

Other functions called by ftbjh.m: tbjf.m   Note: lines that are too long have been split across several lines.

****

function [f,df]
=tbjf(xs,ys,xt,yt,zt,qs,qt,dqtdz,dztdz,dxtdz,dytdz,d2qtdz2,d2ztdz2,d2xtdz2,d2ytdz2)
%The actual equation
%Calculates the force gradient and the derivative of the force gradient between one charge and one image charge
global e0
kq=10^27/(4*pi*e0);
%factor 10^27 allows distances in nm but gives dF/dz in N/m
D=zt.^2+(xs-xt).^2+(ys-yt).^2;
dDdz=-2*((-zt).*dztdz+(xs-xt).*dxtdz+(ys-yt).*dytdz);
f=kq*
  qs.*(dqtdz.*(-zt).*D.^(-1.5)-qt.*dztdz.*D.^(-1.5)-1.5*qt.*(-zt).*D.^(-2.5).*dDdz);
d2Ddz2=-2*((-zt).*d2ztdz2+(xs-xt).*d2xtdz2+(ys-yt).*d2ytdz2)
  +2*(dztdz.^2+dytdz.^2+dxtdz.^2);
df=kq*qs.*(d2qtdz2.*(-zt).*D.^(-1.5)-2.*dqtdz.*D.^(-1.5).*dztdz
  -3*dqtdz.*(-zt).*D.^(-2.5).*dDdz-qt.*D.^(-1.5).*d2ztdz2
  +3*qt.*dztdz.*D.^(-2.5).*dDdz
  +(15/4)*qt.*(-zt).*D.^(-3.5).*dDdz.^2-1.5.*qt.*(-zt).*D.^(-2.5).*d2Ddz2);

A.2   Tapping mode

A.2.1   Programs for force lookup table

This section contains Matlab files for running the tapping mode model. This subsection contains the files necessary for calculating the force lookup tables used in the model: calc_lookup_s provides the table for contact and van der Waals forces and calc_lookup_e for electrostatic forces. At the beginning of these two programs, the user must define several parameters such as tip radius (R1), particle radius (R2) and values for the table limits (dint1, dint2, ds, df, Xs, Xint, Xf). For calc_lookup_s various material parameters for the tip and sample (Es, nu_s, Et, nu_t, W, H) must be defined as well. For calc_lookup_e, the number of points in the charge grid (nph, nth), and the type of charge distribution must be specified. Normally the electrostatic force lookup table is calculated with q=e (unit charge), then multiplied later by the square of the amount of charge needed. Note that these programs have not been tested in all cases, and good practice requires plotting the results after calculation. For calc_lookup_s, the variables fqdot (force table for particle), fplane (force table for plane), zv, dv, zm, dm (vertical dimension in vector and matrix form) and Xv, Xm (lateral dimension in vector and matrix form) are all saved in the file FILENAME. Similarly, for calc_lookup_e, the variables fe (electrostatic force table) and zve, dve, Xv, (vertical and lateral dimensions in vector form) are saved in FILENAME _e.

JKR force

calc_lookup_s.m

****

global fplane fqdot zv Xv

%lookup table parameters
dint1=0.01;% *nm, interval for contact region*

dint2=0.2;% *nm interval for vdW region*
ds=-4;%*max indentation*
df=300;%*max distance from sample*
R1=90;%*tip radius nm*
R2=14.0325;%*radius of particle, nm*
Es=7E10;%*Young's modulus of SiO2 N/m2*
Et=279E9;%*Young's modulus of Cr N/m2*
nu_s=0.17;% *Poisson's ratio of SiO2*
nu_t=0.21;% *Poisson's ratio of Cr*
W=0.756;%*Work of adhesion, Cr/SiO2 N/m*
H=1.8E-18;%*Hamaker constant Cr/Si02*
Xs=0;
Xint=100/64;%*nm (length of scan in nm)/(number of pixels)*
Xf=100;% *length of scan in nm*

%calculate lookup table
[fplane,fqdot,zm,zv,Xm,Xv,dm,dv]
        =force_s(dint1,dint2,ds,df,Xs,Xint,Xf,R1,R2,Es,Et,nu_s,nu_t,W,H);
save FILENAME fqdot fplane zv dv Xv Xm dm zm

        ****

Functions called by calc_lookup_s.m: force_s.m   Note: lines that are too long have been split across two lines.

        ****

function [fplane,fqdot,zm,zv,Xm,Xv,dm,dv]
        =force_s(dint1,dint2,ds,df,Xs,Xint,Xf,R1,R2,Es,Et,nu_s,nu_t,W,H)
%*This function calculates the force lookup tables for the contact (JKR) and van der Waals forces of a particle of radius R2 and tip of radius R1.*
    %*R1,R2,ds,df,dint1,dint2,dd0,Xs,Xint,Xf dc in nm*
    %*f's in nN, H in J, Es,Et in N/m2*

    %*find which values of r (tip-particle spacing) need JKR, which vdW*
R=R1*R2/(R1+R2);
[fcs,dcs]=finddc(dint1,R,Es,Et,nu_s,nu_t,W);
    %*find which values of d (tip-plane spacing) need JKR, which vdW*
[fc,dc]=finddc(dint1,R1,Es,Et,nu_s,nu_t,W);
    %*find dd0s, dd0, so that JKR and vdW have same value at contact*
[dd0s,rdd0]=find_dd0s(H,R1,R2,dcs,fcs);
dd0=find_dd0_approx(H,R1,dc,fc);
    %*find JKR for plane*
dpjkr=[ds:dint1:dc];
fpjkr=lookupjkr(dpjkr,R1,Es,Et,nu_s,nu_t,W,H);

```
%find vdW for plane
dpvdw1=[dc+dint1:dint1:dc+3*dint2];
dpvdw2=[dc+4*dint2:dint2:df];
dpvdw=[dpvdw1 dpvdw2];
fpvdw=fvdw(dpvdw,R1,dd0,H);
fplane=[fpjkr fpvdw];
d=[dpjkr dpvdw];
dv=d;
zv=dv+R1;

X=[Xs:Xint:Xf];
Xv=X;
[Xm,dm]=meshgrid(Xv,dv);
zm=dm+R1;
%find values for tip-particle
r=sqrt((dm+R1-R2).^2+Xm.^2)-R1-R2;
%find which part of matrix needs vdw, which jkr, which both (mix)
[rjkr,Xjkr,djkr,rmix,Xmix,dmix,rvdw,Xvdw,dvdw]=sortit(r,Xm,dm,dcs);
%Next calculate f
ff=[];
if any(rjkr)
   ffjkr=lookupjkr(rjkr,R,Es,Et,nu_s,nu_t,W,H);
   ffjkr=take_zcomp(djkr,rjkr,R1,R2,ffjkr);
   ff=[ff; ffjkr];
end
if any(rmix)
   ffmix=domix(rmix,dcs,R1,R2,Es,Et,nu_s,nu_t,W,H,dd0s);
   ffmix=take_zcomp(dmix,rmix,R1,R2,ffmix);
   ff=[ff; ffmix];
end
if any(rvdw)
   ffvdw=fvdwqdot(rvdw,R1,R2,H,dd0s);
   ffvdw=take_zcomp(dvdw,rvdw,R1,R2,ffvdw);
   ff=[ff; ffvdw];
end
fqdot=ff;
```

****

Functions called by force_s.m: finddc.m   Note: lines that are too long have been split across two lines.

****

```
function [fcs,dcs]=finddc(dint1,R,Es,Et,nu_s,nu_t,W)
```

%Finds the force and distance at which contact occurs between tip and particle.

```
%These numbers may have to be changed
dss=0;
dff=0.5;

d=[dss:dint1:dff];
l=length(d);
dneg=-d;
ftemp=fjkr_s(dneg,R,Es,Et,nu_s,nu_t,W);
i=1;
while (i<=l)&((imag(ftemp{i}(1))==0)|(imag(ftemp{i}(2))==0)
  |(imag(ftemp{i}(3))==0)|(imag(ftemp{i}(4))==0))
    i=i+1;
end
if i==1
    'error--change range! make dss smaller'
else
    if i==(l+1)
        'error! make dff larger'
        return
    else
        dcs=d(i-1);
        ft=[];
        for j=1:4
            if imag(ftemp{i-1}(j))==0
                ft=[ft ftemp{i-1}(j)];
            end
            fcs=min(ft);
        end
    end
end
```

     ****

Functions called by finddc.m: fjkr_s.m

     ****

```
function f=fjkr_s(d,R,Es,Et,nu_s,nu_t,W)
```

%Calculates JKR contact force
%Note: d>0 means in contact for these eq'ns, i.e., d in argument list is -(real dimension)

```
%From N.A. Burnham et al. Nanotechnology 8 p. 67 1997
%d,R in nm, answer in nN
%Es,Et in N/m2
%W in J/m2

Ey=((1-nu_s^2)/Es+(1-nu_t^2)/Et)^(-1);
Ktt=(4/3)*Ey;
dbar=1E-6*d.*(pi^2*W^2*R/Ktt^2)^(-1/3);
c4=9/4;
c3=0;
c2=-(9/2).*dbar;
c1=-6;
c0=(9/4).*dbar.^2;
[endi,endj]=size(d);
for i=1:endi
    for j=1:endj
        abar{i,j}=roots([c4 c3 c2(i,j) c1 c0(i,j)]);
    end
end
for i=1:endi
    for j=1:endj
        fbar{i,j}=abar{i,j}.^3-abar{i,j}.*sqrt(6*abar{i,j});
        f{i,j}=fbar{i,j}*pi.*W.*R;
    end
end
```

****

Functions called by force_s.m: find_dd0s.m Note: lines that are too long have been split across two lines.

****

```
function [dd0s,rdd0]=find_dd0s(H,R1,R2,dc,fc)
```

%Gives smudge value to match boundary conditions going from JKR to vdW force regions for tip-particle
  %NOTE: might have wrong root! Check by looking at rdd0!
  %fc in nm, H in J, R1,R2,dc,dd0s in nm

```
C1=-1E18*(H/6)*64*R1^3*R2^3;
C2=R1+R2;
C3=2*R1;
C4=2*R2;
C5=2*(R1+R2);
```

```
p8=1;
p7=2*C5+2*C4+2*C3;
p6=C3^2+C4^2+C5^2+4*(C3*C4+C3*C5+C4*C5);
p4=(C4*C5)^2+(C3*C5)^2+(C4*C3)^2
    +4*(C3*C4*C5^2+C3*C4^2*C5+C3^2*C4*C5);
p5=2*(C4*C5^2+C5*C4^2+C3*C5^2+C3*C4^2+C5*C3^2+C4*C3^2
    +4*C3*C4*C5);
p3=2*(C3*C4^2*C5^2+C3^2*C4*C5^2+C3^2*C4^2*C5);
p2=(C3*C4*C5)^2;
p1=-C1/fc;
p0=-C1*C2/fc;
p=[p8 p7 p6 p5 p4 p3 p2 p1 p0];
rr=roots(p);
rdd0=rr;
if imag(rr(8))==0
  if rr(8)>=0
    dd0s=rr(8)-dc;
  else
    'wrong root!'
  end
else
  'hmm...wrong root'
end
```

****

Functions called by force_s.m: find_dd0_approx.m

****

```
function y=find_dd0_approx(H,R1,dc,fc)
```

%Finds smudge factor to match JKR and vdW forces at contact (tip-plane)
```
cc=1E18*H/(24*R1);
xc=cc/fc-(cc/fc)*sqrt(1-fc/cc);
```
%choose the negative root to get the answer that makes sense!
```
y=2*R1*xc-dc;
```

****

Functions called by force_s.m: lookupjkr.m

****

```
function ff=lookupjkr(r,R,Es,Et,nu_s,nu_t,W,H)
%Used to produce lookup table for JKR force
d=-r;
ftemp=fjkr_s(d,R,Es,Et,nu_s,nu_t,W);
ff=branch_s(ftemp,-d);
```

        ****

Functions called by lookupjkr.m: branch_s.m

        ****

```
function fb=branch_s(ftemp,r)
%Selects the correct branch of the calculated JKR force
%NOTE: range must include zero or won't work
%r is real dimension
past=-0.02;
[endi,endj]=size(ftemp);
for i=1:endi
    for j=1:endj
        if r(i,j)<past
            if imag(ftemp{i,j}(1))==0
                fb(i,j)=ftemp{i,j}(1);
            else
                if imag(ftemp{i,j}(3))==0
                    fb(i,j)=ftemp{i,j}(3);
                end
            end
        else
            ft=[];
            if imag(ftemp{i,j}(1))==0
                ft=[ft ftemp{i,j}(1)];
            end
            if imag(ftemp{i,j}(2))==0
                ft=[ft ftemp{i,j}(2)];
            end
            if imag(ftemp{i,j}(3))==0
                ft=[ft ftemp{i,j}(3)];
            end
            if imag(ftemp{i,j}(4))==0
                ft=[ft ftemp{i,j}(4)];
            end
            if isempty(ft)
                ftemp{i,j}(1)%Dump information for debugging
                ftemp{i,j}(2)
```

```
                    ftemp{i,j}(3)
                    ftemp{i,j}(4)
                    r(i,j)
                    i
                    j
                    return
                end
            fb(i,j)=min(ft);
        end
    end
end
```

****

Functions called by force_s.m: fvdw.m

****

```
function f=fvdw(d,R1,dd0,H)
%vdW for spherical tip and plane, from Hamaker 1937 paper
%R1 in nm, H in J, f in nN
x=(d+dd0)./(2*R1);
f=1E18*(H/(2*R1))*(1/12)*((2./x)-(1./x.^2)-(2./(x+1))-(1./(x+1).^2));
```

****

Functions called by force_s.m: sortit.m

****

```
function [rjkr,Xjkr,djkr,rmix,Xmix,dmix,rvdw,Xvdw,dvdw]=sortit(r,Xms,dms,dc)
%Takes all the tip-sample distances (r) in the lookup table and sorts the rows according
to whether these values of r require JKR, vdW, or both ("mixed")
    dr=-r;
    drsort=dr>-dc;%i.e., need JKR
    [endi,endj]=size(dr);
    i=1;
    ii=0;
    while i<=endi & sum(drsort(i,:)~=0)
        if sum(drsort(i,:))==endj
            ii=ii+1;
        end
        i=i+1;
    end
    ivdw=i;
    ijkr=ii;
```

```
if ivdw<=endi
    if sum(sum(drsort(ivdw:endi,:)))~=0
        'error! in sortit—vdw'
        return
    end
    rvdw=r(ivdw:endi,:);
    Xvdw=Xms(ivdw:endi,:);
    dvdw=dms(ivdw:endi,:);
else
    'lookout!vdw'
    rvdw=0;
    Xvdw=0;
    dvdw=0;
end
if ijkr~=0
    rjkr=r(1:ijkr,:);
    Xjkr=Xms(1:ijkr,:);
    djkr=dms(1:ijkr,:);
    if sum(sum(drsort(1:ijkr,:)))~=endj*ijkr
        'error in sortit—jkr'
        return
    end
else
    'lookout!jkr'
    rjkr=0;
    Xjkr=0;
    djkr=0;
    drjkr=0;
end
if (ijkr+1)~=ivdw
    rmix=r(ijkr+1:ivdw-1,:);
    Xmix=Xms(ijkr+1:ivdw-1,:);
    dmix=dms(ijkr+1:ivdw-1,:);
else
    'lookout!mix'
    rmix=0;
    Xmix=0;
    dmix=0;
end
```

****

Functions called by force_s.m: take_zcomp.m

```
*******************************************************
```

```
function fz=take_zcomp(d,r,R1,R2,f)
fz=((d+R1-R2)./(r+R1+R2)).*f;
```

```
*******************************************************
```

Functions called by force_s.m: domix.m

```
*******************************************************
```

```
function fmix=domix(rmix,dc,R1,R2,Es,Et,nu_s,nu_t,W,H,dd0s)
%Finds either JKR or vdW force as appropriate for the "mixed" rows
[endi,endj]=size(rmix);
fmix=zeros(size(rmix));
dr=-rmix;
drsort=dr>-dc;
R=R1*R2/(R1+R2);
for i=1:endi
    endjkr=sum(drsort(i,:));
    fmix(i,1:endjkr)=lookupjkr(rmix(i,1:endjkr),R,Es,Et,nu_s,nu_t,W,H);
    fmix(i,endjkr+1:endj)=fvdwqdot(rmix(i,endjkr+1:endj),R1,R2,H,dd0s);
end
```

```
*******************************************************
```

Functions called by force_s.m: fvdwqdot.m   Note: lines that are too long have been split across two lines.

```
*******************************************************
```

```
function f=fvdwqdot(r,R1,R2,H,dd0s)
%Calculates the van der Waals force between tip and particle
%r,R1,R2 in nm, H in J, f in nN
if r<0
    'error vdw!'
end
r=r+dd0s;
f=-1E18*(H/6)*
(64*R1^3*R2^3*(r+R1+R2))./(r.^2.*(r+2*R1).^2.*(r+2*R2).^2.*(r+2*(R1+R2)).^2);
```

```
*******************************************************
```

DMT forces

Files for DMT forces are similar to JKR except for some key differences: finddc does not need to be run since dc=0 and fc=fdmt(0) (i.e., contact occurs at d=0), and the program lookupjkr should be replaced by fdmt (see below) in calc_lookup_s.

****

fdmt.m

****

```
function f=fdmt(z,R,Es,Et,nu_s,nu_t,W)
%Calculates DMT contact force
z=-z;
Ey=((1-nu_s^2)/Es+(1-nu_t^2)/Et).^(-1);
a=sqrt(R.*z);
f=1E-9*4.*Ey.*a.^3./(3*R)-2*pi*W*R;%in nN
```

Electrostatic force

calc_lookup_e.m

****

```
global fe zve Xve
%lookup table parameters
qq=1;
nth=15;
nph=15;
dint=1;
ds=1;%max indentation
df=300;%max distance from sample i.e., from plane (not particle)
R1=50;%tip radius nm
R2=14.0325;%radius of particle, nm
Xs=0;
Xint=1.5625;%(lateral scan dimension in nm)/(number of pixels)
Xf=100;%nm, lateral dimension
dve=[ds:dint:df];
ld=length(dve);
zve=dve+R1;
Xv=[Xs:Xint:Xf];
```

```
lx=length(Xv);
[Xm,dm]=meshgrid(Xv,dve);
r=sqrt((dm+R1-R2).^2+Xm.^2)-R1-R2;
phys=r>0; %calculate lookup table
e0=8.85*10^-12;%units C^2/Nm^2
kq=(1.6E-19)^2*(10^27)/(4*pi*e0);
ptcharge=0;%1 for point charge on top of particle, 2 for point charge in center, 3 for a
uniform whole shell charge, anything else, for a uniform half shell charge distribution
[xs,ys,zsr,qs]=chargedist(qq,R2,nth,nph,ptcharge);
[toti,totj]=size(qs);
zs=zsr+R2;
fe=zeros(ld,lx);
for i=1:ld
    for j=1:lx
        if phys(i,j)==1 %i.e., if a physical situation
            fe(i,j)=eforce_m_sym(Xv(j),zve(i),R1,xs,ys,zs,qs,toti,kq);
        else
            fe(i,j)=0;
        end
    end
end
save FILENAME_e fe zve dve Xv
```

```
        *********************************************************
```

Functions called by calc_lookup_e: chargedist.m

```
        *********************************************************
```

```
function [xs,ys,zs,qs]=chargedist(qq,R2,nth,nph,ptcharge)
%Sets up charge distribution
intth=pi/nth;
intph=pi/nph;
if ptcharge==1
    qs=qq;
    xs=0;
    ys=0;
    zs=R2;
elseif ptcharge==2
    qs=qq;
    xs=0;
    ys=0;
    zs=0;
elseif ptcharge==3
    th=[0:intth:pi];
```

```
    ph=[0:intph:2*pi];
    [thm,phm]=meshgrid(th,ph);
    xs=R2.*sin(thm).*cos(phm);
    ys=R2.*sin(thm).*sin(phm);
    zs=R2.*cos(thm);
    qs=ones(size(zs));
    N=sum(sum(qs)); %Normalization
    qs=qq*qs./N;
else
    th=[0:intth:pi/2];
    ph=[0:intph:2*pi];
    [thm,phm]=meshgrid(th,ph);
    xs=R2.*sin(thm).*cos(phm);
    ys=R2.*sin(thm).*sin(phm);
    zs=R2.*cos(thm);
    qs=ones(size(zs));
    N=sum(sum(qs)); %Normalization
  qs=qq*qs./N;
end
```

****

Functions called by calc_lookup_e: eforce_m_sym.m

****

```
function fe=eforce_m_sym(xx,zz,R1,xs,ys,zs,qs,toti,kq);
%Calculates electrostatic force
%Set up for a symmetric charge distribution and tip
[xt,yt,zt,qt]=imq_s(zz,xx,xs,ys,zs,R1,qs);
qt0=qt((toti-1)/2+1,:);
qt=qt(1:(toti-1)/2,:);
xt0=xt((toti-1)/2+1,:);
xt=xt(1:(toti-1)/2,:);
yt0=yt((toti-1)/2+1,:);
yt=yt(1:(toti-1)/2,:);
zt0=zt((toti-1)/2+1,:);
zt=zt(1:(toti-1)/2,:);
[QS,QT]=meshgrid(qs,qt);
[XS,XT]=meshgrid(xs,xt);
[YS,YT]=meshgrid(ys,yt);
[ZS,ZT]=meshgrid(zs,zt);
fi=tbqd_s(XS,YS,ZS,XT,YT,ZT,QS,QT,kq);
[QS,QT]=meshgrid(qs,qt0);
[XS,XT]=meshgrid(xs,xt0);
```

[YS,YT]=meshgrid(ys,yt0);
[ZS,ZT]=meshgrid(zs,zt0);
fi0=tbqd_s(XS,YS,ZS,XT,YT,ZT,QS,QT,kq);
fe=2*sum(sum(fi))+sum(sum(fi0));

****

Functions called by eforce_m_sym.m: imq_s.m   Note: essentially the same as program imqjf.m (non-contact) but without all the derivatives.

****

function [xt,yt,zt,qt]=imq_s(z,xx,xs,ys,zs,R1,qs)
%Finds location and value of image charges
yy=0;
yw=sqrt((z-zs).^2+(xx-xs).^2+(yy-ys).^2);
qt=-R1*qs./yw; xt=xx-(xx-xs).*(R1./yw).^2; yt=yy-(yy-ys).*(R1./yw).^2;
zt=z-(z-zs).*(R1./yw).^2;

****

Functions called by eforce_m_sym.m: tbqd_s.m

****

function f=tbqd_s(xs,ys,zs,xt,yt,zt,qs,qt,kq)
%Calculates electrostatic interaction between image charge and real charge
f=kq*qs.*qt.*(zt-zs).*((zs-zt).^2+(xs-xt).^2+(ys-yt).^2).^(-3/2);

A.2.2   Simulink program

The Matlab toolbox Simulink was used to solve the tapping mode equation (equation 4.6). This subsection contains the Simulink program and the Matlab programs that run with it. Note that the two lines at the beginning of many programs start with the word "global." These two lines must be one line in the Matlab program to run correctly.

****

partheight_le.m

****

%In this program, a scan is calculated. At each lateral position Xv(i), the tip is lowered in lint increments, spending rs time at each height. The subprogram fitline.m determines the height (dsp) at the set-point amplitude (aasp). The amplitude-distance curves generated at each point are saved (al,dl in ALDL) as well as the resulting scan and the linear fits to the amplitude-distance curves (dsp, mm, bb in SCAN)

    clear fplane fqdot fplanem fqdotm fe fem al dl dsp zdist

    set_par_exp *%run to define global variables*

    rl=1200E-5;*%runtime in s, first and last runs*

    rs=240E-5;*%runtime in s, other runs*

    off=1500;*%number of points to include for calculating amplitude*

    load FILENAME *%i.e., JKR/vdW force table*

    load FILENAME_e *%i.e., electrostatic force table*

    qqq=37; *%total charge (in e)*

    fe=fe.*qqq^2;*%electrostatic force lookup table*

    set_par_exp *%run to divide forces by m*

    open zelect2.mdl*%opens Simulink*

    aasp=10.3;*%set-point amplitude*

    xx=Xv;*%lateral dimension scan values from scan to be fit*

    load exp_scan;*%scan to be fit*

zii=exp_scan+110;*%choose initial values to be experimental scan that is been fitted plus some offset*

    vii=0;*% initial velocity*

    lint=0.1;*% Δd in the Section 4.8. Increment by which tip is lowered.*

    R1=50; *%tip radius*

    zL0i=zii-30;*%initial mean position of tip*

    dfinal=max(zL0i-118,1);*%final position of tip*

    for i=1:length(xx)

        [aal,ddl]=lowit_e(xx(i),zii(i),vii,zL0i(i),dfinal(i),lint,R1,rl,rs);

        al{i}=aal;

        dl{i}=ddl;

        save ALDL al dl

        [mm(i),bb(i),dsp(i)]=fitline(al{i},dl{i},aasp,lint);

    end

    save SCAN mm bb dsp

****

Programs called by partheight_le.m: set_par_exp.m

****

%Sets experimental parameters. Correct values must be entered by the user
global zL0 zdist w0 k m Q w a z fplane fqdot fqdotm w02 w02zL0 fplanem b Fm
start_time stop_time zi veli X1 Xv zv ftot ftotm fe fem dve zve runint off

w0=2*pi*73.23*1E3;*%1/s, measured resonance frequency*

k=2.16; *% Calculated spring constant, see Section 4.5.1*

m=k/w0^2;*%mass of cantilever (Section 4.5.1)*

Q=155; *%measured Q value*

w=2*pi*73.13*1E3;*%measured driving frequency*

a=0.2239185;*%estimated drive amplitude, determined so that afree=32nm as measured*

start_time=0;

stop_time=0;

runint=1200E-5; *%in s*

b=w0/Q;*% in 1/s, damping coefficient*

Fm=k*a/m;

w02=w0^2;

w02zL0=w02*zL0;

zdist=zv;

fplanem=fplane./m;

fqdotm=fqdot./m;

fem=fe./m;

****

Programs called by partheight_le.m: zelect2.mdl

****

See Fig. A.1. Note that the Simulation/Parameters/Workspace I/O variables should have Load from workspace Initial state [zi,veli].

****

Programs called by partheight_le.m: lowit_e.m

****

function [al,dl]=lowit_e(xx,zii,vii,zL0i,dfinal,lint,R1,rl,rs)

%Function lowers tip in increments of lint, calculates amplitude at each height
global zL0 zdist w0 k m Q w a z fplane fplanem fqdot fqdotm w02 w02zL0 b Fm
start_time stop_time zi veli X1 Xv zv ftot ftotm fe fem dve zve runint off

X1=xx

zfinal=dfinal+R1;

endlowering=round((zL0i-zfinal)/lint);

runint=rl;

[aa(1),zl,tl,zL0i,zc,tc]=lowit_cont_e(zii+lint,vii,zL0i+lint,lint,R1);
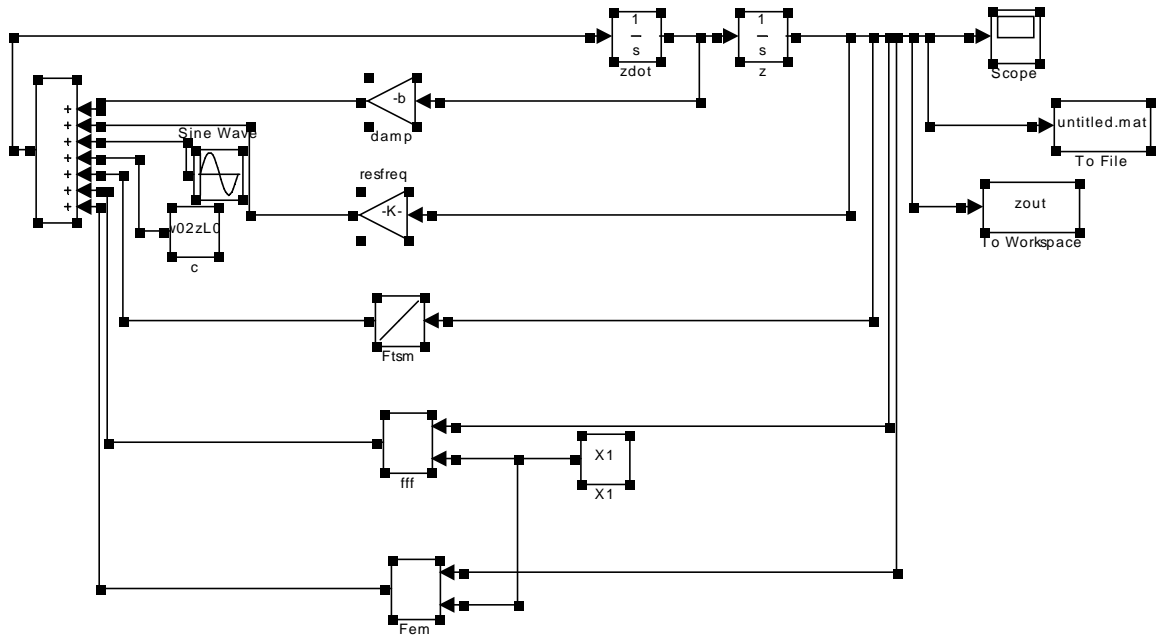
Figure A.1: Simulink model, zelect2.mdl

```
d(1)=zL0i-R1;
runint=rs;
for i=2:endlowering-1
    zii=zc(length(zc),1);
    vi=zc(length(zc),2);
    [aa(i),zl,tl,zL0i,zc,tc]=lowit_cont_e(zii,vi,zL0i,lint,R1);
    d(i)=zL0i-R1;
end
i=endlowering;
runint=rl;
zii=zc(length(zc),1);
vi=zc(length(zc),2);
[aa(i),zl,tl,zL0i,zc,tc]=lowit_cont_e(zii,vi,zL0i,lint,R1);
d(i)=zL0i-R1;
al=aa;
dl=d;
```

****

Programs called by lowit_e.m: lowit_cont_e.m

```
**********************************************************

function [al,zl,tl,zL0i,zout_c,tout_c]=lowit_cont(zii,vi,zL0i,lint,R1)
global zL0 zdist w0 k m Q w a z fplane fplanem fqdot fqdotm w02 w02zL0 b Fm
start_time stop_time zi veli X1 Xv zv ftot ftotm fe fem dve zve runint off
    zi=zii-lint;
    veli=vi;
    zL0=zL0i-lint;
    w02zL0=w02*zL0;
    set_par_sim_e2;
    [tout_c,zout_c]=sim('zelect2');
    [al,zl,tl]=getamp_plus(zout_c,tout_c,off);
    zL0i=zL0;

        **********************************************************
```

Programs called by lowit_cont_e.m: set_par_sim_e2.m
```
        **********************************************************
```

```
%Sets parameters for simulation
global zL0 zdist w0 k m Q w a z fplane fplanem fqdot fqdotm w02 w02zL0 b Fm
start_time stop_time zi veli X1 Xv zv ftot ftotm fe fem dve zve runint off
    start_time=stop_time;
    stop_time=stop_time+runint;
    set_param('zelect2','InitialState','[zi,veli]')
    set_param('zelect2','StartTime','start_time','StopTime','stop_time')
    set_param('zelect2/Sine Wave','frequency','w','amplitude','Fm')
    set_param('zelect2/damp', 'Gain','-b')
    set_param('zelect2/resfreq', 'Gain','-w02')
    set_param('zelect2/c', 'value','w02zL0')
    set_param('zelect2/X1','value','X1')

        **********************************************************
```

Programs called by lowit_cont_e.m: getamp_plus.m
```
        **********************************************************
```

```
function [aa,zz,tt]=getamp_plus(z,t,off)
%Calculates final amplitude
ll=length(t);
while off>ll
    off=off-300;
end
tt=t(ll-off:ll);
zz=z(ll-off:ll,1);
aa=(max(zz)-min(zz))/2;

        **********************************************************
```

Programs called by partheight_le.m: fitline.m

****

```
function [mm,bb,dsp]=fitline(aa,d,aasp,lint)
%Fits a line to the amplitude-distance curve near the set-point amplitude and finds
tip-sample distance at the set-point amplitude.
    l=length(aa);
    s=1;
    while round(aa(l-s))~=round(aasp)
        s=s+1;
    end
    s2=s+1/lint;
    mm=(aa(l-s2)-aa(l-s))/(d(l-s2)-d(l-s));
    bb=aa(l-s2)-mm*d(l-s2);
    dsp=(aasp-bb)/mm;
```